

MONTE CARLO CALCULATIONS OF PATIENT ORGAN DOSES IN TOSHIBA
COMPUTED TOMOGRAPHY EXAMINATIONS WITH AUTOMATIC TUBE CURRENT
MODULATION: A FEASIBILITY STUDY

By

DANIEL J. LONG

A DISSERTATION PRESENTED TO THE GRADUATE SCHOOL
OF THE UNIVERSITY OF FLORIDA IN PARTIAL FULFILLMENT
OF THE REQUIREMENTS FOR THE DEGREE OF
DOCTOR OF PHILOSOPHY

UNIVERSITY OF FLORIDA

2013

© 2013 Daniel J. Long

To Nelia, the love of my life

ACKNOWLEDGMENTS

I first would like to thank my advisor and committee chair, Dr. Wesley Bolch, for his guidance and support throughout my graduate studies, and for giving me the opportunity to pursue research about which I am passionate. I thank Dr. David Hintenlang and Dr. Manuel Arreola, both for their guidance over the course of my academic studies and their support and input as committee members for the work. I also thank Dr. John Aris for his input and advice as the external member of my committee.

I would like to thank all of my colleagues because of whom this research has been successful. First and foremost, I thank Elliott Stepusin for his impressive work ethic, commitment to this research, and his friendship. Because of his knowledge, input, and support, this project has become something of which I can be proud for the rest of my life. I thank Lindsay Sinclair for her generosity in letting me use the data from her own impressive research to conduct my own. I thank Amy Geyer for her generous phantom help, and Kayla Ficarrota for her help with measurements. I thank Matt Maynard, David Borrego, and Matt Hoerner for their friendship and making my days going into the office memorable ones. I would also like to thank Dr. Ryan Fisher and Dr. Chris Tien for their mentorship and friendship.

I would like to thank my parents for their love and support, and who instilled in me the passion for learning and appreciation of hard work that has led me to where I am today. Finally, I thank my beautiful and loving wife, Nelia. Without her, these past few years would not have been as enjoyable and rewarding as they have turned out to be. She truly is my best friend, and I am thankful every day I get to spend with her.

TABLE OF CONTENTS

	<u>page</u>
ACKNOWLEDGMENTS.....	4
LIST OF TABLES.....	9
LIST OF FIGURES	10
LIST OF ABBREVIATIONS.....	12
ABSTRACT.....	14
CHAPTER	
1 INTRODUCTION.....	16
An Overview of Multi-Detector CT Imaging.....	16
Patient Radiation Dose Concerns in CT Examinations	18
Radiation Dose.....	18
Cancer Risks from CT?.....	18
Need for Patient Organ Dose Tracking.....	20
CT Dose Reduction with Automatic Tube Current Modulation	21
Overview	21
Z-Axis ATCM.....	22
Angular ATCM.....	22
Combined ATCM.....	23
Toshiba SureExposure™ 3D.....	23
Overview of Current CT Organ Dosimetry Methods.....	24
Experimental Measurement Dosimetry.....	24
Physical anthropomorphic phantom measurements.....	24
Cadaver measurements.....	26
Advantages and disadvantages	26
Monte Carlo Dosimetry.....	27
Custom Monte Carlo CT sources.....	27
Software programs based on precalculated organ dose databases	28
Advantages and disadvantages	29
Accounting for ATCM in Current CT Organ Dosimetry.....	31
Experimental Measurement Dosimetry.....	31
Monte Carlo Dosimetry.....	32
Objectives of This Research Work.....	33
2 DEVELOPMENT AND VALIDATION OF A MONTE CARLO SOURCE SUBROUTINE OF THE TOSHIBA AQUILION ONE CT SCANNER	38
CT Scan Parameters Affecting Patient Organ Dose	38
Beam Geometry Factors	38

	Source-to-isocenter distance	38
	Scan length.....	38
	Acquisition mode and pitch	39
	Beam Energy	40
	Beam-Shaping Filtration.....	41
	Beam Collimation	41
	Tube-Current Time Product.....	42
	Modeling a Toshiba Aquilion ONE CT Scanner through Experimental Measurements	43
	Description of the Toshiba Aquilion ONE	44
	Custom Source Subroutines in MCNPX	44
	Modeling Geometric Factors	45
	Generating Equivalent CT X-ray Energy Spectra	46
	Accounting for Beam-Shaping Filtration	47
	Beam Collimation and Overbeaming Determination	48
	Beam Output Normalization Factors.....	50
	Validating the Monte Carlo Model with CTDI Phantom Measurements.....	51
	CTDI Phantom Measurements and Simulations	51
	Results.....	53
	Discussion and Conclusion	53
3	DEVELOPMENT AND VALIDATION OF A MONTE CARLO ORGAN DOSE CALCULATION METHODOLOGY FOR TOSHIBA CT EXAMS WITH ATCM	65
	Theoretical Basis for a Precalculated ATCM CT Dosimetry Approach	65
	Cadaver CT Organ Dose Measurements Using OSL Dosimeters.....	66
	Creation of Cadaver-Based Computational Voxel Phantoms	68
	Cadaver ATCM CT Dosimetry Methodology	70
	Slice Dosimetry Calculations	70
	Large Cadaver Fixed Tube Current Dosimetry	71
	Attenuation Calculations.....	72
	ATCM CT Dosimetry and Analysis	73
	Image-based ATCM dosimetry	73
	Calculated attenuation ATCM dosimetry	74
	Results and Discussion	75
	Fixed Tube Current CAP Exam	75
	Determination of the Best Attenuation Weighting Factor Calculation Method ..	76
	Comparison of Tube Current Maps	77
	CT Exams with ATCM.....	78
	Scanner Console Versus Image-Derived Average Effective mAs Values	80
	Conclusion.....	81
4	IMPACTS OF ANTHROPOMORPHIC PATIENT-PHANTOM MATCHING ON ORGAN DOSE IN CT EXAMS WITH AND WITHOUT ATCM.....	97
	Using Computational Phantoms for Patient CT Dosimetry.....	97
	Classifications of Computational Phantoms.....	97

UF/NCI Family of Hybrid Computational Phantoms	99
Determining Patient-Phantom Matching Dose Uncertainties	101
Phantom CT Dosimetry Comparison Study Methodology	102
Patient-Specific Phantom Creation	102
Patient-Dependent Phantom Matching	102
CT Exam Dosimetry	103
Results and Discussion	104
Fixed Tube Current Exams	105
ATCM Exams	107
Conclusion.....	108
5 FINAL CONCLUSIONS AND FUTURE WORK	116
Results and Conclusions of This Work	116
Proposed Future Work	117
MCNPX Source Subroutine	117
ATCM Dosimetry Algorithm	117
Patient-Phantom Matching	118
Final Thoughts.....	118
 APPENDIX	
A CADAVER ATCM DOSE STUDY DATA TABLES	120
Large Cadaver Fixed Tube Current CAP Exam Data Tables	120
Point Dose Comparison	120
Point-Dose-Derived Average Organ Dose Comparison	121
Volumetric Average Organ Dose Comparison	121
Small Cadaver ATCM Exam Data Tables	122
Point Dose Comparison	122
Point-Dose-Derived Average Organ Dose Comparison	125
Volumetric Average Organ Dose Comparison	126
Console Average Effective mAs ATCM Exam Data.....	127
Point dose comparison	127
Point-dose-derived average organ dose comparison	130
Volumetric average organ dose comparison	131
Medium Cadaver ATCM Exam Data Tables	133
Point Dose Comparison	133
Point-Dose-Derived Average Organ Dose Comparison	135
Volumetric Average Organ Dose Comparison	136
Large Cadaver ATCM Exam Data Tables.....	138
Point Dose Comparison	138
Point-Dose-Derived Average Organ Dose Comparison	140
Volumetric Average Organ Dose Comparison	141
B PHANTOM COMPARISON STUDY DATA TABLES	143

Fixed Tube Current Patient-Phantom Matching Study	143
Male Percent Difference Average Magnitude Results	143
Female Percent Difference Average Magnitude Results	144
ATCM Patient-Phantom Matching Study	145
Male Percent Difference Average Magnitude Results	145
Female Percent Difference Average Magnitude Results	146
LIST OF REFERENCES	147
BIOGRAPHICAL SKETCH.....	152

LIST OF TABLES

<u>Table</u>	<u>page</u>
2-1 Body CTDI phantom measurement results	60
2-2 Body CTDI phantom simulation results.....	61
2-3 Body CTDI phantom percent difference results	62
2-4 Head CTDI phantom measurement results	63
2-5 Head CTDI phantom simulation results	63
2-6 Head CTDI phantom percent difference results	64
2-7 CTDI percent difference results summary	64
3-1 Chest-abdomen-pelvis exam scan parameters.....	83
3-2 Chest exam scan parameters.....	84
3-3 Abdomen exam scan parameters.....	85
3-4 Pelvis exam scan parameters	86
3-5 Fixed tube current CAP exam percent difference summary for the large cadaver	90
3-6 Small cadaver percent difference summary over all exams	94
3-7 Medium cadaver percent difference summary over all exams	94
3-8 Large cadaver percent difference summary over all exams.....	94
3-9 Small cadaver percent difference summary over all exams for the calculated attenuation method using console average effective mAs	96
4-1 Adult male patient and matched patient-dependent morphometry data	111
4-2 Adult female patient and matched patient-dependent morphometry data	112
4-3 Adult reference phantom morphometry data.....	112
4-4 Overall percent difference average magnitude results for in-field organs for all fixed tube current CT exams	115
4-5 Overall percent difference average magnitude results for in-field organs for CT exams with ATCM	115

LIST OF FIGURES

<u>Figure</u>		<u>page</u>
1-1	Basic operation of a generic CT scanner	35
1-2	Tube current behavior for the three types of ATCM algorithm.	35
1-3	Reference adult male physical anthropomorphic phantom	36
1-4	UF reference adult computational hybrid phantoms	36
1-5	Screenshot of the ImPACT CTDosimetry dose calculator	37
1-6	Scan range selection in the ImPACT CTDosimetry dose calculator.....	37
2-1	Half-value layer measurement equipment setup.....	55
2-2	First HVL-matched candidate photon energy spectra for 120 kVp and medium bowtie filter	56
2-3	Equipment setup for both beam profile and free-in-air measurements.....	56
2-4	Beam profile data for 120 kVp beam energy	57
2-5	Derivation of beam collimation weighting functions.....	58
2-6	Body CTDI phantom center hole measurement setup	59
2-7	Body CTDI 12 o'clock hole position measurement MCNPX simulation geometry	59
3-1	Chest-abdomen-pelvis exam scan range (thoracic inlet to lesser trochanter)	83
3-2	Chest exam scan range (thoracic inlet to top of kidneys).....	84
3-3	Abdomen exam scan range (dome of diaphragm to iliac crest)	85
3-4	Pelvis exam scan range (iliac crest to lesser trochanter)	86
3-5	Segmented image of the medium cadaver in 3D-DOCTOR™	87
3-6	Medium cadaver phantom's outer body contour, placement tubes, and dosimeter locations	88
3-7	MCNPX visualization of the central ray attenuation detectors at all eight beam projection angles for a chest slice of the small cadaver phantom	89

3-8	MCNPX visualization of the eighth circular arc detector for a 6 o'clock beam projection for a chest slice of the small cadaver phantom.....	89
3-9	MCNPX visualization of the quarter circular arc detector for a 6 o'clock beam projection for a chest slice of the small cadaver phantom.....	90
3-10	Small cadaver CAP exam tube current maps comparison	91
3-11	Medium cadaver CAP exam tube current maps comparison	92
3-12	Large cadaver CAP exam tube current maps comparison.....	93
3-13	Small cadaver percent difference summary over all exams	95
3-14	Medium cadaver percent difference summary over all exams	95
3-15	Large cadaver percent difference summary over all exams.....	96
4-1	Adult male phantom grid for the UF/NCI family of computational hybrid phantoms	110
4-2	Adult female phantom grid for the UF/NCI family of computational hybrid phantoms	110
4-3	Frontal view of the four phantoms used for dosimetry for male patient nine	113
4-4	Left lateral view of the four phantoms used for dosimetry for male patient nine	114

LIST OF ABBREVIATIONS

AAPM	The American Association of Physicists in Medicine
ALRADS	Advanced Laboratory for Radiation Dosimetry Studies
AP	Anterior-posterior
ATCM	Automatic tube current modulation
AQ1	Toshiba Aquilion ONE
BEIR	Biological Effects of Ionizing Radiation
BMI	Body mass index
CAP	Chest-abdomen-pelvis
CDC	Centers for Disease Control and Protection
CT	Computed tomography
CTDI	Computed tomography dose index
CTDI _{vol}	Volume weighted computed tomography dose index
CTDI _w	Weighted computed tomography dose index
DLP	Dose length product
FOC	Fiber-optic coupled
GSF	National Research Center for Environment and Health
HVL	Half-value layer
ICRP	International Commission on Radiological Protection
ICRU	International Commission on Radiation Units and Measurements
kVp	Peak kilovoltage
mAs	Tube current-time product
MCNPX	Monte Carlo N-Particle eXtended
MR	Magnetic resonance
NCI	National Cancer Institute

NEJM	New England Journal of Medicine
NHANES	National Health and Nutrition Examination Survey
NIST	National Institute of Standards and Technology
NRPB	National Radiation Protection Board
NURBS	Non-uniform rational B-spline
ORNL	Oak Ridge National Laboratory
OSLD	Optically-stimulated luminescence dosimeter
PMMA	Poly(methyl methacrylate)
PSD	Plastic scintillator dosimeter
PVC	Polyvinyl chloride
SID	Source-to-isocenter distance
TLD	Thermoluminescent dosimeter
UF	University of Florida

Abstract of Dissertation Presented to the Graduate School
of the University of Florida in Partial Fulfillment of the
Requirements for the Degree of Doctor of Philosophy

MONTE CARLO CALCULATIONS OF PATIENT ORGAN DOSES IN TOSHIBA
COMPUTED TOMOGRAPHY EXAMINATIONS WITH AUTOMATIC TUBE CURRENT
MODULATION: A FEASIBILITY STUDY

By

Daniel J. Long

August 2013

Chair: Wesley Bolch
Major: Biomedical Engineering

In an effort to decrease radiation doses patients receive during computed tomography imaging, scanner manufacturers have implemented a system called automatic tube current modulation (ATCM) that varies the x-ray beam output during a CT imaging exam given information on photon attenuation within the patient's anatomy seen at different positions and angles of the x-ray fan beam. This goal of this work was to develop a robust Monte Carlo methodology to prospectively calculate patient organ doses for exams with ATCM for a wide variety of patient body morphometry, and to quantify the accuracy of the approach.

First, a Monte Carlo-based model of the Toshiba Aquilion ONE scanner at Shands Hospital at UF was created from measurement data and successfully validated using CTDI measurements. Next, voxel computational phantoms of three female cadavers used for CT dose measurements at Shands were created using CT image sets of each individual. Using the Monte Carlo model, average attenuation values for each axial slice of anatomy of the cadavers were calculated in order to approximate the influence of ATCM in tissue energy deposition. Axial-acquisition dosimetry simulations

were first run for four exam protocols on each cadaver. The resulting doses for each axial slice were then modulated by the attenuation values of the slice normalized by the average attenuation in the exam scan ranges and the average effective tube current-time product delivered over each exam. The results indicated that the dose methodology of choice had average percent differences from the measured cadaver doses of less than 13%.

Finally, a study was performed to quantify the effects of matching a patient by height, weight, and body mass index (BMI) to a patient-dependent phantom for four exam protocols with and without ATCM. The study involved 27 adult patients, whose simulated organ doses were compared with those of the patient-dependent phantoms. The results showed that on average for exams without ATCM, there was a 16% average percent difference between the organ dosimetry of the matched phantoms and those of the patients; and with ATCM, this average percent difference was reduced to 11%.

CHAPTER 1 INTRODUCTION

An Overview of Multi-Detector CT Imaging

The first computed tomography (CT) scanner was built by Godfrey Hounsfield in 1971, and since that time, the technology has advanced to exponentially-higher levels of diagnostic imaging capability. The history of this technological progression has been well documented,¹ and is beyond of the scope of this paper. Nevertheless, a grasp of the basic operation of current multi-detector CT scanners is required for better understanding of the work presented in this study, and will therefore be presented here.

Like most external x-ray beam diagnostic imaging modalities, CT imaging utilizes externally incident x-rays to form patient images. These photons are produced in an x-ray tube in which electrons are freed by running a current through a tungsten filament and then accelerated by a potential across the tube called the peak kilovoltage (kVp), a parameter selected by the operator from preset values. The current of the electron beam across this potential is called the tube current and is units of mA. The electrons then strike a tungsten target (or anode) in which their incident kinetic energy is lost.. The majority (99%) of electron energy incident on the target is dissipated through ionization and excitation of the target material. The remaining 1% of that kinetic energy is lost through radiation interactions producing bremsstrahlung photons, x-rays that exit the tube across a spectrum of energies, with the maximum energy corresponding to the incident kinetic energy of the electrons striking the target. It should be noted that the number of photons produced increases with both increases in both tube potential and tube current.

This x-ray tube is situated in a large circular gantry opposite a bank of x-ray detectors shaped in an arc with multiple rows of detectors extending along the “z-axis” of the scanner geometry, or what is also known as the axis of rotation. These multiple rows of detectors in this direction are what give “Multi-Detector” CT its name. The plane that contains the detectors and the x-ray tube and is perpendicular to the axis of rotation and is called the x-y plane. The patient lies down on a table that is centered at a point between the x-ray tube and the detectors (known as the isocenter), and is positioned at a starting location corresponding to the anatomical starting point of the exam. The gantry begins to rotate (usually at speeds of 0.5 to 1 rotations per second), the x-ray tube is energized, and the table begins to translate. As the x-rays travel through the patient, they can interact with atoms of the imaged tissues through both scattering and absorption processes, with a given fraction pass through the patient without interaction. The probability of these interactions largely depends on the tissue type (e.g. the photons will be absorbed more readily in denser and higher atomic number bone tissue than in the other soft tissues of the body). Those photons that penetrate the patient's body are then absorbed and counted by the detectors on the opposite side. The photon count data for a given location, or projection, of the x-ray beam is then collected and sorted based on the location of the beam relative to the patient.

After the entire scan length of patient has been irradiated, the projection data are analyzed and converted into images based on two possible image reconstruction algorithms, known as filtered backprojection or iterative reconstruction. These images show cross-sectional anatomy (akin to slices of a loaf of bread) of the patient based on the differences in x-ray attenuation properties of the tissue structures, which allow the

radiologist to identify and diagnose disease, abnormalities, and other conditions with much more precision than with traditional planar x-ray radiography. A simplified diagram of the basic operation of a CT scanner can be seen in Figure 1-1. Please note a more thorough description of each CT beam parameter and its effect on patient dose can be found in Chapter 2.

Patient Radiation Dose Concerns in CT Examinations

Radiation Dose

Radiation absorbed dose in its most basic form is a measurement of the amount of energy imparted by incident radiation to a particular organ or other biological structure divided by the mass of that structure. The most common unit of absorbed dose is the gray (Gy), defined as one joule (J) of energy absorbed per kilogram (kg) of tissue mass. The importance of this metric lies within the fact that in radiation biology studies, the radiation absorbed dose delivered to cells is predictive of the probability for either non-lethal cell changes (e.g., chromosome aberrations) or lethal cell change (e.g., reproductive cell death). On a more macroscopic level, sufficiently high radiation doses can cause deterministic effects (tissue reactions) such as skin burns and Acute Radiation Syndrome. Increasing absorbed dose at all levels can increase one's risk for cancer incidence or mortality, even at doses below thresholds for deterministic effects.²

Cancer Risks from CT?

The growing diagnostic capabilities of CT imaging have led to the annual number of exams performed in the United States to increase from 3.6 million in 1980 to 72 million in 2007.³ This trend has started to alarm some members of the radiation protection community, as the radiation doses delivered to a patient from a CT exam are much larger than those of normal planar radiography or diagnostic fluoroscopy, normally

in the range of 15-25 mGy, and could hypothetically lead to an overall increase in cancer risk in the population.

The first paper to really address this concern was published in the *New England Journal of Medicine (NEJM)* by Brenner *et al.* in 2007.⁴ The article drew national media attention and controversy due to its claim that 1.5% to 2% of all cancers in the United States could be attributed to CT exam exposures. The claims were met with sharp criticism due to the methods of dosimetry and risk estimation, especially the latter.⁵ The authors based their risk estimates on the Biological Effects of Ionizing Radiation Report VII (BEIR VII), a set of cancer incidence and mortality risk models derived mainly from radiation epidemiological studies of the Japanese atomic bomb survivor cohort, who received radiation doses from the nuclear weapons dropped on Hiroshima and Nagasaki in 1946 during World War II.² The survivors of the bombings were exposed to whole-body doses of radiation from combinations photons and neutrons with wide energy ranges, whereas patients undergoing CT exams are exposed to photons in a specific range of diagnostic energies and in specific regions of the body (and thus not delivered across the whole body). Additionally, the minimum radiation doses from which the epidemiologists were able to prove causality of additional cancer incidence and mortality was still well above the doses received in a typical CT examination.⁵ Many felt that this article was damaging in nature, as it relied on questionable assumptions to calculate risks that would potentially alter patients' decisions to undergo potential life-saving imaging procedures due to fear of the extrapolated dangers of CT examinations as spread in the media. Therefore, many argue that the only certain way

to establish the validity of risks from CT exposure was to perform epidemiology studies on populations of patients who have received these imaging procedures themselves.

The first such risk study was published in *The Lancet*, which was the first epidemiological study to find a statistical link, though small, between childhood CT exposures and leukemia and brain cancer incidence based on a retrospective cohort study of children in the UK that had undergone CT exams.⁶ The report, though providing more accurate dosimetry methods and a more applicable cohort from which to draw statistical conclusions than the Brenner *et al.* study, was still met with criticism.⁷ One major concern was the fact that these dose estimates had to be made retrospectively; therefore assumptions had to be made regarding some of the beam parameters of exams which could have caused estimates to differ considerably from the actual doses received by the patients in the cohort. In order to better understand the true links between CT patient dose and cancer risk, more such studies must be undertaken to decrease the statistical certainties of the data.

Need for Patient Organ Dose Tracking

In order to provide the best dosimetry results for such epidemiological studies, patient organ doses for those in a cohort would ideally already have been calculated immediately after their actual exam and would have that data stored in their medical records. This type of organ dose tracking would eliminate the need for the assumption-filled practice of retrospective dosimetry that can affect the validity and results of an epidemiology study. Individual organ doses would need to be calculated due to the fact that CT exams do not result in whole-body irradiation, but rather non-uniform doses are delivered to organs that in or out of the scan range of interest as based on the specific exam protocol. Therefore, appropriate future CT-based risk models would describe the

risks for individual organs rather than simply for cancer incidence or mortality as a whole. The benefits of patient organ dose tracking would extend beyond simply the creation of these risk models, but they would rather allow physicians to be better informed regarding the risks associated with prescribing CT exams to their patients. In addition, some states are now starting to pass legislation requiring the reporting of patient CT doses in medical records (such as Assembly Bill No. 510 in California); consequently, the time to act is now to development accurate methods of patient dosimetry that could be used practically in the clinic.

CT Dose Reduction with Automatic Tube Current Modulation

Overview

In response to increased concern over CT doses (particularly for pediatric patients), scanner manufacturers began implementing dose-reduction techniques in their designs, one of which was automatic tube current modulation (ATCM).⁸ The overall goal of an ATCM algorithm is to provide an acceptable, uniform, and diagnostic-level image quality across an entire exam while maintaining patient dose at a minimum.⁹ While these ATCM algorithms of different scanner manufacturers are proprietary in nature, at their core are techniques based on the fact that for a constant image noise (i.e. a constant number of photons incident on the detectors), less-attenuating sections of the body will require fewer incident photons (and therefore less tube current) than for higher-attenuating sections of patient anatomy.⁹⁻¹² ATCM algorithms can be categorized into three types: z-axis modulation, angular modulation, and combined (z-axis and angular) modulation.⁹⁻¹²

Z-Axis ATCM

In z-axis (or longitudinal) ATCM, a pre-scan radiograph (called a scanogram by Toshiba) is taken of the patient in order for the system to calculate the photon fluence necessary to maintain a user-defined noise level in the reconstructed image along the length of the patient.¹¹ While the tube current remains constant during a single x-ray tube rotation, it varies along the z-axis length of the patient. Lower tube current values are given to rotations surrounding lower-attenuation areas of patient anatomy such as the chest, while higher tube currents are given to rotation surrounding higher-attenuation areas of patient anatomy such as the pelvis. A hypothetical example of the behavior of the tube current under z-axis ATCM can be seen in Figure 1-2A.

Angular ATCM

During angular (or x-y) ATCM, the goal is to equalize the photon fluence to the detectors as the x-ray tube rotates about the patient in the x-y or imaging plane.¹¹ The CT operator chooses an initial value for the tube current-time product, and the current is modulated from the initial value within a gantry rotation.¹¹ For example, in a rotation around the shoulder region, the tube current would be lower during anterior-posterior (AP) projections of the rotation, and would be higher during its lateral projections. The exact modulation of the tube current is usually determined in one of two ways. The first is by taking two initial radiographs (one AP and one lateral) of the patient, and then fitting a sinusoidal pattern to the attenuation information obtained within these two projections. The second is by calculating the modulation “on the fly” or through “online feedback” during an exam (which requires no input from the initial pre-scan radiograph), whereby the current is automatically adjusted based on the attenuation measured from

the previous 180° beam projection data.¹¹ A hypothetical example of the behavior of the tube current under angular ATCM can be seen in Figure 1-2B.

Combined ATCM

In combined (or x-y-z axis) ATCM, the tube current is varied both within one tube rotation and along the length of the patient, essentially combining z-axis and angular ATCM into one algorithm.¹¹ There are two methods of using the combined ATCM approach. The first is by taking a single scout radiograph to determine the z-axis changes of the modulation, and then using online feedback to initiate the x-y modulation of the image acquisition. The second involves taking two scout radiographs (AP and lateral) from which both the z-axis and x-y axis changes to the tube current are determined from the attenuation information gained from these radiographs.¹¹ This combined method results in dose reductions higher than either angular or z-axis ATCM alone,¹³ and is currently the method of choice for all major scanner manufacturers.¹⁴ A hypothetical example of the behavior of the tube current under combined ATCM can be seen in Figure 1-3C.

Toshiba SureExposure™ 3D

Since the focus of this work will be on CT exams with ATCM on a Toshiba scanner, it is appropriate to have an overall understanding for the basic workings of this algorithm. For its current scanners, Toshiba uses a combined ATCM algorithm named SureExposure™ 3D.¹⁴ For this system, two pre-exam “scanograms” are taken of the patient (AP and lateral), from which attenuation information is collected and used to pre-calculate the map of the tube current for the upcoming imaging examination. The actual values of the tube current are determined by a specified target standard deviation image quality metric, which determines the standard deviation of pixel values in the

reconstructed image. The system also allows for the selection of minimum and maximum tube current limits to avoid under and overexposures.

Overview of Current CT Organ Dosimetry Methods

There are a variety of methods currently used to provide patient CT organ dosimetry. These methods generally fall into two categories: doses based on experimental measurements, and doses based on computational Monte Carlo methods.

Experimental Measurement Dosimetry

Physical anthropomorphic phantom measurements

Experimental organ dose measurement in CT is performed using physical anthropomorphic phantoms, which are physical representations of patients. These phantoms allow for direct dose measurement by means of various dosimeter systems embedded within these physical patient replicas. The dosimeters record energy deposition by x-rays while the phantoms are scanned using typical CT protocols. They are subsequently retrieved and analyzed to give point estimates of organ dose.

In order to give meaningful dose results that reflect real human patients, the anthropomorphic phantoms used for these measurements must exhibit properties that allow better correlation to humans. First, the total body size, internal anatomical structure, and organ masses should be close to those seen in actual patients. Because there are wide variations of patient body morphometry as well as organ masses, physical anthropomorphic phantoms are generally modeled such that their body and organ masses match reference 50th percentile values as put forth by the International Commission on Radiological Protection (ICRP) in its Publication 89.^{15,16} Second and arguably the most important requirement is that these phantoms must be made of tissue-equivalent materials. The majority of these phantoms are composed of up of

three types of materials: soft tissue-equivalent, lung tissue-equivalent, and bone tissue-equivalent substitutes.¹⁵ The major goal for creating these materials is to closely match the reference mass densities and x-ray attenuation coefficients for their respective representative body tissues, as laid out by the International Commission on Radiation Units and Measurements (ICRU) in its Report No. 44. For CT dosimetry, these materials must exhibit correct x-ray attenuation for beams in the diagnostic energy range of 80-140 kVp, as this is the energy range where most all CT scanners operate. Examples of these physical phantoms include those made commercially, such as RANDO (The Phantom Laboratory, Salem, NY) or ATOM phantoms (Computerized Imaging Reference Systems, Inc., Norfolk, VA), and those made at academic institutions, such as those of the University of Florida (UF).¹⁵ Figure 1-3 shows the UF reference adult male anthropomorphic phantom.

In order to record organ doses, dosimeters must be able to be placed within the phantoms without introducing air gaps between slices that could alter dose measurements. The dosimeters able to satisfy this requirement are small point dosimeters such as thermoluminescent dosimeters (TLD), optically stimulated luminescence dosimeters (OSLD), and small scintillator detectors such as the fiber-optic coupled (FOC) plastic scintillator dosimeter (PSD) developed at the University of Florida.¹⁷ These dosimeters are placed within pre-cut holes or channels inside each phantom at measurement locations corresponding to different organs. These point dosimeters measure point doses for organ locations in the phantom during CT examinations, which are assumed to reflect average organ doses. Larger organs may

require two or more dose points within the phantom that are then averaged in the reporting of a single mean value of organ dose.

Cadaver measurements

Another novel approach to experimental organ dose measurement was pioneered by Dr. Thomas Griglock at the Shands Hospital at UF.¹⁸ The measurement approach involves the surgical insertion of polyvinyl chloride (PVC) access tubes into cadavers in which OSLDs could be placed. These tubes are inserted by a board-certified radiologist into several internal organs of interest in the cadaver, and the OSLDs are placed into these tubes in such a manner as to achieve a wide area of anatomical coverage while encompassing the variations in dose gradient seen by each organ of interest. Just as with the anthropomorphic phantom measurements, the cadaver is run through a series of CT protocols, and the doses on the OSLDs are measured to determine organ doses.

Advantages and disadvantages

Physical phantom and cadaver measurements offer direct dose measurements of the CT scanner being evaluated, which eliminates the need to make assumptions regarding the beam output, which is very useful when determining the effects of ATCM (discussed in the following section). However, physical measurements are time-intensive, and require new sets of measurements to be performed for each scan type, energy, and any other scan parameter differences. This can amount to hundreds of man-hours if an entire dose database is being generated. Additionally, dose measurements are restricted to the phantoms or cadavers one has available for measurement. Usually, there are only reference adult and pediatric phantoms available, with no ability to change patient body morphometry. Also, these phantoms

can be prohibitively expensive, which hinders the ability to have a complete set of phantoms in one's possession without significant investment. In the case of cadavers, acquisition can be a complicated and expensive process without exact control over what types of cadaver are available in terms of gender, age, or body morphometry. Cadavers of children and adolescents are particularly difficult to acquire for these purposes.

Monte Carlo Dosimetry

Custom Monte Carlo CT sources

Monte Carlo radiation transport codes have been widely accepted as accurate, reliable, and versatile tools for evaluating patient organ dosimetry for CT examinations.¹⁹⁻³⁰ Monte Carlo radiation transport relies on interaction probabilities and physics relationships that govern the track lengths of transported particles between interactions, the types of interactions, particle direction and energy changes after interaction, and the production of additional particles and their energy and direction. For patient CT dosimetry, custom mathematical models of scanners can be created that simulate their photon output (described in detail in Chapter 2). "Virtual exams" can then be run that involved computational phantoms (digital models of patients, covered in detail in Chapter 4) being irradiated by these source models for any number of exam protocols defined by the user, with the calculated doses delivered to their virtual organs. Two examples of computational phantoms, the UF reference adult male and adult female hybrid phantoms, can be seen in Figure 1-4. The computational time for these calculations can range from minutes to hours based on the processing hardware available and the complexity of the irradiation geometry.

Software programs based on precalculated organ dose databases

A second Monte Carlo method for CT dosimetry is the use of graphical user interface-based software programs based on large-scale organ dose databases generated using Monte Carlo simulation. There are two major CT dose databases that are the most widely cited and used for current software-based programs. One database was introduced in 1991 by the National Radiation Protection Board (NRPB) of the United Kingdom, and the other was introduced in 1991 by the National Research Center for Environment and Health (GSF) of Germany.^{31,32} The NRPB database was computed using an adult hermaphrodite mathematical stylized phantom that was an amalgamation of Cristy's 1980-revision stylized adult phantom, Kramer's 1982-revision neck model, and a breast model of 50% fat and 50% water composition.³¹ The database is composed of dose results from 208 5-mm axial beam slices from the head to the thigh of the phantom for 27 scanner models and 23 sets of exposure conditions (i.e. kVp, beam filtration, and source-to-isocenter distance) based upon a 1989 CT survey conducted by the NRPB within the UK. The GSF database was computed using the ADAM and EVA stylized adult phantoms and the BABY and CHILD voxel phantoms.³² The database is composed of dose results from 10-mm axial beam slices from head to thigh for each phantom for non-scanner-specific beam models. In order to make the use of these databases for dosimetric purposes easier, many groups developed graphical user interface-based software that allowed users to easily calculate organ doses for various CT scan protocols. Of these programs, two have become the most commonly used: CTDosimetry (<http://www.impactscan.org/ctdosimetry.htm>) and CT-Expo.³³

The CTDosimetry software package is based on the NRPB database and was created by the ImPACT Group out of London in the United Kingdom. As part of their program, the group organized an updated CT survey in 1997 that collected relevant data for newer model CT scanners in order to keep the dose database up-to-date. The software's graphical user interface (GUI) in Figure 1-5 allows the user to input scanner model and scan acquisition parameters, and in turn the software displays dosimetric data for the scan. Additionally, the software allows the user to visually see the scan length placed over the phantom to ensure correct placement, as seen in Figure 1-6. In order to account for other ages other than adult patients, the code uses scaling factors to approximate pediatric patient doses.

The CT-Expo software package is based on the GSF database and was created at the Hanover Medical School in Germany. Like the CTDosimetry software, CT-Expo was updated to cover newer scanner models based on a 1999 CT Survey conducted in Germany.³³ The GUI for this software mirrors closely that of CTDosimetry in that there is a one-page dose calculation sheet on which users define scan parameters and an additional page showing the scan length placed over the chosen phantom. Unlike CTDosimetry, a user may choose from four total phantoms instead of only one. Available are a stylized adult male or female phantom, a 7-year-old voxel phantom, and a 2-month-old voxel phantom. In order to account for ages other than those of the available phantoms, the software uses the Brenner and Huda algorithms to interpolate between the doses on the available phantoms.³³

Advantages and disadvantages

Software programs based on organ dose databases offer almost instantaneous dose calculations for a variety of scan parameters. Such programs are ideal for

performing large-scale epidemiological studies where there organ doses must be reported for each of perhaps thousands of members of the study cohort. However, these programs are very limited due to the fact that their majority of organ dose databases are computed using stylized phantoms of only a single age and body type. Stylized phantoms tend to be anatomically unrealistic when compared to actual patient anatomy, which can lead to major errors in reported organ doses. Additionally, these already limited doses have to be scaled to approximate doses for subject ages that are different from those used to construct the organ dose library. Single scaling factors introduce even greater error, as there are vast anatomical differences between pediatric and adult patients that cannot be accounted for using single scaling values. Also, these databases do not allow for changing patient morphometry (underweight and overweight patients), and thus additional error would be introduced if one had to assign single doses for all adults undergoing the same procedure. One other limitation is that doses are calculated for different scanner models based on additional scaling factors based upon ratios of weighted computed tomography dose indices ($CTDI_w$ values). This method may not adequately take into account the spectral and beam filtration differences present in different scanners needed for accurate dose estimation.

The creation and use of custom CT scanner sources for Monte Carlo calculations is the most accurate dosimetric method for patient organ dose estimation. If the goal is to determine organ doses delivered by a specific scanner, this method ensures that the source will be as close to what is measured physically. Additionally, the ability to choose more anatomically realistic phantoms for dose calculations will help alleviate the errors present in other organ dose database libraries. Also, if one uses hybrid

phantoms like those from the University of Florida, patient morphometry can be explicitly taken into account.³⁴ While this method will allow for very accurate organ dose measurements for one particular scanner, a new source model must be created for each scanner upon which organ doses need to be measured. This may pose technical problems if the organ doses are being calculated for epidemiological studies. In this case, the source term could still be used, but conversion factors between different scanner models may still need to be used to avoid having to make hundreds of full sets of organ dose databases. That being said, this method can still be applied to create new organ dose databases and CT dosimetry software that use more anatomically realistic phantoms; therefore improving the accuracy of doses reported in current CT dose software packages.

Accounting for ATCM in Current CT Organ Dosimetry

With the advent of ATCM algorithms for CT exams, the task of providing accurate CT patient organ dosimetry became much more complex, especially for computational methods, as the exact algorithms used by the scanner manufacturers are proprietary in nature. Nevertheless, there have been several studies published in the literature that have sought to account for ATCM in patient CT dosimetry.

Experimental Measurement Dosimetry

As mentioned in the previous section, experimental organ dose measurement lends itself well to quantifying changes in organ dosimetry resulting from the application of ATCM, as no changes in the measurement methodology need to be undertaken when measuring organ doses with or without ATCM algorithms in place. There have been several studies published in which experimental measurements were taken for protocols with and without ATCM to quantify levels of organ dose reduction and to try to

determine empirically-derived dose conversion factors to account for ATCM.^{14,35,36} As was stated previously, the major drawback to this approach is the lack of phantoms of different ages, body shapes, and sizes upon which to quantify these dose changes and therefore capture a wider data set covering more of the patient population.

Monte Carlo Dosimetry

Very similar to the experimental measurement studies, the goals of nearly all currently published computational studies that account for ATCM have been directed toward the creation of “dose conversion factors” that seek to relate organ doses calculated to scanner metrics output post-exam from the scanner console such as $CTDI_{vol}$ or DLP. How these ATCM CT doses are calculated vary slightly based on the study.

A large group of studies involved using computational phantoms that were “twins” of either commercial physical phantoms or patients for which image sets were available. These physical counterparts were imaged using the CT scanner of interest with ATCM, and the resulting tube current information was extracted and worked into the Monte Carlo dose simulations using custom source models or commercially available software.^{23,25,26,37-40} The major drawback to these studies was the fact that these conversion factors were all based on a limited subset of phantoms that may not adequately encompass the patient population.

One study of particular interest to this work was that of Schlattl *et al.*⁴¹ Unlike the other studies published to date, their methodology for quantifying tube current modulation was not in the form of extracting the data post-exam from the scanner. Instead, the authors of this study presented the idea of creating an “ideal” general algorithm stemming from the calculated attenuation information of the computational

phantom being used for dosimetry simulations based on previous work by Gies *et al.*⁴² Nevertheless, the paper's goal was still the calculation of dose conversion factors and thus the authors ran into the same drawbacks of other studies. The idea to try a methodology based on calculating attenuation on the phantoms themselves was born from References 41 and 42.

Objectives of This Research Work

In order to provide a practical, clinically-relevant method of modern CT patient dose calculation, the CT dosimetry group within the Advanced Laboratory for Radiation Dosimetry Studies (ALRADS) at the University of Florida (UF) has begun a project to create a CT patient dosimetry software program in the style of the ImPACT CTDosimetry dose calculator or CT-Expo. The proposed software would address some of the shortcomings of these common tools, including a lack of diverse, anatomically-accurate phantoms to match to patients and the ability to automatically account for ATCM within the simulated CT examination. The software would be based on organ dose databases calculated using Monte Carlo models of the four most common 64-slice CT manufacturers: Toshiba, Siemens, GE, and Philips. The final goal for this software would be both clinical implementation for fast, accurate CT dose tracking for a large variety of patient ages and body shapes and sizes, as well as the ability to provide large-scale dosimetry for radiation epidemiology studies.

The overall goal of this work was to investigate the initial feasibility and accuracy of using the methodologies proposed for this software to provide organ dose estimates for patients undergoing exams with ATCM on Toshiba 64-slice scanners. To accomplish this goal, the following specific aims were pursued:

1. To create a measurement-based Monte Carlo source subroutine of the Toshiba Aquilion ONE CT scanner used clinically at Shands Hospital based upon a combination of previously-investigated methodologies, and to subsequently validate its accuracy using CTDI phantom experimental measurements.
2. To develop and validate a computational attenuation-based methodology within the framework of a pre-calculated organ dose database that accounts for the influences of ATCM on patient organ dose for four standardized CT exams on the Toshiba Aquilion ONE. This aim would be accomplished by using experimental measurements performed on three cadavers of varying body sizes. Organ doses computationally calculated with the developed methodology would be compared with those experimentally determined within the cadavers using OSL dosimeters for the purposes of quantifying the accuracy of the proposed methodology.
3. To quantify dose uncertainties introduced by matching patients to computational patient-dependent phantoms and reference phantoms for CT organ dose simulations for four typical CT exam protocols with and without ATCM. Organ doses would be simulated for 27 adult patient-specific computational phantoms and used as benchmark values of actual patient organ dose received for these examinations. Organ doses would be simulated for matched patient-dependent hybrid, reference hybrid, and reference stylized phantoms and compared to the benchmark doses to quantify the accuracy of using body-sized matched phantoms for patient dosimetry in computed tomography.

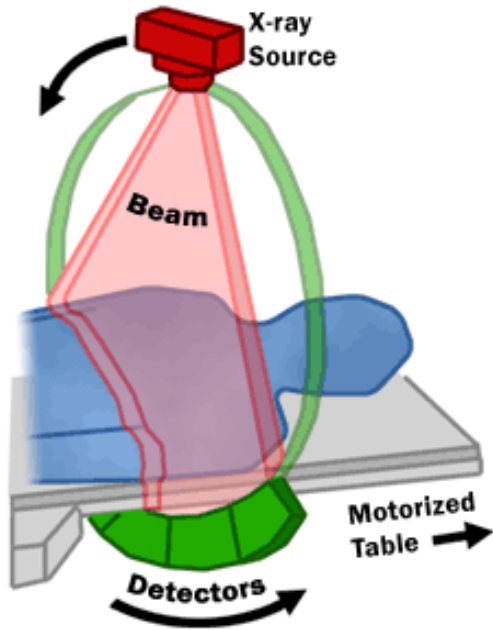


Figure 1-1. Basic operation of a generic CT scanner.

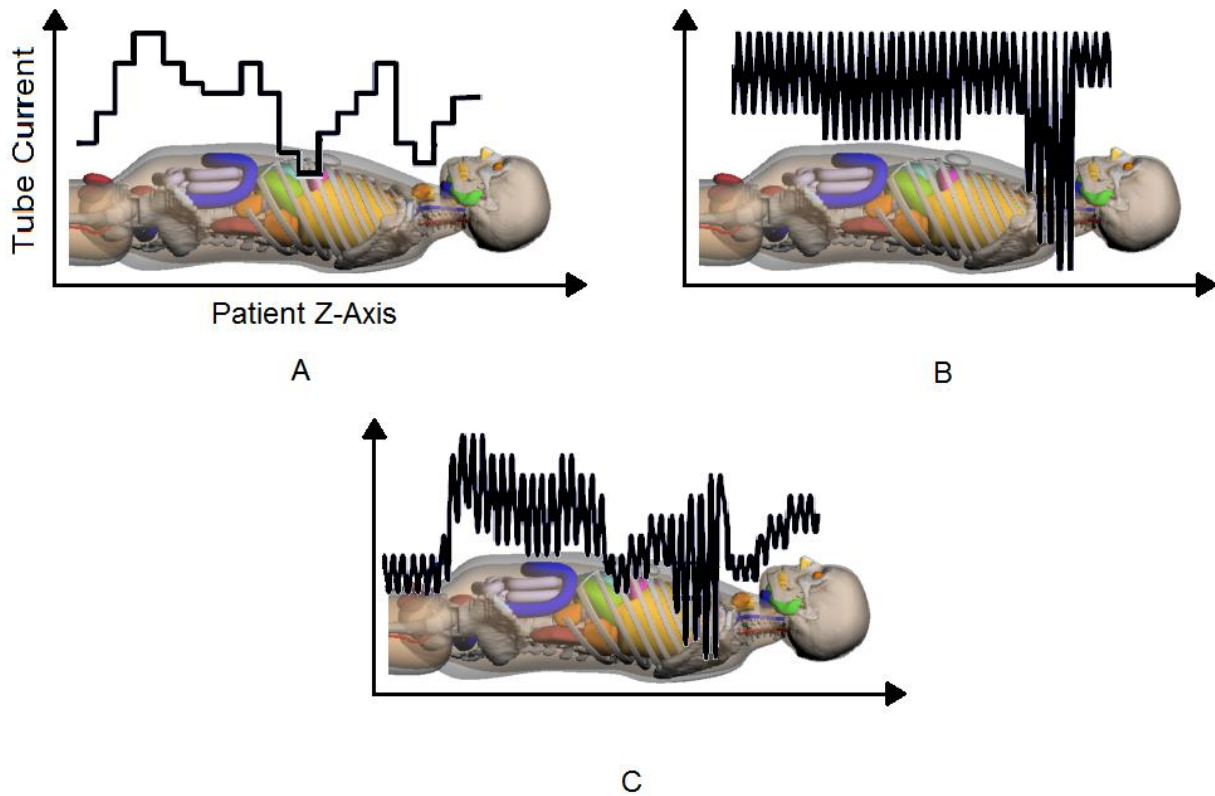


Figure 1-2. Tube current behavior for the three types of ATCM algorithm. A) Z-axis ATCM. B) Angular ATCM. C) Combined ATCM.



Figure 1-3. Reference adult male physical anthropomorphic phantom.

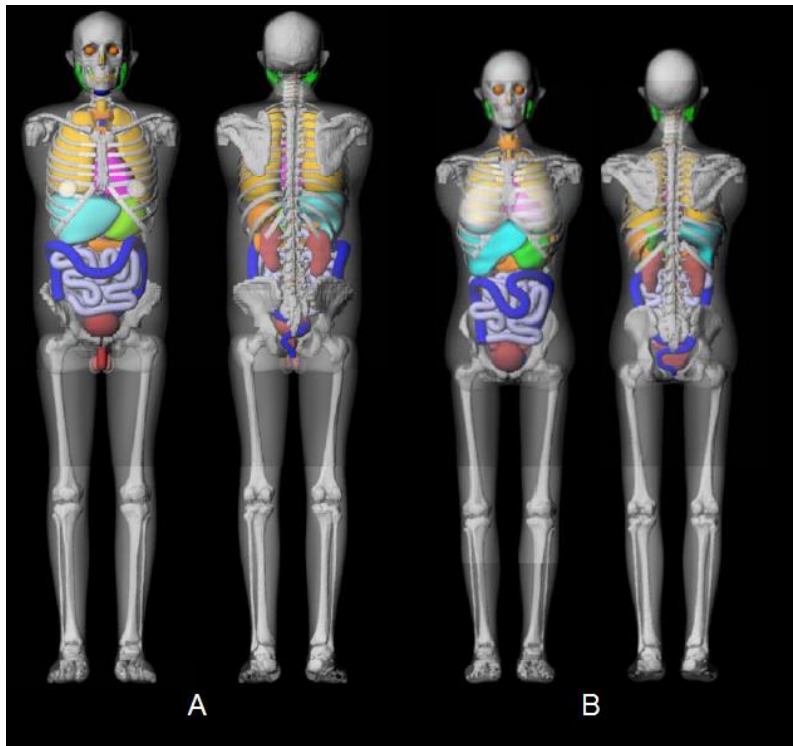


Figure 1-4. UF reference adult computational hybrid phantoms. A) Male phantom. B) Female phantom.

ImPACT CT Patient Dosimetry Calculator

Version 0.99x 20/01/06

Scanner Model:		Acquisition Parameters:	
Manufacturer:	Siemens	Tube current	655 mA
Scanner:	Siemens Sensation 16	Rotation time	0.33 s
kV:	120	mAs / Rotation	216.15 mAs
Scan Region:	Body	Collimation	24 mm
Data Set:	MCSET16	Slice Width	mm
Current Data:	MCSET16	Pitch	1
Scan range:		Rel. CTDI	Look up 0.81 at selected collimation
Start Position:	41.5 cm	CTDI (air)	Look up 12.3 mGy/100mAs
End Position:	73 cm	CTDI (soft tissue)	13.1 mGy/100mAs
Patient Sex:	m	nCTDI _w	Look up 5.5 mGy/100mAs

Organ	w _T	H _T	w _T · H _T
Gonads	0.2	0.014	0.0028
Bone Marrow (red)	0.12	4.9	0.59
Colon	0.12	0.035	0.0042
Lung	0.12	17	2
Stomach	0.12	2.4	0.29
Bladder	0.05	0.0085	0.00042
Breast	0.05	14	0.7
Liver	0.05	3.9	0.2
Oesophagus (Thymus)	0.05	18	0.92
Thyroid	0.05	16	0.81
Skin	0.01	3.7	0.037
Bone Surface	0.01	9.4	0.094
Thymus	0.025	18	0.46
Remainder 2	0.025	3.5	0.088
Total Effective Dose (mSv)			6.2

Remainder Organs	H _T
Adrenals	4.7
Brain	0.28
Upper Large Intestine	0.19
Small Intestine	0.14
Kidney	0.87
Pancreas	3
Spleen	2.7
Thymus	18
Uterus	0.036
Muscle	3.8

CTDI _w (mGy)	11.9
CDTI _{vol} (mGy)	11.9
DLP (mGy.cm)	374

Scan Description / Comments

Figure 1-5. Screenshot of the ImPACT CT Dosimetry dose calculator.

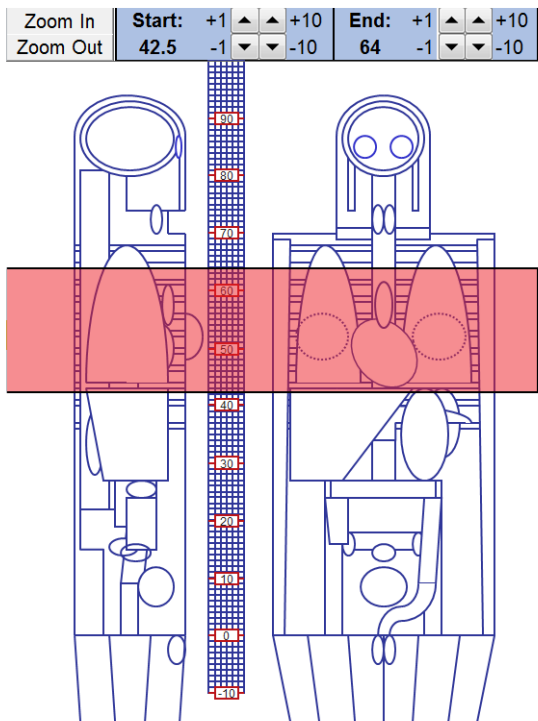


Figure 1-6. Scan range selection in the ImPACT CT Dosimetry dose calculator.

CHAPTER 2 DEVELOPMENT AND VALIDATION OF A MONTE CARLO SOURCE SUBROUTINE OF THE TOSHIBA AQUILION ONE CT SCANNER

CT Scan Parameters Affecting Patient Organ Dose

In order to use Monte Carlo computational techniques to perform patient dosimetry for CT examinations, one must accurately model the output and scan parameters of the CT scanner of interest. Before doing so, however, it is important to identify those parameters and understand their impact on patient organ dose.

Beam Geometry Factors

There are a few geometric factors related to the CT exam that influence patient dose, including source-to-isocenter distance (SID), scan length, and acquisition mode/pitch.

Source-to-isocenter distance

The source-to-isocenter distance is the distance from the x-ray tube anode focal spot to the isocenter of the axis of rotation of the CT gantry. Keeping all other parameters constant, a shorter SID will result in higher doses to the patient, as the photon beam will have geometrically diverged less than at a greater distance.

Scan length

The scan length is the total length the CT exam traverses along the patient. The longer the scan length, the greater the total number of x rays which will impinge upon the patient, thus increasing the whole-body patient dose. However, the more important effect of scan length is determining which organs of the patients are in-field and thus receive direct irradiation from incident x-rays of the primary beam. In-field organs receive much higher doses than those that are out-of-field, which are defined as those outside the body region exposed to the primary beam. These organs will, however,

receive dose from internally scattered x-rays, so it is important to correctly account for their dose contributions when performing organ-level patient dosimetry.

Acquisition mode and pitch

The acquisition mode of a CT exam is either axial or helical. Axial CT exams involve a “step-and-shoot” method whereby the table is moved one nominal beam collimation width for each rotation of the x-ray tube, halted for that rotation, and then moved to the next position, and so on until the full scan length is acquired. In axial mode, there is no overlap of the acquired data for each image slice. In contrast, helical CT exams involve a continuous table motion during tube rotation, thus resulting in much faster exam times than those using axial acquisitions. In fact, the use of axial acquisitions is now limited to very few clinical protocols currently used in modern CT practices (e.g., head scans). The prominent geometric factor in helical exams is the pitch, defined as the ratio of the length of table movement during one x-ray tube rotation and the nominal beam collimation. A pitch of 1.0 would be dosimetrically similar to an axial exam with neither missing nor overlap of irradiated anatomy. In contrast, a pitch of greater than 1.0 would deliver less dose than an axial exam, as it introduces gaps in the acquired data for each image slice and therefore gaps in irradiated patient anatomy. Finally, a pitch of less than 1.0 would deliver greater dose, as it involves overlapping of acquired image data and hence overlapping of the fan beam on regions of patient anatomy. In addition, due to the nature of the image reconstruction algorithms for helical exams, an extra half to whole beam rotation is required on either end of the selected scan range for an exam. This is referred to as “over-ranging” or “helical overscan”, and primarily increases the doses of organs closer to the ends of the scan range. Resultantly, it is important in CT computation simulation to have the ability to

represent the geometry of these scans in order to best represent the acquisition mode of the patient.

Beam Energy

The energy, or quality, of the x-ray spectrum output by the scanner is a parameter that plays a major role in patient dosimetry. In CT scanners, the quality of the x-ray spectrum reaching the patient is determined by the selected kVp (peak kilovoltage), the inherent filtration, and the beam-shaping filtration. The beam energy is selected in units of kVp, which signifies the maximum energy of electrons accelerated in the x-ray tube that in turn denotes the maximum photon energy found in the resulting x-ray spectrum. As the photons generated in the x-ray tube travel out of the scanner, they pass through a layers of materials (including the anode itself), which are collectively called inherent filtration, which removes lower-energy photons in the emerging x-ray spectrum. The resulting spectrum has a higher average energy than what is fundamentally produced in the anode, and is thus more penetrating. Finally, the beam travels through the beam-shaping filter that, while not affecting the energy of the beam as drastically as the inherent filtration, still plays a role in the final quality of the beam before reaching the patient. As the beam quality increases in average energy, the radiation dose delivered to the patient increases when keeping all other parameters constant. This is primarily due to the fact that more energy is available to be imparted by the x rays in each interaction as they travel through the body of the patient. Therefore, it is important to characterize the quality of the beam for every available combination of kVp, inherent filtration, and beam-shaping filtration. In this manner, the correct x-ray beam energy information is available corresponding to the parameters selected for the CT exam of the patient for which dosimetry is being assessed.

Beam-Shaping Filtration

As mentioned in the previous section, the CT x-ray beam travels through a beam-shaping (also called bowtie or compensation) filter after inherent filtration. The purpose of this filter is to ensure that the image detectors receive as close to the same photon energy spectrum as possible for all projections around the patient in the plane perpendicular to the axis of rotation of the scanner (usually referred to as the x-y or imaging plane of the scan geometry). Without this special filter (or with a “flat” filter), the beam is collimated to a fixed angle such that its shape resembles a straight-edged triangle or fan. Since the patient occupies the centerline of the “fan beam”, the photons on the outer edges will often not pass through the patient before hitting the detectors. Thus, they will have a different energy spectrum than those interacting with and exiting the patient. Therefore, the beam-shaping filter is designed such that there is thicker amount of material (often aluminum) on the edges as compared to the center to compensate for the smaller tissue pathlengths of these photons that pass through the more peripheral regions of patient anatomy. The resulting shape resembles the bottom half of a bowtie, so this filter is often referred to as a “bowtie filter”. This filter not only causes a resulting variation in the x ray energy spectrum with regards to position in the fan beam, but also a variation in intensity within the fan beam. These two factors both influence patient dosimetry, and so it is important to understand how each beam-shaping filter setting affects the fan beam in order to account for these effects in Monte Carlo dosimetry calculations.

Beam Collimation

In CT imaging, “beam collimation” most often refers to the width of the x-ray beam along the axis of rotation of the x-ray tube, often referred to as the “z-axis” of the

CT exam. The collimation width settings on a CT scanner are most often in terms of the number of sequential detectors in the z-axis that are active during an exam multiplied by the detector width (e.g., 64 x 0.5 mm would indicate a nominal beam width of 3.2 cm). This nominal beam width is not the true extent of the collimated x-ray beam, however. As with any collimated man-made photon beam, there are curved, less-intense penumbra regions extending past either side of the full-intensity region of the beam profile, that are resultant from the finite size of the anode focal spot. Most CT scanners have two focal spots, one large and one small, with the larger creating a larger penumbra region. The extra size of this region does not drastically increase the dose as compared to the small focal unless the nominal collimation setting is very small, and therefore requiring more x-ray tube rotations to cover a given scan range.⁴³ In addition to this extra penumbra region, the full-intensity region of the beam is actually wider than the nominal beam width setting in an effect known as “overbeaming”. This extra beam width is put into place in order to prevent any active detector element from receiving signal from the penumbra region of the z-axis beam profile, which would result in artificially low signals thereby reducing image quality. The result of these two processes is that the actual z-axis beam width irradiating a patient can be significantly wider than the nominal collimation setting, which would lead to an underestimation of patient dose if not accounted for properly.

Tube-Current Time Product

The tube-current time product, often referred to as the mAs, is a setting that controls the intensity of the photon beam during a CT exam. The parameter is the product of the current of electrons impinging on the anode focal spot of the x-ray tube (in units of milliamperes) and the time (in seconds) of one rotation of the x-ray tube in

the CT gantry. The mAs is approximately linearly proportional to the number of photons emitted into the imaging plane for each x-ray tube rotation for a given beam energy, filter, and collimation combination. Therefore, a higher mAs value will lead to more photons being emitted and therefore greater patient dose. Another widely-used parameter is known as the effective mAs, which is the mAs per rotation divided by the helical pitch of an exam. This value gives an approximate understanding as to the amount of photons emitted over an axial section of patient anatomy. It is often used to approximate helical exam dosimetry by using axial scan dosimetry methods with the effective mAs applied as the mAs value for each slice.

Modeling a Toshiba Aquilion ONE CT Scanner through Experimental Measurements

In order to model a CT scanner for computational patient dosimetry, one must have an understanding of the behavior of CT parameters described earlier in this chapter. These parameters, especially the composition and shape of beam filters, are often proprietary in nature and require a non-disclosure agreement to be signed with a manufacturer before the information is released. Additionally, the information provided is usually factory-tested data and may not accurately describe the exact x-ray output of the particular scanner of interest.⁴³ Therefore, a better alternative is to derive an understanding of the CT parameters through actual physical measurements made on the scanner itself. The methodology described in this section was used to create a Monte Carlo source term model of the Toshiba Aquilion ONE (AQ1) CT scanner (Toshiba America Medical Systems Inc. Tustin, CA). This methodology was based off the dissertation work of Dr. Monica Ghita⁴⁴ and a journal article by Turner *et al.*⁴³

Description of the Toshiba Aquilion ONE

The Toshiba AQ1 is a 320-slice volumetric scanner that has uniform 0.5 mm detector elements. There are four energies (80, 100, 120, and 135 kVp), three beam-shaping bowtie filters (small, medium, and large), two focal spots (small and large), and beam collimations ranging from 1.6 cm (32 x 0.5 mm) to 16 cm (320 x 0.5 mm) available for selection during exams. The scanner can operate in both axial and helical exam acquisition modes, has an SID of 60 cm, and a fan beam angle of 49.2°.

Custom Source Subroutines in MCNPX

Monte Carlo radiation transport codes have been widely accepted as accurate, reliable, and versatile tools for evaluating patient organ dosimetry for CT examinations.¹⁹⁻³⁰ Monte Carlo radiation transport relies on the probabilities and relationships that govern: the track lengths of transported particles between interactions, the types of interactions, the particle direction and energy changes following interaction, and the production of additional particles during interactions and their energy and direction. In these simulations, particles are given initial conditions of location, direction, and energy based on user input and are tracked in a “virtual” manner within a problem geometry also defined by the user. The contributions of each particle to quantities such as absorbed dose and particle fluence to specified structures in that geometry can be tallied as well. If sufficient numbers of particles are transported (usually in the tens to hundreds of millions) for a given problem setup, these quantities can be determined with high statistical confidence.

For this work, a code developed by the Los Alamos National Laboratory, MCNPX (Monte Carlo N-Particle eXtended) Version 2.7,⁴⁵ was used as the code within which a computational model of the AQ1 was created. MCNPX allows the user to create one

custom source subroutine (written in the Fortran 90 coding language) per compiled executable, which requires probabilistic information regarding beam energy, particle starting spatial coordinates, direction vectors from those initial coordinates, and particle weighting and biasing formulas to account for the complex beam shaping characteristics of CT scanners. The Fortran 90 code framework for this subroutine was previously created by Dr. Monica Ghita, and was altered to incorporate the new data derived in this study.⁴⁴

Modeling Geometric Factors

Geometric factors such as scan length, SID, fan beam angle, and acquisition mode/pitch are used to define the starting spatial coordinates of photons to be transported, and are able to be modeled mathematically without the need for input of probabilistic data. The mathematical derivations of these factors are presented in detail in Section 6.4.1 of Dr. Monica Ghita's dissertation.⁴⁴ The subroutine requires user input of the desired scan range starting z-axis coordinate and length, SID, fan beam angle, as well as the desired mode of acquisition. The modes of acquisition include axial, helical (with the ability to input desired pitch and starting angle), and static beam positions (with the ability to select the angle at which the beam is "parked"). Once these inputs are selected, the subroutine creates a geometric trajectory representing the location of the x-ray tube focal spot (where the photons originate and modeled as a point source) relative to the patient table during an exam, which is then sampled with equal probability to determine the starting spatial coordinates of particles being transported by the subroutine. This uniform sampling is appropriate, as the x-ray tube moves with uniform rotation time during an exam, and therefore has no position bias relative to the patient.

Generating Equivalent CT X-ray Energy Spectra

In order to generate the necessary probability data for photon energies, measurements of first and second half-value layers (HVL) (in mm Al) were made for each beam energy (80, 100, 120, and 135 kVp) and filter (small, medium, and large) setting combination. For the measurements, the scanner was placed in service mode with the x-ray tube parked at the 6 o'clock position (pointing upwards). A lead diaphragm was centered on the bottom of the gantry and a Radcal 10x6-6 general purpose ion chamber (Radcal, Monrovia, CA) was centered free-in-air at the beam isocenter using the scanner positioning lasers to ensure good geometry. Exposure measurements at 100 mAs were made with increasing thicknesses of aluminum until the exposure measured one-half and one-fourth of the initial unfiltered exposure (first and second half-value layers, respectively). A photograph of a similar setup can be found in Figure 2-1.

With these HVL data, "equivalent" x-ray spectra were generated using a methodology presented by Turner *et al*⁴³ that makes use of the SPEKTR tungsten anode spectrum generator code.⁴⁶ Using a custom MATLAB™ (The Mathworks Inc., Natick, MA) script and the SPEKTR code, an initially lower-energy tungsten (the typical material of CT x-ray tube anode targets) anode target spectrum was mathematically transmitted using ideal beam geometry assumptions through thicknesses of different typical inherent filter materials (aluminum, graphite, lead, titanium, and copper). The first HVL of this "candidate spectrum" resulting from transmission through the material was then calculated. A custom script was used to iteratively vary the material thickness until the resultant candidate spectrum had a calculated first HVL that matched that which was measured on the scanner (to within 0.00001 mm Al). This process was

repeated for all hardening materials to produce a first-HVL matched spectrum for each combination. The candidate spectrum that had a second HVL that most closely matched its measured value was then chosen as the “equivalent spectrum” for that energy and filter combination. These spectra were then entered into the MCNPX source subroutine as a set of probability bins for sampling initial x-ray energies during CT exam simulation. A graph of the first-HVL candidate spectra for the five materials for the 120 kVp and medium filter combination is shown in Figure 2-2.

Accounting for Beam-Shaping Filtration

In order to account for the shaping of the fan beam (perpendicular to the axis of rotation of the gantry) provided by the three different bowtie filters for each selectable kVp, beam profile measurements were made using a Radcal 10x6-3CT pencil ion chamber (Radcal, Monrovia, CA). The chamber was first suspended free-in-air at beam isocenter using a meter stick and the scanner positioning lasers, and the beam was parked in the 3 o’clock position (facing leftward). Exposure measurements of 100 mAs were then made for incrementally lower table positions until the table was 30 cm below isocenter. The setup for these measurements can be seen in Figure 2-3.

The exposure measurements were then normalized to the exposure at isocenter to create plots of relative x-ray intensity versus lateral position in the beam for each kVp and filter combination. These plots were assumed to be symmetric about the isocenter.

A modified Boltzmann function of the form:

$$f(x) = a1 + \frac{a2}{(1 + e^{\left(\frac{x-a4}{a5}\right)})^{a3}} \quad (2-1)$$

was then fit to each plot using a custom MATLAB™ script, where x is the distance from the centerline of the beam-shaping filter and a_1 through a_5 are fitting parameters. An example of raw profile data and the subsequent fit for 120 kVp can be seen in Figure 2-4. These functions were then added into the source subroutine in order to assign particle weighting factors based on the location of the simulated particles within the fan beam. One drawback to this method of modeling the beam-shaping filter as an intensity-modulation function coupled with a single equivalent energy spectrum is that it only accounts for the x-ray intensity changes introduced by the filter without accounting for corresponding changes in the x-ray spectrum. However, the use of this “virtual” bowtie filter modeling has been shown in the literature to not have a significant dosimetric accuracy impact as compared to explicit modeling of the bowtie filter’s shape and material composition.¹⁹

Beam Collimation and Overbeaming Determination

In order to characterize the actual overbeaming and penumbra region of a given nominal beam collimation, Gafchromic® XR-CT2 film strips (Ashland Inc., Covington, KY) were centered at the gantry isocenter using a meter stick with the beam parked at the 12 o’clock position (facing downward). An exposure was then made at 120 kVp, medium filter, large focal spot, and 200 mAs for the two collimation settings (64 x 0.5 mm and 32 x 0.5 mm) of interest as described in Chapter 1. Although the shape of the penumbra region may vary with energy and focal spot size, 120 kVp with a large focal spot was chosen as the representative data for these collimation settings, as these two settings are the most common for exams performed at the University of Florida Shands Hospital. Choosing the large focal spot is also a conservative assumption, as this will produce a larger penumbra region than given in the small focal spot setting.

After exposing the film strips, they were scanned using an Epson Stylus NX515 scanner (Seiko Epson Corporation, Suwa, Nagano, Japan) in greyscale mode at 300 dpi. These resulting images were then opened in the image analysis software ImageJ (National Institutes of Health, Bethesda, MD). An analysis line was then drawn across the exposed region of the film (as seen in Figure 2-5A for the 64 x 0.5 mm strip) and the “plot profile” feature of ImageJ was used to generate a list of pixel values across the line. Since the shades of the exposed regions of the film are linearly proportional to dose deposited (as claimed by the manufacturer), the corresponding pixels were assumed to be linearly proportional to the x-ray intensity impinging upon the film. The resulting pixel values from the analysis line were normalized to the maximum pixel intensity and imported into MATLAB™ and plotted (the 64 x 0.5 mm data can be seen in Figure 2-5B). As seen in the figure, the data takes the approximate shape of a trapezoid with a “full intensity” region with two sloped penumbra regions. The dimensions of these regions were found using MATLAB™ data analysis, with the resulting trapezoid seen for the 64 x 0.5 mm strip seen in Figure 2-5C. The results showed that for the 64 x 0.5 mm (or 3.2 cm) beam collimation, the full-intensity region was 3.6 cm with two 3 mm penumbra regions on either side. For the 32 x 0.5 mm (or 1.6 cm) beam collimation, the full-intensity region was 2.0 cm with two 2.5 mm penumbra regions on either side. This information was incorporated into the subroutine by allowing for user inputs of the total beam width (full-intensity plus penumbra regions) and total penumbra width (the addition of both penumbra region widths). These inputs then generate the appropriate trapezoid with a particle weighting of one for the full-intensity region, and linearly-decreasing weighting in the penumbra regions.

Beam Output Normalization Factors

With the previously-described probability data generated and incorporated within the MCNPX framework of Dr. Ghita's code, the source subroutine was completed and ready for performing x-ray transport. However, dose calculations performed using MCNPX give tallied results in mGy per starting photon, and thus in order to convert these tallies to values of absolute absorbed dose, Monte Carlo normalization factors were calculated that account for the total number of photons delivered by the scanner for each combination of beam parameters (kVp, bowtie filter, and beam collimation) per mAs of output. As mentioned earlier in this chapter, all measurements were made with a large focal spot as the majority of scan protocols use this setting, and this assumption provides conservative estimates of dosimetry. In order to calculate these factors, a Radcal 10x6-3CT pencil ion chamber (Radcal, Monrovia, CA) was positioned free-in-air and centered at isocenter (identical to the setup in Figure 2-3). A single axial rotation scan of 100 mAs was then performed for every energy, filter, and collimation setting combination of interest and the air kerma recorded for each. Dividing this air kerma by 100 gave the air kerma per mAs for each beam parameter combination. Using the completed source subroutine, simulations of these axial scans were performed, with the mGy per starting photon delivered to the active element of a model of the ion chamber calculated using an F6 energy deposition tally. A total of 100 million particle histories were run, with the resulting Monte Carlo uncertainties of the tallies all less than 0.1%. This tally assumes local energy deposition of generated secondary particles at the location of generation, which has been shown to be an acceptable assumption at diagnostic x-ray energies.⁴⁷ Dividing the measured exposures (in mGy per mAs) by those simulated (in mGy per photon) yielded normalization factors in units of photons

per mAs for each scan parameter combination. These normalization factors could then be used to convert calculated patient doses from Monte Carlo tallies to absolute tallies by multiplying the tallies in mGy per starting particle by the normalization factor and the total mAs delivered (mAs per rotation multiplied by total number of rotations) in the exam of interest.

Validating the Monte Carlo Model with CTDI Phantom Measurements

CTDI Phantom Measurements and Simulations

The usefulness of a Monte Carlo source model is dictated by its ability to accurately predict actual physical dose measurements. Consequently, to perform initial validation testing of the source term subroutine, a series of computed tomography dose index (CTDI) phantom measurements were made on the AQ1. CTDI phantoms come in two sizes, head and body, and are generally made of poly(methyl methacrylate) (PMMA). Each phantom is 15 cm deep with a diameter of 32 cm for the body phantom, and 16 cm for the head phantom. Both contain five holes, 4 evenly spaced at the periphery at 1 cm from the outer surface, and one at the center. These holes are sized to each accommodate the insertion of a 100 mm CT pencil ion chamber, which is what was used to perform dose measurements. When the chamber is placed in a specific hole for measurements, PMMA dowels are fitted to the remaining four holes to create a solid phantom without air gaps. The experimental setup involved laser centering the phantoms at scanner isocenter, with the four periphery holes lined up at azimuthal positions of 12, 3, 6, and 9 o'clock. This measurement setup for a center hole measurement on the body phantom can be seen in Figure 2-6. Air kerma measurements were then made with a Radcal 10x6-3CT pencil ion chamber (Radcal, Monrovia, CA) at each of the five hole positions for both phantoms. For the body

phantom, these measurements were made with all combinations of the following beam parameters: large focal spot, 100 mAs, beam energies of 80, 100, 120, and 135 kVp, medium and large bowtie filters (filters commonly used for body exams), and beam collimations of 32 x 0.5 mm and 64 x 0.5 mm. For the head phantom, these measurements were made with all combinations of the following beam parameters: large focal spot, 100 mAs, beam energies of 80, 100, 120, and 135 kVp, small bowtie filter (commonly used for head exams), and beam collimations of 32 x 0.5 mm and 64 x 0.5 mm. These two beam collimations were chosen as they represent the collimations of initial interest for a dose calculation program as discussed previously in Chapter 1. For each set of beam parameter combination measurements, the weighted CT dose index ($CTDI_w$) was calculated by the following formula:

$$CTDI_w (mGy) = \frac{\frac{2}{3} * \text{Average of Periphery Doses (mGy)} + \frac{1}{3} * \text{Center Dose (mGy)}}{\frac{\text{Nominal Beam Collimation (mm)}}{100 \text{ mm}}} \quad (2-2)$$

In order to be used for comparison purposes.

After the experimental CTDI measurements, the source subroutine was used to simulate each measurement configuration (beam parameter combinations and the ion chamber positioned within the five holes of the phantoms) are calculate air kerma in the ion chamber active element. The scanner table was modeled as carbon fiber in a shape geometrically defined by Dr. Ghita in her dissertation.⁴⁴ The simulation geometry for the body phantom with the ion chamber at the 12 o'clock position can be seen in Figure 2-7. A total of 100 million photon histories were run, with resulting Monte Carlo errors were all less than 0.3%.

Results

After generating all air kerma values, the measured and simulated values were compared using percent difference calculations of the following form:

$$\text{Percent Difference} = \frac{\text{Simulated Air Kerma} - \text{Measured Air Kerma}}{\text{Measured Air Kerma}} * 100 \quad (2-3)$$

The results for the body CTDI phantom can be seen in Tables 2-1, 2-2, and 2-3; and those for the head phantom in Tables 2-4, 2-5, and 2-6. Table 2-7 shows average magnitude and range summaries for both sets of results for 32 x 0.5 mm, 64 x 0.5 mm, and overall collimations.

Discussion and Conclusion

As seen in Table 2-7, there was good agreement for the body phantom measurements. All percent differences were within 6%, with average magnitudes all below 3%. There seems to be no dependence of the percent difference on any of the beam parameters used for these measurements. Overall, these results seemed to indicate a successful initial validation of the subroutine for body-sized objects with the medium and large bowtie filters.

The results for the head phantom also showed good agreement, but slightly poorer than those seen for the body phantom. All percent differences were within 11%, with average magnitudes all below 7%. Once again, there seemed to be no dependence of the percent differences with any particular scan parameter. However, there seems to be some sort of systematic error in the results, since all simulated air kerma values were greater than those measured. A possible explanation for this is the fact that the effects of phantom positioning at the isocenter play a much larger role with a smaller phantom and a smaller bowtie filter, as the edges of this phantom are right as

the sharpest slope of the bowtie-filter-induced intensity modulation. Any slight shifts in the positioning of the phantom could therefore impact the dose noticeably in this setup. Contrast this with the fact that in the MCNPX simulation, the phantom is always perfectly centered at isocenter (where the bowtie filter will deliver the highest doses), and it may shed some light on the greater discrepancies. A test for future work would be to take a sample set of measurements on the body phantom with the small filter selected, and a set of measurements on the head phantom with the medium and large filters selected to determine if the root cause of the discrepancies is indeed positioning errors. However, despite the larger differences, sufficient confidence was felt in the results to conclude that the subroutine had successfully passed initial validation and the research could move forward.



Figure 2-1. Half-value layer measurement equipment setup. Photo courtesy of Elliott Stepusin.

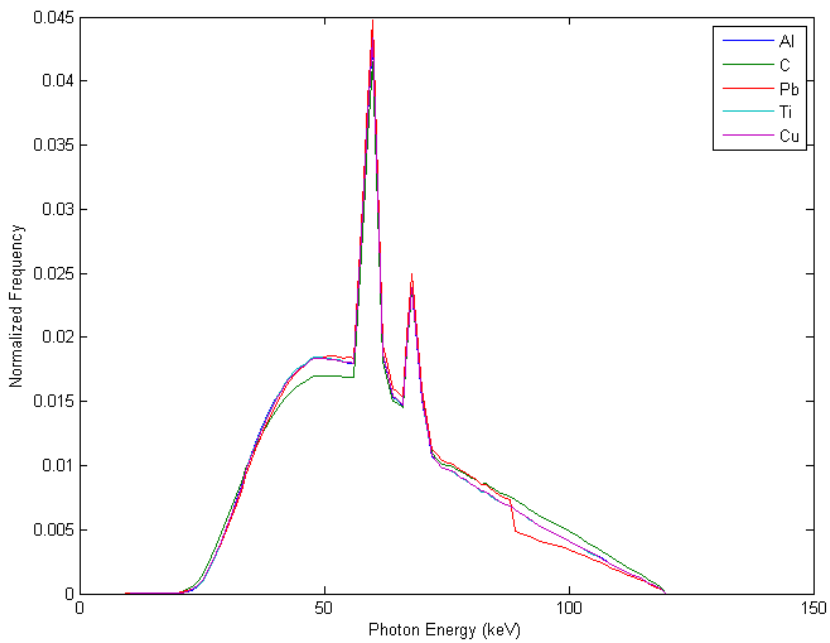
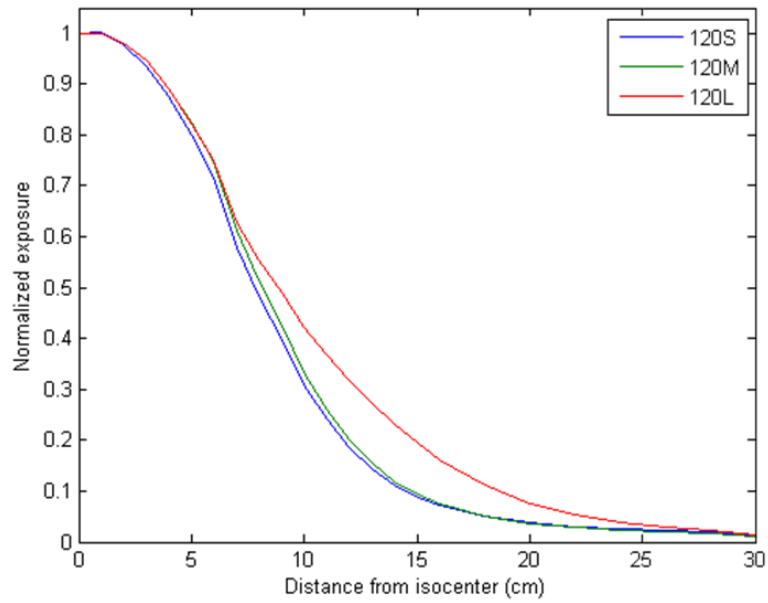


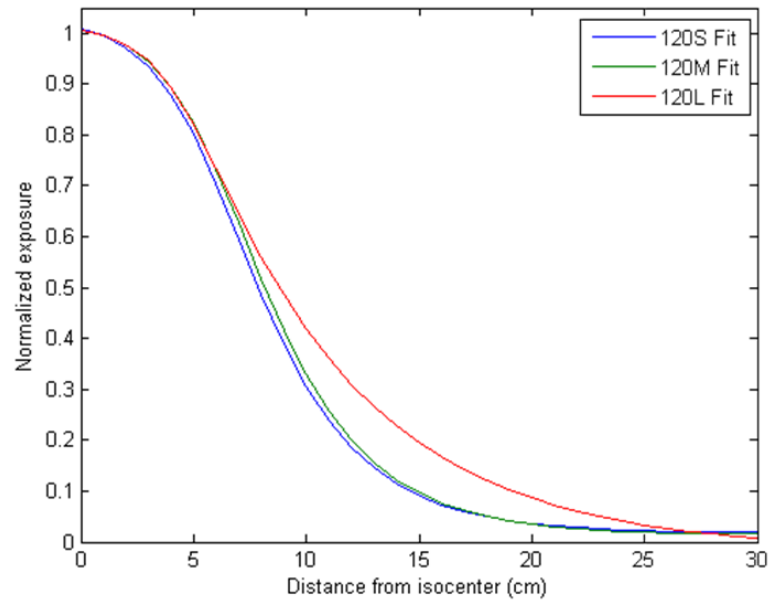
Figure 2-2. First HVL-matched candidate photon energy spectra for 120 kVp and medium bowtie filter.



Figure 2-3. Equipment setup for both beam profile and free-in-air measurements. Photo courtesy of Daniel Long.



A

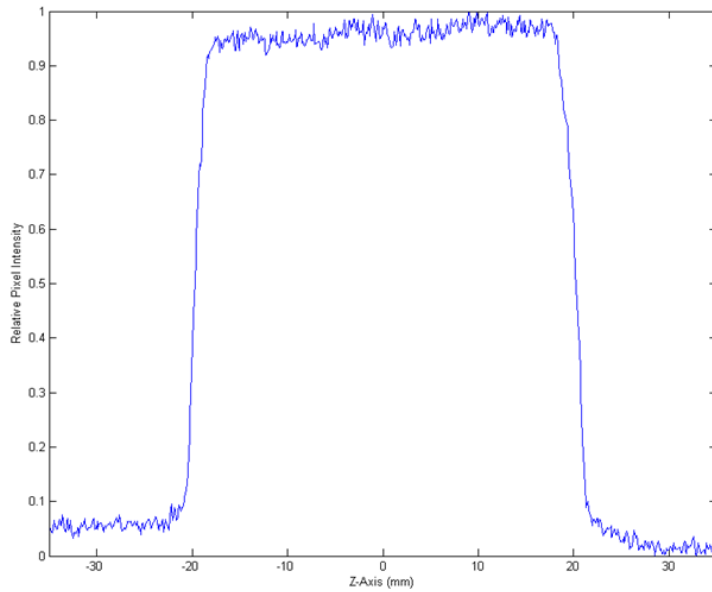


B

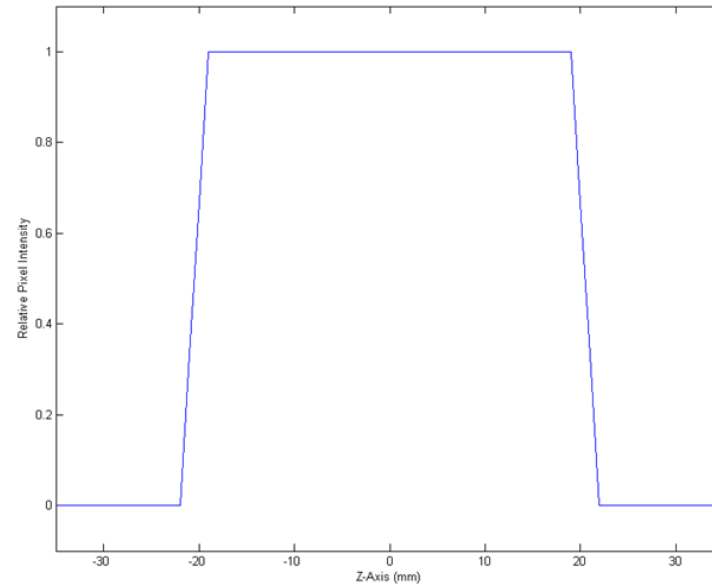
Figure 2-4. Beam profile data for 120 kVp beam energy. A) Raw data. B) Fitted functions.



A



B



C

Figure 2-5. Derivation of beam collimation weighting functions. A) Exposed film strip for the 64 x 0.5 mm beam collimation setting with yellow analysis line. B) Normalized pixel intensities along the analysis line. C) Resulting beam weighting trapezoid.

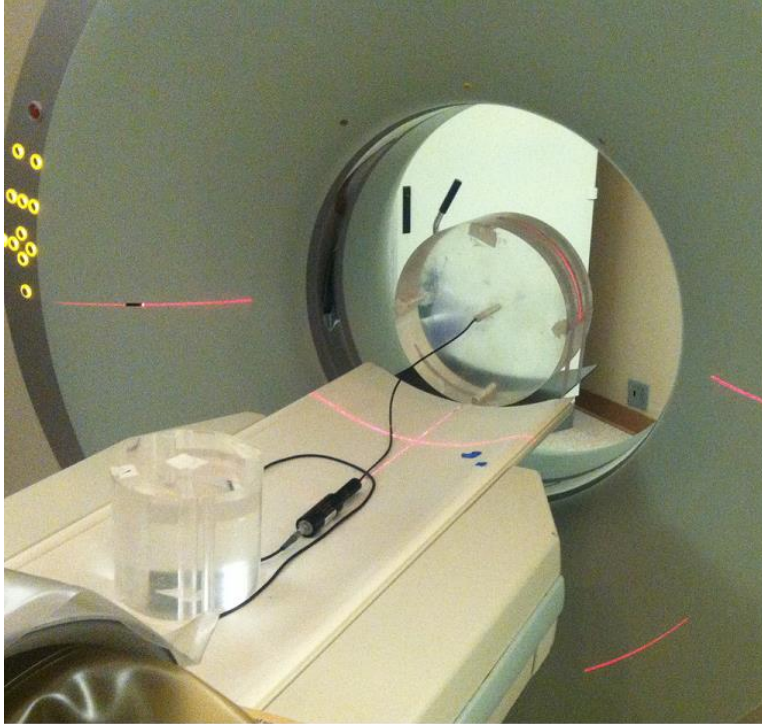


Figure 2-6. Body CTDI phantom center hole measurement setup. Photo courtesy of Elliott Stepusin.

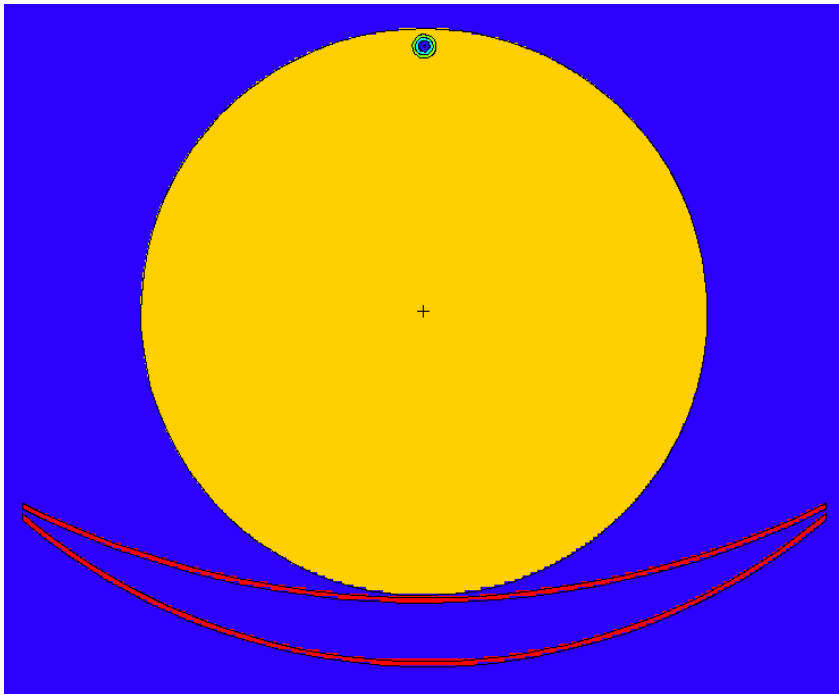


Figure 2-7. Body CTDI 12 o'clock hole position measurement MCNPX simulation geometry.

Table 2-1. Body CTDI phantom measurement results.

Energy (kVp)	Filter	Collimation	CTDI Position Measured Air Kerma (mGy)				CTDI _w	
			Center	3 o'clock	6 o'clock	9 o'clock		12 o'clock
80	M	32 x 0.5 mm	0.2	0.6	0.5	0.6	0.6	2.8
		64 x 0.5 mm	0.4	1.0	0.9	1.0	1.0	2.5
	L	32 x 0.5 mm	0.3	0.7	0.6	0.6	0.6	3.2
		64 x 0.5 mm	0.4	1.2	1.1	1.1	1.1	2.8
100	M	32 x 0.5 mm	0.5	1.1	1.1	1.1	1.1	5.7
		64 x 0.5 mm	1.0	2.0	1.9	1.9	1.9	5.0
	L	32 x 0.5 mm	0.6	1.3	1.2	1.2	1.3	6.4
		64 x 0.5 mm	1.0	2.3	2.1	2.2	2.2	5.6
120	M	32 x 0.5 mm	1.0	1.9	1.7	1.8	1.8	9.5
		64 x 0.5 mm	1.7	3.2	3.0	3.1	3.1	8.3
	L	32 x 0.5 mm	1.0	2.1	2.0	2.0	2.1	10.7
		64 x 0.5 mm	1.7	3.7	3.5	3.5	3.6	9.3
135	M	32 x 0.5 mm	1.4	2.5	2.4	2.4	2.4	13.0
		64 x 0.5 mm	2.3	4.4	4.1	4.2	4.2	11.2
	L	32 x 0.5 mm	1.4	2.9	2.7	2.8	2.8	14.7
		64 x 0.5 mm	2.4	5.1	4.7	4.8	4.9	12.6

Table 2-2. Body CTDI phantom simulation results.

Energy (kVp)	Filter	Collimation	CTDI Position Simulated Air Kerma (mGy)				CTDI _w	
			Center	3 o'clock	6 o'clock	9 o'clock		12 o'clock
80	M	32 x 0.5 mm	0.3	0.6	0.6	0.6	0.6	3.0
		64 x 0.5 mm	0.5	1.0	1.0	1.0	1.0	2.6
	L	32 x 0.5 mm	0.3	0.7	0.6	0.7	0.7	3.2
		64 x 0.5 mm	0.5	1.2	1.1	1.2	1.2	2.9
100	M	32 x 0.5 mm	0.6	1.1	1.1	1.1	1.1	5.8
		64 x 0.5 mm	1.0	2.0	1.9	2.0	2.0	5.1
	L	32 x 0.5 mm	0.6	1.3	1.2	1.3	1.3	6.4
		64 x 0.5 mm	1.0	2.2	2.1	2.2	2.2	5.6
120	M	32 x 0.5 mm	1.0	1.8	1.7	1.9	1.9	9.7
		64 x 0.5 mm	1.7	3.2	3.0	3.2	3.2	8.4
	L	32 x 0.5 mm	1.0	2.1	1.9	2.1	2.1	10.7
		64 x 0.5 mm	1.8	3.6	3.4	3.6	3.7	9.3
135	M	32 x 0.5 mm	1.4	2.5	2.3	2.5	2.5	13.1
		64 x 0.5 mm	2.4	4.3	4.1	4.3	4.3	11.4
	L	32 x 0.5 mm	1.4	2.8	2.6	2.8	2.8	14.5
		64 x 0.5 mm	2.5	4.9	4.6	4.9	4.9	12.6

Table 2-3. Body CTDI phantom percent difference results.

Energy (kVp)	Filter	Collimation	CTDI Position Air Kerma Percent Difference				CTDI _w	
			Center	3 o'clock	6 o'clock	9 o'clock		12 o'clock
80	M	32 x 0.5 mm	5.4	2.9	2.6	4.9	5.3	4.2
		64 x 0.5 mm	4.9	2.6	2.2	4.6	4.9	3.8
	L	32 x 0.5 mm	4.8	-0.3	-0.2	3.4	3.8	2.2
		64 x 0.5 mm	4.2	-0.2	-0.1	3.3	3.2	2.0
100	M	32 x 0.5 mm	1.9	0.4	0.3	3.7	3.5	2.0
		64 x 0.5 mm	1.4	0.8	0.1	3.4	3.4	1.8
	L	32 x 0.5 mm	0.6	-2.4	-2.2	2.5	1.8	0.0
		64 x 0.5 mm	0.1	-2.2	-2.1	2.1	1.7	-0.1
120	M	32 x 0.5 mm	2.6	-0.7	-0.3	3.6	3.2	1.7
		64 x 0.5 mm	2.9	-0.1	-0.4	3.8	3.2	1.9
	L	32 x 0.5 mm	2.0	-3.5	-2.8	2.2	1.7	-0.1
		64 x 0.5 mm	2.1	-3.1	-3.0	2.3	1.4	-0.1
135	M	32 x 0.5 mm	2.6	-1.7	-1.4	3.0	2.3	1.0
		64 x 0.5 mm	3.1	-1.2	-1.0	3.3	2.5	1.4
	L	32 x 0.5 mm	1.9	-4.7	-3.7	1.6	0.6	-0.9
		64 x 0.5 mm	2.5	-4.1	-3.4	2.0	1.0	-0.4

Table 2-4. Head CTDI phantom measurement results.

Energy (kVp)	Filter	Collimation	CTDI Position Measured Air Kerma (mGy)					CTDI _w
			Center	3 o'clock	6 o'clock	9 o'clock	12 o'clock	
80	S	32 x 0.5 mm	1.2	1.4	1.4	1.4	1.5	8.3
		64 x 0.5 mm	2.1	2.5	2.4	2.4	2.6	7.3
100	S	32 x 0.5 mm	2.2	2.5	2.5	2.5	2.6	15.2
		64 x 0.5 mm	3.9	4.5	4.3	4.4	4.6	13.3
120	S	32 x 0.5 mm	3.6	3.9	3.9	3.8	4.0	23.7
		64 x 0.5 mm	6.2	6.9	6.7	6.7	7.0	20.7
135	S	32 x 0.5 mm	4.7	5.2	5.1	5.0	5.3	31.3
		64 x 0.5 mm	8.2	9.0	8.8	8.7	9.2	27.1

Table 2-5. Head CTDI phantom simulation results.

Energy (kVp)	Filter	Collimation	CTDI Position Simulated Air Kerma (mGy)					CTDI _w
			Center	3 o'clock	6 o'clock	9 o'clock	12 o'clock	
80	S	32 x 0.5 mm	1.3	1.5	1.4	1.5	1.6	9.0
		64 x 0.5 mm	2.3	2.6	2.5	2.7	2.8	7.9
100	S	32 x 0.5 mm	2.4	2.7	2.6	2.7	2.8	16.0
		64 x 0.5 mm	4.2	4.7	4.5	4.7	4.9	14.1
120	S	32 x 0.5 mm	3.8	4.1	4.0	4.1	4.3	25.2
		64 x 0.5 mm	6.7	7.2	7.0	7.3	7.5	22.1
135	S	32 x 0.5 mm	5.1	5.4	5.3	5.4	5.6	33.2
		64 x 0.5 mm	8.8	9.4	9.1	9.4	9.8	28.9

Table 2-6. Head CTDI phantom percent difference results.

Energy (kVp)	Filter	Collimation	CTDI Position Air Kerma Percent Difference					CTDI _w
			Center	3 o'clock	6 o'clock	9 o'clock	12 o'clock	
80	S	32 x 0.5 mm	9.8	6.5	7.1	8.5	8.3	8.3
		64 x 0.5 mm	10.5	6.6	7.0	9.1	8.2	8.6
100	S	32 x 0.5 mm	5.9	4.5	4.2	7.0	6.6	5.7
		64 x 0.5 mm	6.3	4.4	4.1	7.3	6.6	5.8
120	S	32 x 0.5 mm	7.4	5.1	3.9	7.8	7.0	6.4
		64 x 0.5 mm	8.2	5.4	4.2	8.2	7.2	6.8
135	S	32 x 0.5 mm	7.1	4.7	3.4	7.4	6.7	6.0
		64 x 0.5 mm	8.2	5.1	3.7	8.0	6.9	6.6

Table 2-7. CTDI percent difference results summary.

	32 x 0.5 mm Collimation		64 x 0.5 mm Collimation		Combined	
	Body Phantom	Head Phantom	Body Phantom	Head Phantom	Body Phantom	Head Phantom
Range	(-4.7, 5.4)	(3.4, 9.8)	(-4.1, 4.9)	(3.7, 10.5)	(-4.7, 5.4)	(3.4, 10.5)
Average Magnitude	2.3 ± 1.5	6.5 ± 1.6	2.2 ± 1.4	6.8 ± 1.7	2.3 ± 1.5	6.6 ± 0.9

CHAPTER 3 DEVELOPMENT AND VALIDATION OF A MONTE CARLO ORGAN DOSE CALCULATION METHODOLOGY FOR TOSHIBA CT EXAMS WITH ATCM

Theoretical Basis for a Precalculated ATCM CT Dosimetry Approach

As described in Chapter 1, the major goal of any ATCM algorithm is to maintain a uniform, desired level of image quality throughout an exam while reducing patient dose as much as feasible. All major CT manufacturers have different proprietary approaches to their ATCM algorithms; nevertheless, at a fundamental level, all algorithms seek to adjust the tube current according to the attenuation of the patient “seen” by the beam at any given point along the scan length. This is especially true of Toshiba’s SureExposure™3D ATCM algorithm, where the mA “map” for an exam is precalculated based off of calculations of patient attenuation from anterior-posterior (AP) and lateral scanograms taken prior to the acquisition of the diagnostic CT image.

Therefore, characterizing the attenuation of a patient along scan ranges would be a good starting point in the development of a computational method of accounting for ATCM given a lack of access to proprietary algorithms. Fortunately, the slice-by-slice CT dosimetry methodology described in Chapter 1 lends itself well to this type of attenuation calculation. The premise of this technique would be to calculate an “attenuation weighting factor” for each axial beam slice in the pre-calculated organ dose database that would serve to redistribute the average effective mAs (all average of the tube currents over all projections in the exam multiplied by rotation time and divided by pitch) for an exam across the slices based upon patient attenuation. For example, for a chest-abdomen-pelvis (CAP) exam, the weighting factors for the slices corresponding to the anatomical extents of the exam would be selected, averaged, and normalized to the average. The slices containing the pelvis region (more attenuating) would then have

normalized factors above 1, while those in the chest region containing the lungs (less attenuating) would have factors below 1. These normalized weighting factors would then be multiplied by the average effective mAs for the exam, with the resulting slice-specific effective mAs values being used to scale the organ dose contributions from each slice up or down from the average effective mAs.

The difficulty, then, would be in finding a single, robust methodology to calculate weighting factors that will cover a wide variety of patients and protocols. An idea for an initial approach came in a journal article by Gies *et al.* in 1999 that presented a simplified mathematical derivation of an “ideal” mA modulation scheme.⁴² The authors mathematically proved through a simplified problem setup that in order to have a tube current modulation scheme that will provide the lowest uniform theoretical image noise, one must weigh the beam projections over the course of an exam relative to one another based upon the square root of the central ray attenuation of each projection (where attenuation is defined as the initial intensity of the central ray divided by the exit intensity from the patient for that projection). Since the precalculated dosimetry approach uses full 360° axial beam slices, a logical starting point was to calculate the weighting factors based on the average of the square roots of the central ray attenuation values for all projection angles in a single tube rotation of patient anatomy. Though this approach was for an “ideal” ATCM algorithm based on a simplified mathematical model, it was seen as a solid starting point for this investigation.

Cadaver CT Organ Dose Measurements Using OSL Dosimeters

The usefulness of any computational-based CT dosimetry approach lies solely in the ability to accurately predict experimental data. To this end, a large set of in-field CT dose measurements made on cadavers on the Toshiba Aquilion ONE by Lindsay

Sinclair for her dissertation research at Shands Hospital at the University of Florida were used to perform validation testing of the proposed pre-calculated ATCM algorithm. These measurements involved the surgical insertion of polyvinyl chloride (PVC) access tubes into three female cadavers in which optically-stimulated luminescence dosimeters (OSLDs) were placed in a process pioneered by Dr. Thomas Griglock in his dissertation research.⁴⁸ These tubes were placed by a board-certified radiologist into several internal organs of interest in each cadaver, including the thyroid, breasts, lungs, liver, stomach, small intestine, colon, uterus, and ovaries. The OSLDs were then placed into these tubes in such a manner as to achieve a wide range of anatomical coverage while encompassing variations in dose gradient seen by each organ of interest. All OSLD measurements had associated measurement uncertainties of within $\pm 5\%$.

The three cadavers upon which measurements were made had body mass indices (BMI) of 17.4, 35.2, and 43.9; henceforth in this chapter, the three cadavers will be referred to as the small (BMI 17.4), medium (BMI 35.2), and large (BMI 43.9) subjects. For this study, dose data for the cadavers were taken from Ms. Sinclair for four common standardized Shands Hospital body imaging protocols with ATCM: CAP, chest, abdomen, and pelvis. Additionally, one CAP exam on the large cadaver was performed without ATCM to provide data for an initial test of dose accuracy before the ATCM algorithm itself was enabled. All exams were performed at a beam collimation of 64 x 0.5 mm, as this is the collimation of most interest for the development of the pre-calculated dose database software described in Chapter 1. The associated scan ranges and parameters used for each cadaver and protocol can be found in Figure 3-1 and Table 3-1 (CAP), Figure 3-2 and Table 3-2 (chest), Figure 3-3 and Table 3-3

(abdomen), and Figure 3-4 and Table 3-4 (pelvis). It should be noted that in these tables, both the console-reported average effective mAs and that which was derived from the images themselves are shown for each protocol. The discrepancies between these numbers are an important factor to be discussed later in this chapter.

Creation of Cadaver-Based Computational Voxel Phantoms

In order to perform dosimetry simulations for the three cadavers for which OSL dose measurements were made, it was necessary to create computational voxel phantom “twins” for each in order to be able to be read properly into MCNPX. The multi-step process to create these phantoms involved segmentation of image sets, 3D model rendering, and voxelization.

The first step in the creation of these computational phantoms was the segmentation of three special CT image sets of the cadavers provided by Lindsay Sinclair. The scans taken to produce these image sets involved scanning anatomy just beyond the starting and ending anatomical landmarks encompassing a standardized CAP exam, as well as the placement of fiducial markers at the location of each OSLD used in the dose measurements described previously in this chapter. These markers are clearly visible in the resulting image sets, allowing for precise location knowledge in relation to the cadaver anatomy. The image sets were imported into 3D-DOCTOR™ (Able Software Corp., Lexington, MA), a 3D modeling and image processing software for tomography data. Within the software, two sets of anatomical structures of the cadavers were segmented in order to create contours for the resulting phantoms. The first set of structures included soft tissue, lung tissue, skeletal tissue, the air-filled tubes housing the dosimeters, and the fiducial markers. The second set included all but the fiducial markers with the addition of the breasts, liver, stomach, uterus, and ovaries. An

example of a segmented image can be seen in Figure 3-5. These contour sets were then rendered and exported in a Wavefront Object file format and imported into Rhinoceros™ (McNeel North America, Seattle, WA), a non-uniform rational B-spline (NURBS) modeling, rendering, and analysis software.

Within Rhinoceros™, the different structures of the contours were uniquely tagged with ID numbers, with the segmented fiducial markers each replaced by uniform spheres of 1 cm diameter. A frontal and lateral view of the medium cadaver with outer body contour, placement tubes, and dosimeter spheres visible can be seen in Figure 3-6. After all structures were tagged, the rendered phantoms were then imported into an in-house voxelizing program, which converted the phantoms into a series of $2 \times 2 \times 2$ mm³ voxel elements, which were each tagged with the ID number corresponding to the anatomical structure of which it was a part. These “voxelized” phantoms were then imported into an in-house MCNPX lattice generator, which converted the phantoms into a readable format for MCNPX. Each phantom was simplified into four material definitions for MCNPX simulations: International Commission on Radiological Protection (ICRP) Report 89 homogenous soft tissue (density 1.03 g/cm³) for all organs, dosimeters, and adipose and muscle tissue; ICRP Report 89 homogenous lung tissue (density 0.33 g/cm³) for the lungs; Oak Ridge National Laboratory Report 8381 homogenous bone tissue (density 1.4 g/cm³) for the skeleton; and National Institute of Standards and Technology (NIST) dry air (density 0.001205 g/cm³) for the dosimeter placement tubes.^{16,49}

The final products of this process were six total cadaver phantoms, with two versions of each of the small, medium, and large cadavers. The first version contained

soft tissue, skeleton, placement tubes, and dosimeter spheres to be used in point-to-point dose comparisons. The second version had no dosimeters but instead contained segmented organs to be used in volumetric dosimetry comparisons.

Cadaver ATCM CT Dosimetry Methodology

Slice Dosimetry Calculations

The first step taken in implementing this initial ATCM approach was to perform slice-based point and organ dosimetry on all six cadaver phantoms. Within MCNPX, each phantom was placed on top of the scanner table model described in Chapter 2. The Toshiba AQ1 source subroutine was placed in single axial slice acquisition mode with a 120 kVp beam, the large bowtie filter, and a 64 x 0.5 mm beam collimation, as these parameters were common for all cadaver and protocol combinations. The first slice input had the beam centered 1.6 cm from the cranial end of the phantom, with the next slice shifted 1.6 cm caudally until the slice location reached the caudal end. Although the beam width was 3.2 cm, this 1.6 cm spacing gave finer positioning flexibility when seeking the anatomical landmarks that define the scan ranges of the four protocols of interest. When the starting slice for a protocol was found, only every second slice after that starting slice would contribute to the dosimetry calculation in order to avoid slice overlap. For each slice input, F6 dose deposition tallies were calculated for all sphere dosimeters or organs, depending on the phantom type; and were converted to absolute dose per mAs using the proper Monte Carlo normalization factors. Additionally, 100 million particle histories were run to keep all tally uncertainties for organs or dosimeters within the bounds of the slice (in-field) to less than 2%. After these inputs were completed, the starting and ending slices of each protocol for each cadaver were determined by finding the z-axis coordinate location of the start and end

anatomical landmarks of interest for each exam type by using the built-in MCNPX visualization tool. The sets of slices that provided the closest match to the scan ranges of interest based on the anatomical coordinates and those of the slices themselves were then noted and used for the remainder of the dose calculation process. The effects of over-ranging were not taken into account in this calculation method, as investigations into their exact behavior for exams on the Aquilion ONE were still under investigation at the time. Integration of these effects will be addressed in future studies.

Large Cadaver Fixed Tube Current Dosimetry

Before beginning the ATCM study, it was decided that it would be beneficial to run dosimetry for an exam with a fixed tube current (without ATCM) in order to assess the accuracy of the subroutine within the slice-by-slice framework for a more complicated phantom geometry. As mentioned in previously, one CAP exam was performed on the large cadaver with constant effective mAs with parameters shown in Table 3-1. Computationally, the slices within the CAP range for the large cadaver were selected and their corresponding point and organ doses were scaled based on the effective mAs of the exam. The effective mAs is used to scale the axial slice dose values due to the fact that it is an approximate measure of the total amount of mAs delivered to each beam-width-wide slice of patient anatomy. After this slice dose scaling, all slice dose results were summed in the CAP range in order to calculate the final computational dose values for the exam. Three sets of doses were calculated: (1) point detector doses to be compared with the OSLD doses measured in the corresponding location in the cadaver, (2) in-field organ doses calculated from averaging the point doses located in each organ to be compared with the measured averages, and (3) volumetric in-field organ doses to be compared with the measured

averages. It should be noted that for the average organ doses, “in-field” refers to those organs that had more than one-half of their dose points within the primary fan beam during the exams.

Attenuation Calculations

The next step of the study was to create methods of calculating the attenuation of each slice of the cadavers in order to create candidate attenuation weighting factors for dosimetry. The subroutine allowed for “parking” the beam at fixed projection angles, so the question was then how to make detectors and choose tallies such that the attenuation described in Gies *et al.* (defined as the initial intensity of the central ray divided by the exit intensity from the patient for that projection) could be determined. The answer was a matter of mathematics. MCNPX tallies already gave results normalized to some initial intensity (per starting particle). Consequently, as long as this initial intensity was identical for every projection in every slice, all that would be required would be to create a detector opposite the patient from the beam and tally an approximate measure of exit intensity (such as fluence or air kerma) and then take the multiplicative inverse of the result (to units of starting particle per exit fluence or kerma). This would then satisfy the desired definition of attenuation that would still capture the relative differences between projections and slices.

To this end, six different virtual detectors (three types with two variants each) were designed in the hope of capturing attenuation values from which one would prove most adequate for final organ dosimetry under ATCM. The three major types were a central ray detector (1 cm wide in the x-y plane), an eighth circular arc detector, and a quarter circular arc detector all defined as air and placed 30 cm from the isocenter of the beam for each projection. Eight projection angles (0°, 45°, 90°, 135°, 180°, 225°,

270°, and 315°) for the beam were chosen to better sample the attenuation differences in the x-y plane of the slices, with the detectors centered opposite the patient from the incident beam. The beam itself was given identical parameters as defined previously (120 kVp, large bowtie filter, and 64 x 0.5 mm collimation). The two variants of each detector were in the width of each in the z-axis: the “thin” variant was centered on the slice and measured 1 cm, and the “wide” variant encompassed the entire 3.2 cm of slice width. The detectors were all 2 cm wide in the radial direction, with the first millimeter used for an F4 fluence tally, while the full 2 cm was used for an F6 air kerma tally. Therefore, a total of 12 different attenuation values (six detectors with two tally types) were calculated for each of the eight projection angles around each slice. A total of 10 million particle histories were run for each calculation, keeping the tally uncertainties all below 4%. Fewer particles were run for the attenuation calculations due to the large volume of inputs (over 7,000) required for the study. Figure 3-7 shows the central ray detectors at the eight projection angles for a chest slice in the small cadaver, and Figures 3-8 and 3-9 show the eighth arc and quarter arc detectors, respectively, for a 6 o'clock beam position for the same slice.

ATCM CT Dosimetry and Analysis

Image-based ATCM dosimetry

Before final dosimetry calculations could be completed, information regarding the tube current delivered for each exam protocol for each cadaver needed to be gathered. Displayed on each image of an exam image set was the average tube current used to create that image; therefore, recording the tube current for each image and averaging provided a value for the average tube current delivered for the entire exam. Multiplying this value by the single rotation time and dividing by the pitch gave the average effective

mAs for that exam. With the reconstructed image thicknesses known, it was also possible to plot the tube current versus the z-axis location on the patient. The plots will henceforth be referred to as “tube current maps”.

With those data gathered, two sets of “image-based” doses were calculated for comparing to the proposed attenuation calculation methodology. The first data set assumed a fixed effective mAs for each exam equal to the average effective mAs derived from the images sets. The purpose of this dose set was to determine dosimetric inaccuracies associated with using a traditional slice-by-slice dose methodology without accounting for the ATCM effects of the exams. The second set of doses used the actual tube current maps for each exam to assign effective mAs values to each dosimetric slice. Such an approach has been used in computational ATCM dosimetry before in the literature,^{23,25,26,37,38} and this second comparison helped benchmark its effectiveness versus a calculated attenuation methodology.

Calculated attenuation ATCM dosimetry

Once all dosimetry and attenuation calculations were performed for all three cadavers, a custom MATLAB™ script was written to perform the final set of dosimetry calculations incorporating ATCM and to analyze the results. The script read in the slice dosimetry data, the slice attenuation data, and the slice ranges and average effective mAs for each protocol, as well as the actual measured dose data for each of the three cadavers. The script then calculated 12 attenuation weighting factors per slice (corresponding to the six detectors and two tally types) by taking the inverse square root of each tally result of the eight angular projections and then averaging them together. With these attenuation weighting factors, both point and organ doses were calculated

for every cadaver and protocol combination by redistributing the effective mAs of each slice based on the normalized weighting factors within the slice ranges of interest.

As with the fixed tube current study, three sets of dose data were calculated: point detector doses to be compared with the OSLD doses measured in the corresponding location in the cadaver, in-field organ doses calculated from averaging the point doses located in each organ to be compared with the measured averages, and the in-field volumetric organ doses to be compared with the measured averages. Once again, “in-field” refers to those organs that had more than half of their dose points within the primary beam during CT examination.

Results and Discussion

Due to the large amount of data tables generated as part of this study, only the summary tables for the results will be presented in this chapter. The full set of data tables can be found in Appendix A. For all studies, the percent differences between simulated and measured doses were defined by the following equation:

$$\text{Percent Difference} = \frac{\text{Simulated Dose} - \text{Measured Dose}}{\text{Measured Dose}} * 100 \quad (3-1)$$

Fixed Tube Current CAP Exam

The summary of percent difference results for the fixed tube current CAP exam on the large cadaver can be found in Table 3-5. The overall results indicate good agreement with the measured data, with average magnitudes of the percent differences all below 15%. This agreement is acceptable, especially considering all the sources of uncertainty inherent to this study, especially those associated with experimental versus simulated exam positioning and geometry (including modeling a helical exam as an axial one with adjusted mAs values), and the simplified material assumptions made for

the cadaver and dosimeters. The average organ doses calculated from the segmented organ volumes outperformed the other two dose methods, and this result was anticipated. The reason is the fact that point dose calculations are much more susceptible to deviations between in-cadaver dose gradients of experimental and simulated exams than a volumetric dose target. This increased accuracy is promising, as volumetric organ dosimetry is what will be used in a future CT dosimetry software package.

Despite these encouraging results, the majority of the percent differences for all doses were negative. This may be in part due to the material assumptions made about the cadaver, especially assuming the majority of cadaver tissues were solid homogenous soft tissue at a density of 1.03 g/cm^3 , and assuming the lungs had a density of 0.33 g/cm^3 . In reality, there was some noticeable heterogeneity in the cadaver tissues apart from that which is expected in normal anatomy. The main source of this heterogeneity was small pockets of decay gases visible in the cadaver images that were so small and numerous that individually segmenting them would have been time prohibitive. The assumption that the lungs had a “fully-inflated” density (as patients are told to hold their breath during a CT exam), is most likely another source of error. The cadavers’ lungs were fluid-filled, so this assumption may have significantly underestimated the true density of the lung. In both cases, further investigation is warranted into these material assumptions in future work.

Determination of the Best Attenuation Weighting Factor Calculation Method

After doses for all cadavers and exams using the 12 attenuation weighting factors were calculated, they were compared with the corresponding experimentally measured doses. A large-scale statistical analysis was then undertaken, calculating the

average magnitudes of percent differences, their standard deviations, and minimum and maximum ranges for all sets of doses (3 cadavers x 4 exam types x 3 dose calculation types x 12 weighting factor methods = 432 total dose sets). Based on those statistical measures (weighted most by average magnitude, then standard deviation, then range), the top three weighting factor methods were selected for the 36 exam dose set combinations. From this list, it became clear that the “thin” quarter circular arc detector with kerma tallies was the ideal choice for weighting factor calculation, as it occupied the top three for nearly every exam dose set, most often in first or second position.

Comparison of Tube Current Maps

After selecting the thin quarter circular arc kerma detector as the best weighting factor calculation method, plots of the CAP exam tube current based on the weighting factors versus the patient z-axis location were made for each cadaver. Also present on these plots were the actual tube current maps from the CAP image sets, as well as the average tube current derived from the images. Figures 3-10, 3-11, and 3-12 contain the plots for the small, medium, and large cadavers, respectively. The CAP exam was chosen for this comparison as it contained the largest variability in attenuation values across the scan range.

All three cadavers’ simulated maps exhibited correct behavior regarding the tube current and the different regions of the patient anatomy. The tube current remained below the average in the less-attenuating chest region containing the lungs, rose to above average in the abdominal region, and peaked in the pelvic region. There were varying degrees of success in the simulated maps matching the actual maps. The small cadaver matched best, followed by the medium cadaver, and finally the large cadaver. A potential reason for this varying degree of matching comes to mind. The Toshiba

SureExposure™ 3D ATCM algorithm utilizes minimum and maximum tube current value limits to avoid under- and overexposures during an exam, which can override the underlying attenuation differences along the patient's z-axis. The algorithm presented in this work does not take these potential limits into account, and thus discrepancies could arise.

Ultimately, the degree of matching the tube current maps matters less than the actual dosimetric results from the study. However, if there are significant percent differences in the simulated doses as compared to those measured, analyzing the tube current maps may be a good starting point for adjusting the methodology to give better results.

CT Exams with ATCM

After analyzing the tube current maps, the cadaver organ dose percent difference data for the thin quarter arc kerma detector for all exams were collated and summarized in tables. Table 3-6 contains the summary percent difference data collected over all four exam types (including those for the fixed tube current and imaged-based attenuation dose calculations) for point dose, average organ doses from points, and volumetric organ doses for the small cadaver. Table 3-7 contains the same data for the medium cadaver, and Table 3-8 contains the same data for the large cadaver. Figures 3-13, 3-14, and 3-15 visually illustrate the percent difference summary data for the small, medium, and large cadavers, respectively. In these graphs, "Fixed Tube Current" refers to dose calculations made assuming a constant effective mAs for all slices equal to the average effective mAs for the exams; "Image-Based Attenuation" refers to dose calculations made by directly applying the actual tube current values taken from the images themselves; and "Calculated Attenuation" refers to dose calculations made

using the attenuation methodology presented in this chapter. The data from all four exam types were not separated for the percent difference summaries because the variations in the percent difference behavior between exams was minimal, as can be seen by referring to the tables presented in Appendix A.

Looking at the summarized data reveals several trends. First and foremost, the data for the attenuation calculation methodology had good agreement with the measured data across all three cadavers. The average magnitudes of the percent differences were all below 20%, with the majority below 15%. Despite the fact that the standard deviations on these averages are high even at maximum uncertainty, the averages are all below 30%, with the majority below 25%. As expected, the calculated attenuation method produced better results on the whole over that using the fixed tube current method, especially for the large cadaver. Despite the average magnitudes of the percent differences for the fixed tube current not being much higher than those of the calculated attenuation, the wider range of percent difference values indicates that it is a less accurate method. Another promising result was the fact that the calculated attenuation method matched very closely with the image-based attenuation method results, as the image-based attenuation should theoretically have the best results as it involves reading in the exact tube current data for the exam. This preliminary data indicates that as long as the average effective mAs is known for an exam, accessing all the images in order to derive the correct tube current along the patient z-axis (a much more involved task than inputting a single number as with the calculated attenuation method) is unnecessary and does not ensure higher dose accuracy. This would especially be useful for retrospective patient dosimetry for epidemiological studies,

where the images may not be available for the patient, but scan parameters and exam types might.

Another expected trend was the fact that the methodology was more accurate for the calculation and comparison of average organ doses as opposed to point doses. Volumetric organ geometries respond much less drastically to inconsistencies between the experimental and simulated exams, as they usually span multiple beam slices and occupy a much greater range of dose gradients than small point doses. Therefore, slight positioning errors or discrepancies between actual and simulated tube current maps impact the overall average dose much less than would be for point doses. This is also a promising result, as the future dosimetry methodology used for the ALRADS CT dose software will be using volumetric organ dose tallies; thus ensuring higher accuracy.

A final point to make is the fact that there did not seem to be that systematic dose overestimation as seen in the results for the fixed tube current CAP exam on the large cadaver, nor any other systematic pattern of percent error within a particular exam. This disappearance of the trend should be further investigated with future measurements using the UF reference physical phantoms for which material compositions are less uncertain as compared with those of the cadavers.¹⁵

Scanner Console Versus Image-Derived Average Effective mAs Values

It is important to note that the value of the average effective mAs for an exam varies significantly between that which is displayed on the scanner console after an exam, and that which is derived and calculated from the tube current values displayed on the images (see Figures 3-1 to 3-4). In all cases for this study, the console values were much greater than those derived from the exam images. It is unclear as to why

there is this discrepancy, but the important point to note is that using the console-given value for dosimetry results in significantly high percent differences when compared with the measurement data. Table 3-9 shows summarized percent difference data over all exam types for the calculated weighting factor method of dosimetry for the small cadaver using the average effective mAs values reported by the scanner for each exam. The resulting data is essentially unusable due to the high percent differences; therefore, it is necessary to derive these values from the images themselves for proper patient dosimetry until such a time that the scanner can report these corrected values on the console.

Conclusion

The overall results of this study suggest that this preliminary test of a precalculated dosimetry methodology incorporating ATCM has been a success. Given all the sources of uncertainty, including discrepancies in experimental and simulated exam parameters and positioning as well as assumptions regarding cadaver tissue composition and density in the simulations, the majority of the average percent difference values remained below 14%. Additionally, the volumetric organ dose comparison yielded average percent differences all below 12.5% for each cadaver. This methodology of organ dose calculation is identical to what would be used in a precalculated organ dose database program, so that result is promising. The results also show good agreement of the presented methodology with the common practice of extracting the tube current information from the image data itself to manually apply it in the dosimetry calculation. The results of this study indicate that this methodology could be used to faithfully reconstruct patient organ dosimetry in the case where the exact image sets are not available, but an idea as to the average effective mAs is known. If

perhaps one day scanner manufacturers start displaying on the console post-exam the average effective mAs as derived from the images themselves, it would make incorporating this method into the clinic even easier. Though more work needs to be done to further refine this methodology, it can be considered feasible and a solid foundation for such precalculated CT dosimetry methods incorporating attenuation calculations.

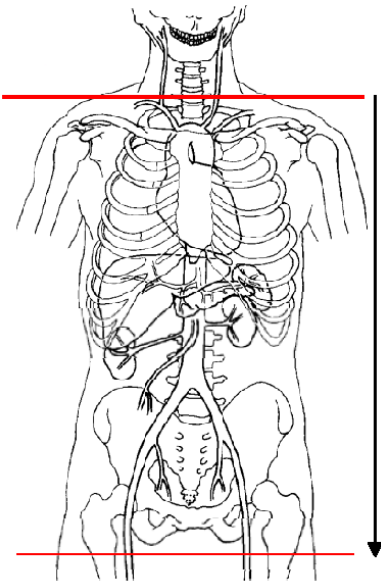


Figure 3-1. Chest-abdomen-pelvis exam scan range (thoracic inlet to lesser trochanter).

Table 3-1. Chest-abdomen-pelvis exam scan parameters.

Scan Parameters	Small Cadaver	Medium Cadaver	Large Cadaver	Large Cadaver
Body Mass Index	17.4	35.2	43.9	43.9
Beam Energy (kVp)	120	120	120	120
Bowtie Filter	Large	Large	Large	Large
Focal Spot	Small	Large	Large	Large
Beam Collimation	64 x 0.5 mm	64 x 0.5 mm	64 x 0.5 mm	64 x 0.5 mm
Rotation Time (s)	0.5	0.5	0.5	0.5
Pitch	0.828	0.828	0.828	0.828
SureExposure™ 3D enabled?	Yes	Yes	Yes	No
Average Effective mAs (Console)	154	302	302	254
Average Effective mAs (Image-Derived)	85	255	251	254
Scan Length (mm)	635	600	700	700

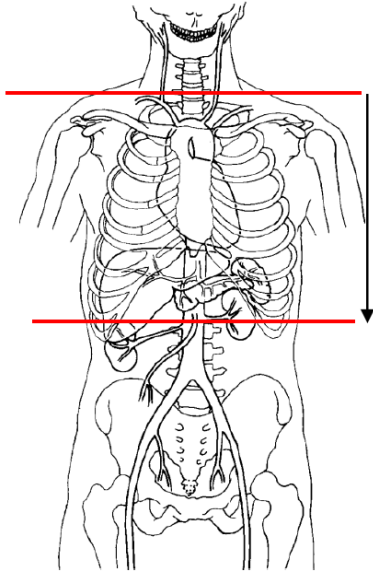


Figure 3-2. Chest exam scan range (thoracic inlet to top of kidneys).

Table 3-2. Chest exam scan parameters.

Scan Parameters	Small Cadaver	Medium Cadaver	Large Cadaver
Body Mass Index	17.4	35.2	43.9
Beam Energy (kVp)	120	120	120
Bowtie Filter	Large	Large	Large
Focal Spot	Large	Large	Large
Beam Collimation	64 x 0.5 mm	64 x 0.5 mm	64 x 0.5 mm
Rotation Time (s)	0.5	0.5	0.5
Pitch	1.484	1.484	1.484
SureExposure™ 3D enabled?	Yes	Yes	Yes
Average Effective mAs (Console)	95	169	169
Average Effective mAs (Image-Derived)	56	155	149
Scan Length (mm)	360	360	360

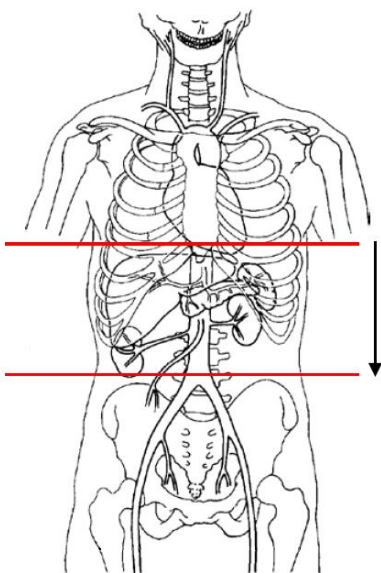


Figure 3-3. Abdomen exam scan range (dome of diaphragm to iliac crest).

Table 3-3. Abdomen exam scan parameters.

Scan Parameters	Small Cadaver	Medium Cadaver	Large Cadaver
Body Mass Index	17.4	35.2	43.9
Beam Energy (kVp)	120	120	120
Bowtie Filter	Large	Large	Large
Focal Spot	Large	Large	Large
Beam Collimation	64 x 0.5 mm	64 x 0.5 mm	64 x 0.5 mm
Rotation Time (s)	0.5	0.5	0.5
Pitch	0.828	0.828	0.828
SureExposure™ 3D enabled?	Yes	Yes	Yes
Average Effective mAs (Console)	133	302	302
Average Effective mAs (Image-Derived)	79	252	241
Scan Length (mm)	250	302	300

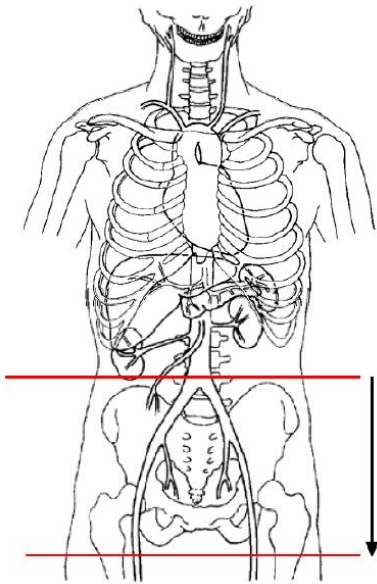


Figure 3-4. Pelvis exam scan range (iliac crest to lesser trochanter).

Table 3-4. Pelvis exam scan parameters.

Scan Parameters	Small Cadaver	Medium Cadaver	Large Cadaver
Body Mass Index	17.4	35.2	43.9
Beam Energy (kVp)	120	120	120
Bowtie Filter	Large	Large	Large
Focal Spot	Small	Large	Large
Beam Collimation	64 x 0.5 mm	64 x 0.5 mm	64 x 0.5 mm
Rotation Time (s)	0.5	0.5	0.5
Pitch	0.828	0.828	0.828
SureExposure™ 3D enabled?	Yes	Yes	Yes
Average Effective mAs (Console)	151	302	302
Average Effective mAs (Image-Derived)	98	241	259
Scan Length (mm)	250	302	250

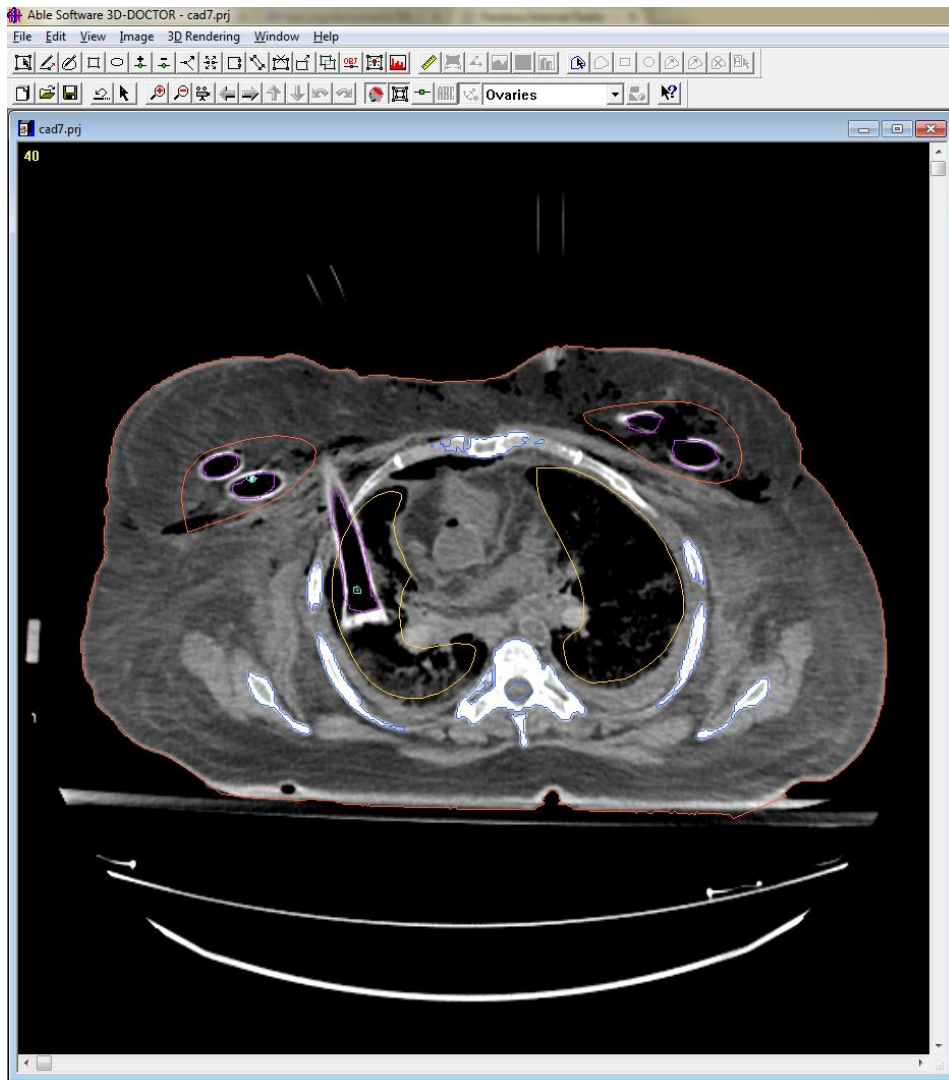


Figure 3-5. Segmented image of the medium cadaver in 3D-DOCTOR™. The peach line is for outer body contour, the orange for breast tissue, the purple for the placement tubes, the yellow for lung tissue, the blue for skeleton, and the teal for OSLD locations.

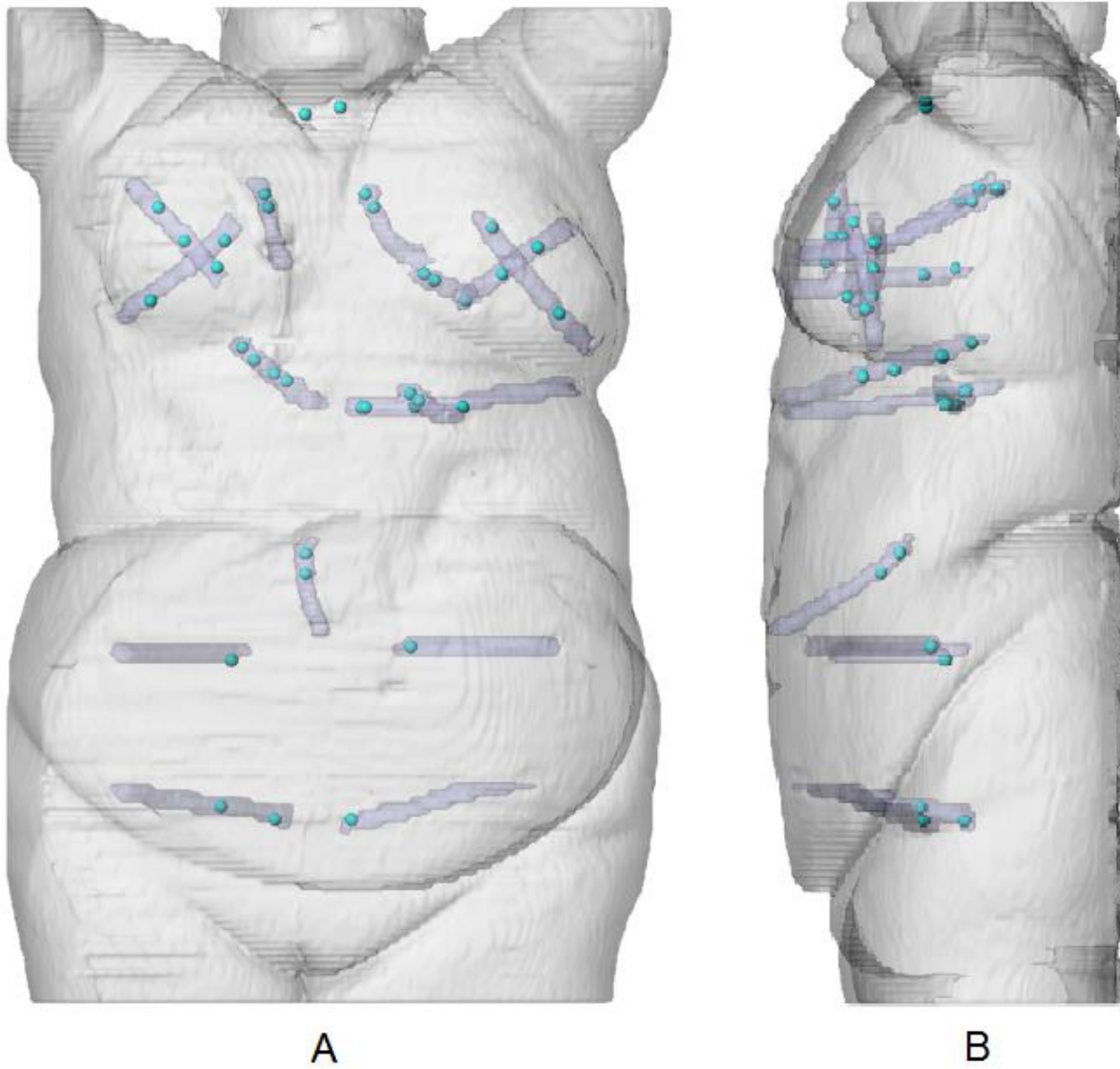


Figure 3-6. Medium cadaver phantom's outer body contour, placement tubes, and dosimeter locations. A) Frontal view. B) Left lateral view.

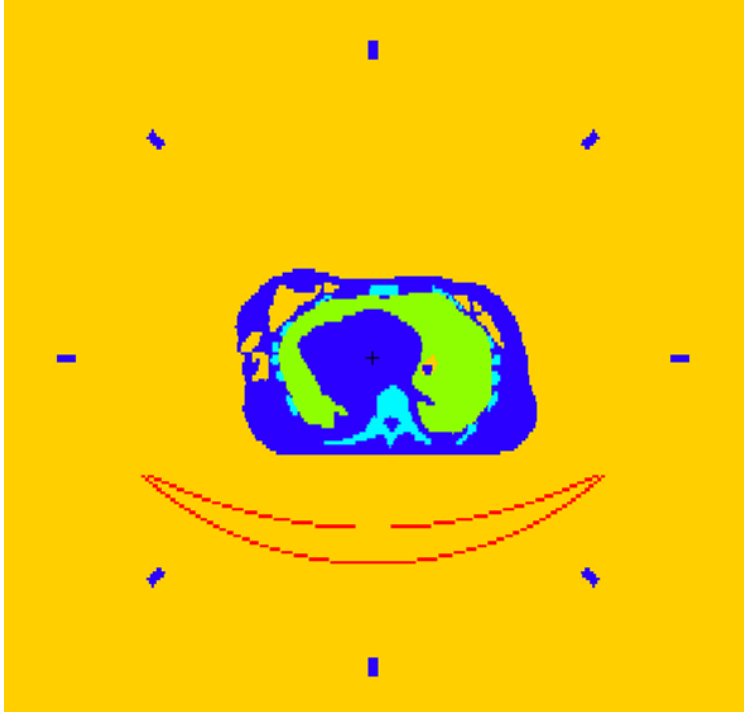


Figure 3-7. MCNPX visualization of the central ray attenuation detectors at all eight beam projection angles for a chest slice of the small cadaver phantom.

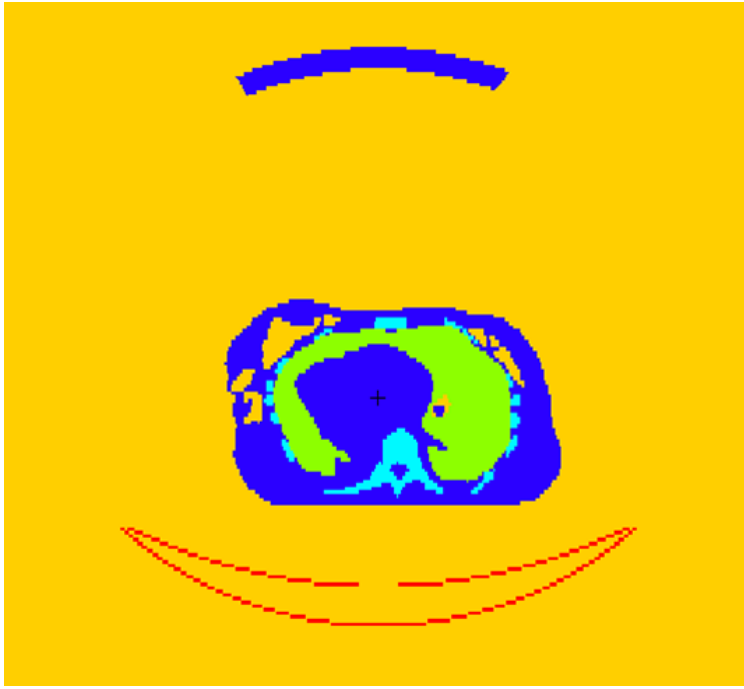


Figure 3-8. MCNPX visualization of the eighth circular arc detector for a 6 o'clock beam projection for a chest slice of the small cadaver phantom.



Figure 3-9. MCNPX visualization of the quarter circular arc detector for a 6 o'clock beam projection for a chest slice of the small cadaver phantom.

Table 3-5. Fixed tube current CAP exam percent difference summary for the large cadaver.

	Point Doses	Organ Doses from Points	Volume Organ Doses
Range	(-28.8, 25.7)	(-23.5, 23.8)	(-20.2, 4.0)
Average Magnitude	13.0 ± 8.2	14.2 ± 8.1	11.6 ± 7.2

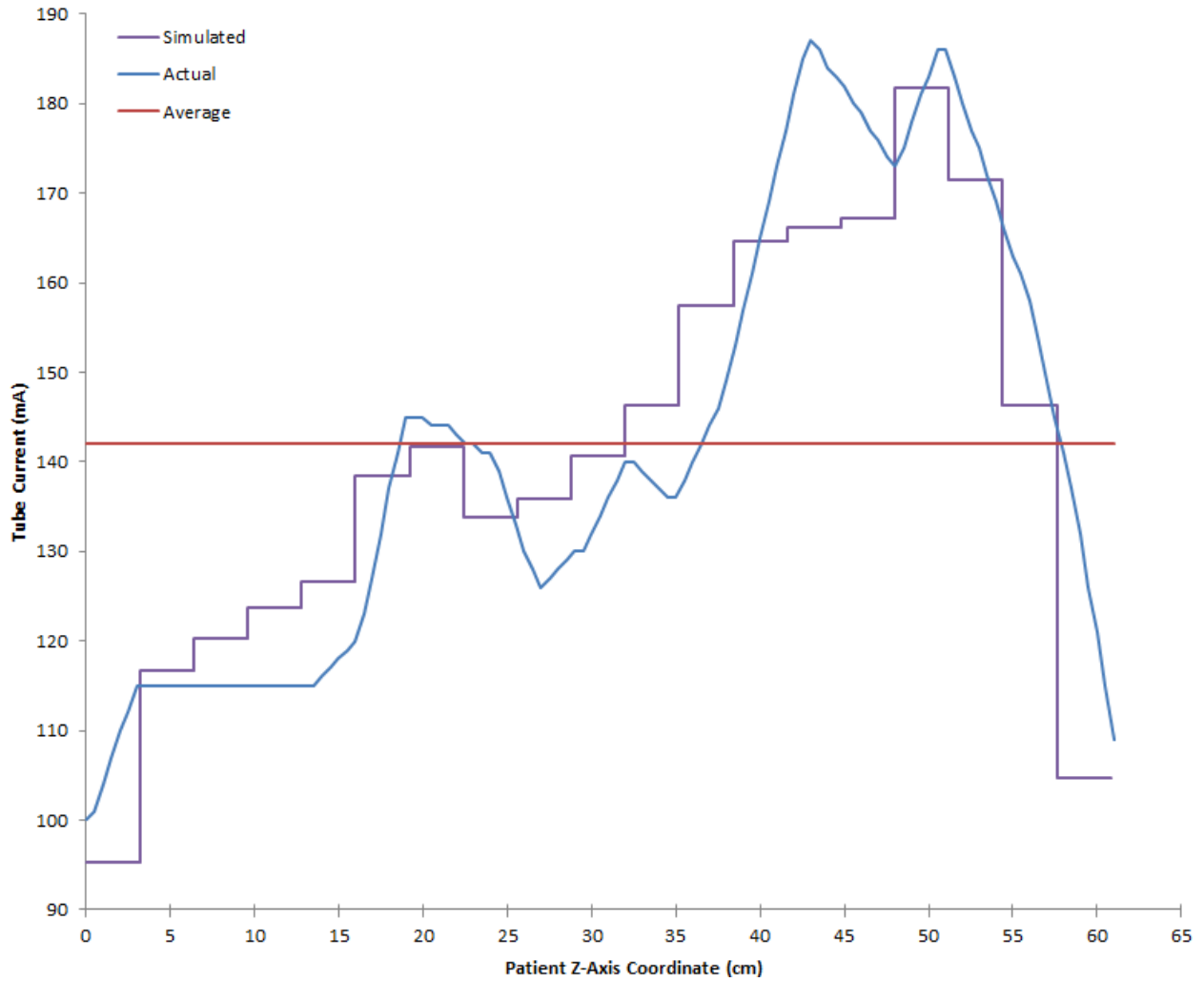


Figure 3-10. Small cadaver CAP exam tube current maps comparison.

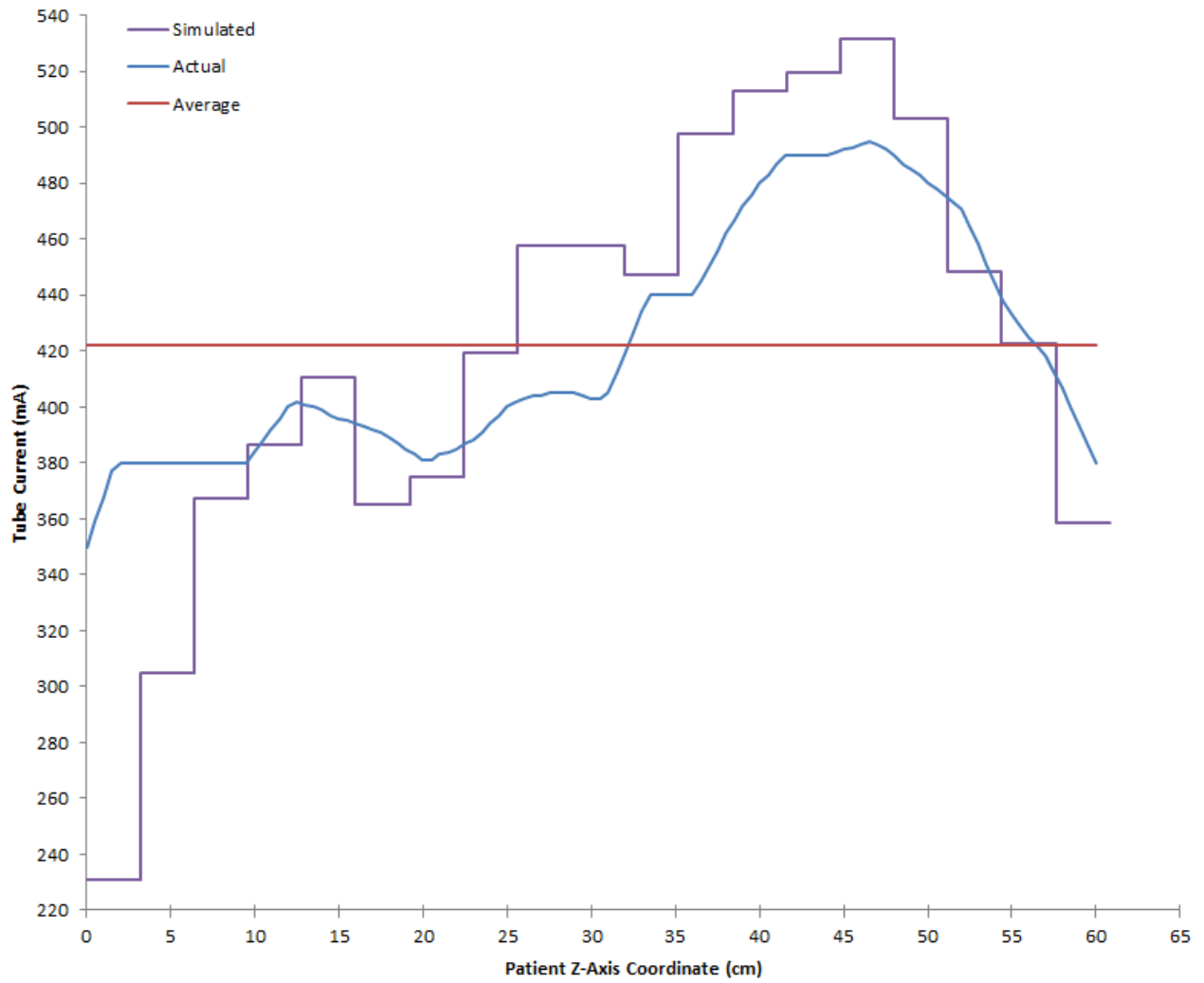


Figure 3-11. Medium cadaver CAP exam tube current maps comparison.

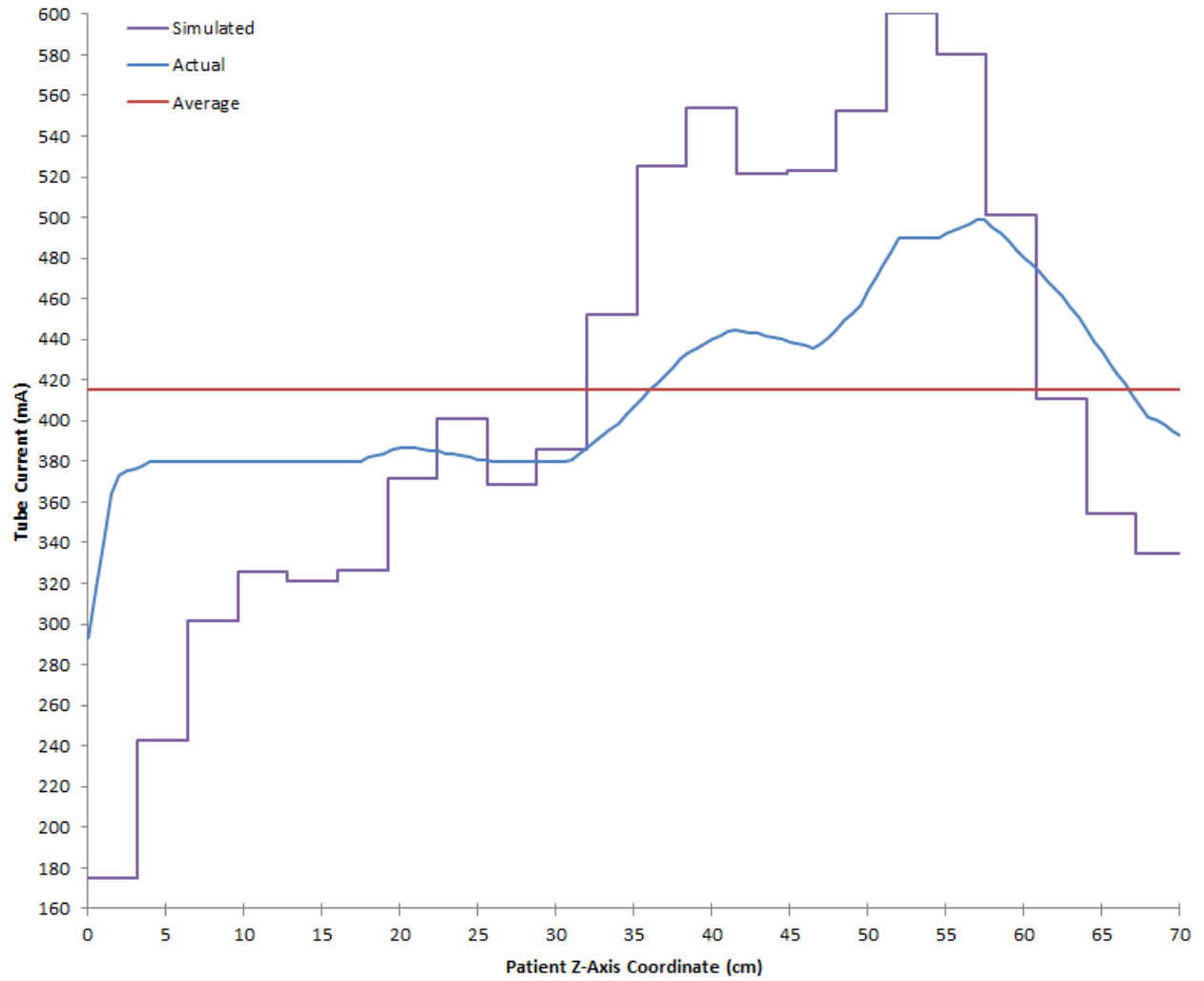


Figure 3-12. Large cadaver CAP exam tube current maps comparison.

Table 3-6. Small cadaver percent difference summary over all exams.

Dose Type		Fixed Tube Current	Image-Based Attenuation	Calculated Attenuation
Point Doses	Range	(-43.7, 52.6)	(-36.7, 48.0)	(-36.6, 51.2)
	Average Magnitude	18.0 ± 10.7	16.8 ± 10.6	17.9 ± 10.3
Point-Derived Organ Doses	Range	(-21.3, 24.9)	(-22.6, 27.4)	(-17.5, 50.7)
	Average Magnitude	11.2 ± 7.5	11.4 ± 6.3	11.0 ± 10.4
Volumetric Organ Doses	Range	(-29.8, 24.0)	(-19.2, 24.6)	(-22.4, 46.1)
	Average Magnitude	13.2 ± 10.2	12.1 ± 6.4	12.5 ± 11.0

Table 3-7. Medium cadaver percent difference summary over all exams.

Dose Type		Fixed Tube Current	Image-Based Attenuation	Calculated Attenuation
Point Doses	Range	(-48.0, 38.1)	(-44.2, 34.9)	(-34.5, 41.6)
	Average Magnitude	15.5 ± 10.2	11.3 ± 9.6	12.8 ± 10.8
Point-Derived Organ Doses	Range	(-25.3, 23.0)	(-23.0, 16.4)	(-28.2, 21.2)
	Average Magnitude	13.1 ± 6.7	7.5 ± 5.6	9.6 ± 9.1
Volumetric Organ Doses	Range	(-29.8, 36.5)	(-25.0, 27.0)	(-20.9, 22.0)
	Average Magnitude	12.8 ± 11.7	11.4 ± 8.2	11.2 ± 7.7

Table 3-8. Large cadaver percent difference summary over all exams.

Dose Type		Fixed Tube Current	Image-Based Attenuation	Calculated Attenuation
Point Doses	Range	(-45.3, 84.3)	(-44.8, 61.2)	(-39.3, 23.9)
	Average Magnitude	17.2 ± 14.2	15.2 ± 11.2	13.4 ± 8.7
Point-Derived Organ Doses	Range	(-28.9, 68.3)	(-26.2, 48.3)	(-22.4, 8.6)
	Average Magnitude	19.0 ± 14.7	14.3 ± 11.7	9.5 ± 6.2
Volumetric Organ Doses	Range	(-32.2, 22.0)	(-27.3, 12.1)	(-22.8, 8.7)
	Average Magnitude	15.6 ± 9.2	12.4 ± 8.5	10.2 ± 8.3

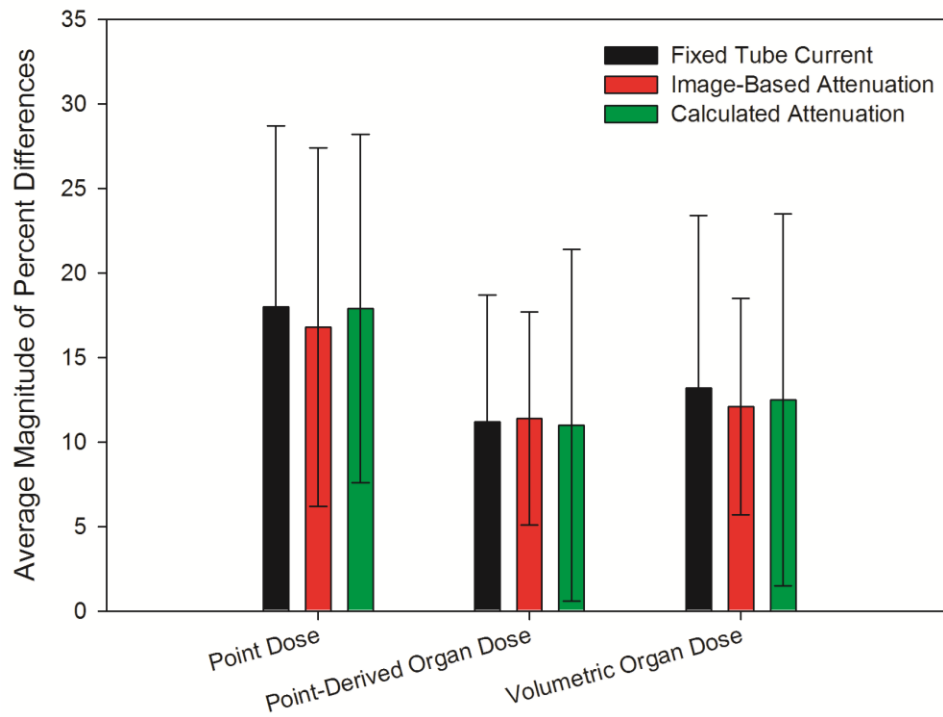


Figure 3-13. Small cadaver percent difference summary over all exams.

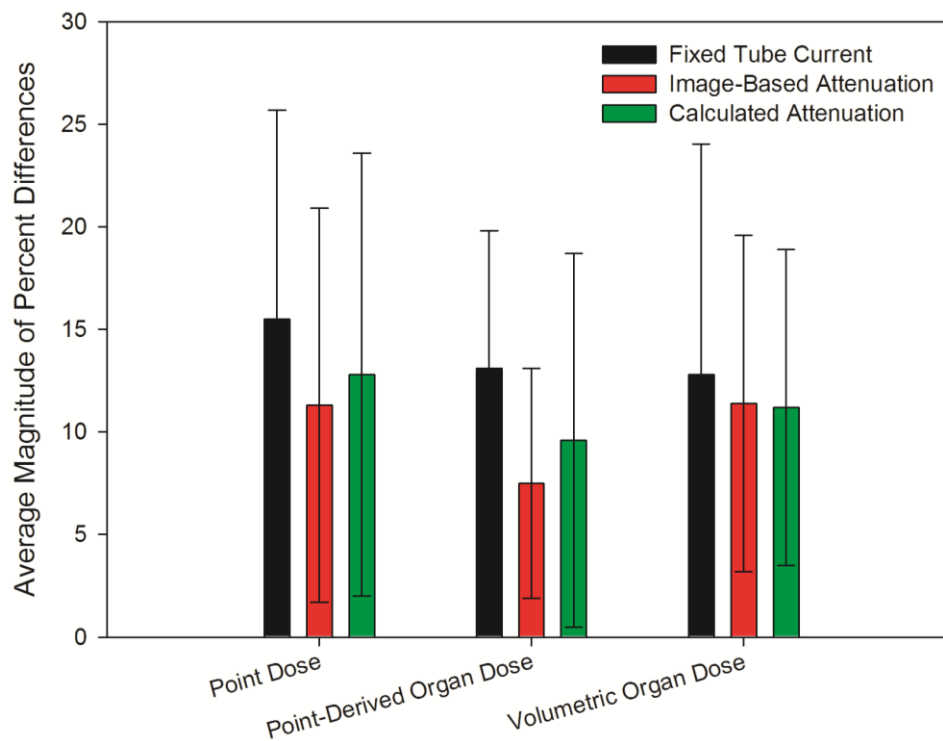


Figure 3-14. Medium cadaver percent difference summary over all exams.

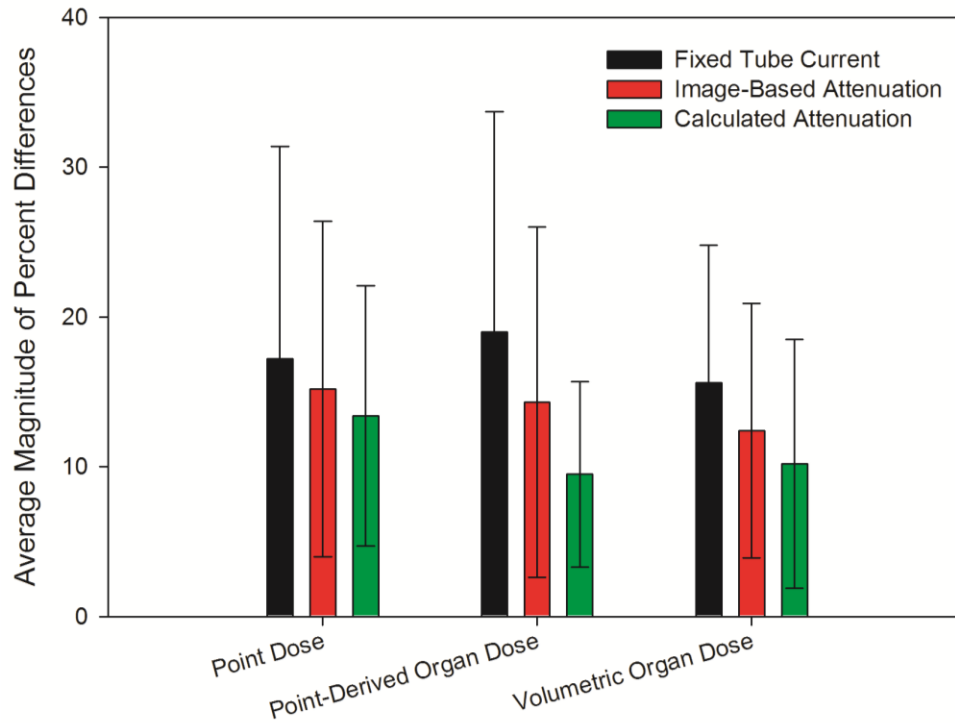


Figure 3-15. Large cadaver percent difference summary over all exams.

Table 3-9. Small cadaver percent difference summary over all exams for the calculated attenuation method using console average effective mAs.

	Point Doses	Organ Doses from Points	Volume Organ Doses
Range	(7.6, 174.0)	(37.3, 173.0)	(7.6, 164.7)
Average Magnitude	74.0 ± 37.3	77.0 ± 30.0	79.8 ± 31.7

CHAPTER 4
IMPACTS OF ANTHROPOMORPHIC PATIENT-PHANTOM MATCHING ON ORGAN
DOSE IN CT EXAMS WITH AND WITHOUT ATCM

Using Computational Phantoms for Patient CT Dosimetry

Any time Monte Carlo CT patient dosimetry is to be performed, a computational anthropomorphic phantom must be used for radiation transport. There are many types of phantoms that have been developed and described in the literature, each with their own strengths and weaknesses. These phantoms have varying degrees of anatomical accuracy, ease-of-use, and scaling flexibility, all of which impact the accuracy of dosimetric evaluation.

Classifications of Computational Phantoms

These phantoms can be classified into three broad types. Stylized (or mathematical) phantoms are characterized by three-dimensional geometric surface equations that when put together approximate internal anatomy and body contour. These phantoms can be altered (e.g. organ repositioning and size scaling) with relative ease, but their anatomy is simplistic and often unrealistic as compared to that seen in real patients. Voxel (i.e. voxel element) phantoms are created from segmenting the body and organ contours from CT or magnetic resonance (MR) image sets, and offer high anatomical accuracy. However, the ability to rescale these phantoms to fit a broader range of patient sizes is severely limited by the fixed voxel lattice structure. Voxel phantoms may be rescaled uniformly in 2D or 3D, but non-uniform reshaping of the body contour or organ surfaces within a voxel phantom is extremely difficult and prone to error. Hybrid phantoms combine the flexibility of stylized phantoms and the anatomical realism and accuracy of voxel phantoms. Hybrid phantoms were developed

and used for the first time for medical patient dosimetry at the University of Florida, and employ non-uniform rational B-spline (NURBS) and polygon mesh surfaces that permit the modeling of models and body contours with high anatomical realism while allowing for the uniform scaling and reshaping of these surfaces through NURBS control point manipulation.

For each phantom classification, there are four morphometric categories: reference, patient-dependent, patient-sculpted, and patient-specific. Reference phantoms use 50th-percentile values for anthropomorphic parameters such as height, weight, and organ mass to represent average individuals in a patient population, and are often made for different reference ages. They are generally associated with data published by the ICRP, and thus these average values are taken from data pooled across many different countries. Consequently, an ICRP reference phantom might very well not represent the 50th percentile individual in a given country (perhaps under-sized for US morphometries). Furthermore, these phantoms lack anatomical specificity for individuals who can easily diverge from 50th-percentile parameter values. Patient-dependent phantoms relax these 50th-percentile design criteria, and are usually available in “libraries” that contain a wide range of phantoms encompassing different ages, weights, and heights apart from the reference values. The strong utility of these phantoms libraries is that they allow for the matching of a patient to a patient-dependent phantom that more closely shares the same morphometric characteristics of that patient than would be afforded by a limited series of reference phantoms. Patient-dependent libraries also allow for the creation of precalculated organ dose databases that can be used for rapid dosimetry reporting over a large population of patients without the need

to explicitly run Monte Carlo radiation transport on a per-patient basis. The third morphometric category of phantoms - patient-sculpted phantoms - are patient-dependent phantoms that have adjusted body surface control points to uniquely and exactly match those of a given patient. While adding another degree of anatomical matching, these phantoms are made uniquely for the patients in question, and thus no prior organ dosimetry library could be created. It is noted that for both patient-dependent and patient-sculpted phantoms, no specific adjustments to internal organ anatomy are made other than uniform 2D or 3D scaling of body regions (e.g., torso height, leg lengths, etc.) as they offer only an exterior body shape matching of the targeted patient. The final category, patient-specific phantoms, provide the most accurate match of patient anatomy. They are created by segmenting whole-body CT scans to uniquely model a patient's exterior as well as internal organ morphometry. Alternatively, a patient-specific phantom may be assembled from a patient sculpted phantom through additional matching of internal organ shape, depth, and position as seen of these patient CT images. The requisite segmenting of the patient's CT images is a labor-intensive process and whole-body scans are often not available for patients, so the practicality of using these phantoms for large-scale patient dosimetry is very low.

UF/NCI Family of Hybrid Computational Phantoms

For the purposes of assembling a precalculated CT organ dosimetry library and executable code, a hybrid patient-dependent phantom library offers the most practical means of combining fast, reliable organ dosimetry with enhanced accuracy. Recently, a new hybrid phantom library was created by Amy Geyer for her Master's thesis research, in a collaborative effort between the University of Florida and the National Cancer

Institute (NCI).⁵⁰ This work represented a continuation of work by Johnson *et al.*,⁵¹ where UF hybrid adult reference phantoms were shaped into patient-dependent phantoms matching anthropometric parameters statistically derived from the Centers for Disease Control and protection (CDC) National Health and Nutrition Examination Survey (NHANES) III, a survey of anthropometric data from patients in the United States over the years of 1988-1994. Ms. Geyer, using the newest set of CDC NHANES data (collected from 1999-2006), created four “grids” of patient-dependent phantoms representing adult males (100 phantoms), adult females (93 phantoms), pediatric males (75 phantoms), and pediatric females (73 phantoms). Each grid of phantoms has a height (5 cm increments for adults, 10 cm for pediatrics) and weight (5 kg increments) axis that helps identify the availability of phantoms possessing those parameters. Additionally, the grids indicate the CDC body mass index (BMI) classification for each phantom (underweight, healthy, overweight, obese, or morbidly obese). The BMI is calculated as a ratio of the patient's weight (in kilograms) to the square of their standing height (in meters). For adults, underweight individuals have a BMI below 18.5, healthy individuals have a BMI within 18.5-24.9, overweight individuals between 25.0-29.9, obese individuals between 29.9-39.9, and morbidly obese individuals 40.0 and above. For children and adolescents, the BMI category is determined from BMI-for-age charts provided by the CDC. Figures 4-1 and 4-2 show the adult male and adult female grids, respectively.

The scaling process for each phantom contained several steps. First, target anthropometric parameter values were derived from the NHANES data for the targeted phantom height and weight combinations, including sitting height, waist circumference,

arm circumference, thigh circumference, and buttocks circumference. Next, an “anchor phantom” was selected from the UF family of reference hybrid phantoms to be used for scaling. This phantom was then three-dimensionally scaled to match the target sitting height of the phantom of interest, with the legs scaled in the z-direction to match target standing height. The remaining secondary circumferential parameters were then matched to within 1% of targeted values, and the total weight matched to within 1 kg of the target value. The result of this work was a large-scale family of patient-dependent hybrid phantoms that cover a wide range of ages, heights, and weights that are grounded in robust statistical data that can be used for large-scale dosimetry studies.

Determining Patient-Phantom Matching Dose Uncertainties

As mentioned previously, patient-specific voxel phantoms provide the highest degree of anatomical accuracy in terms of assessing organ dose to an individual patient. However, since creating and using these phantoms in a practical clinical setting for patient dose assessment is infeasible, patients must be matched to pre-constructed phantom types. As good scientific practice, the dose uncertainties of this patient-phantom matching should be quantified when possible in providing large-scale patient dosimetry. This study aims to investigate these patient-phantom matching effects in CT dosimetry for exams with and without ATCM using the UF/NCI family of patient-dependent hybrid phantoms, the UF reference adult hybrid phantoms,⁵² and an ORNL reference adult stylized phantom.⁵³

Phantom CT Dosimetry Comparison Study Methodology

Patient-Specific Phantom Creation

In a previous patient-phantom matching study by Johnson *et al.*,⁵⁴ 27 adult CT CAP datasets (14 male and 13 female) of broad height and weight ranges were selected and retrieved from the image archives at Shands Jacksonville Medical Center. These image sets were then contoured and converted to MCNPX-readable patient-specific voxel phantoms using the same methodology presented in Chapter 3 for the cadaver phantoms. Eight anatomical organs or structures were contoured and included in each phantom: lungs, pericardium, urinary bladder, stomach, pancreas, liver, spleen, and kidneys. These patient-specific phantoms would serve to provide dose benchmarks for the comparison study as the “actual” organ doses received by the patients themselves, an assumption that has been shown in the literature to be valid.²⁸

Patient-Dependent Phantom Matching

Each patient was then matched to a patient-dependent phantom in the UF/NCI library by matching criteria involving height, weight and BMI. The nearest two height and weight increments on the grid (ideally one above and one below the patient’s parameters) to those of a patient were found, and the phantoms available within these bound were selected and had their BMI values calculated. The phantom with the BMI nearest that of the patient from that group was chosen as the patient’s match. For outlier patients with unusually large or small BMI values, the nearest three height and weight increments were used to try to find the best BMI match. Table 4-1 contains morphometric data for the male patients and their matched patient-dependent phantoms. Table 4-2 contains the same data for the female patients, while Table 4-3

contains data for the three reference phantoms of interest in this comparison: the UF reference adult male hybrid, the UF reference adult female hybrid, and an ORNL reference adult hermaphrodite. Figures 4-3 and 4-4 contain side-by-side frontal and left lateral views, respectively, of the patient-specific and matched patient-dependent phantoms for male patient 9, as well as the UF reference adult male hybrid and ORNL reference adult stylized phantoms.

CT Exam Dosimetry

Two sets of CT exams (CAP, chest, abdomen, and pelvis) were simulated on all phantoms in this study: one set with fixed tube current, and the other incorporating ATCM. The slice-by-slice dosimetry performed on these phantoms was identical to the cadaver phantom dosimetry methods described in detail in Chapter 3. The parameters for all exams were held identical at 120 kVp, large bowtie filter, large focal spot, 64 x 0.5 mm beam collimation, and an average effective mAs of 100. The ATCM dose calculations were performed using the quarter circular arc kerma detector methodology to calculate attenuation, as this was proven the best calculation method in the cadaver study. F6 dose deposition tallies were calculated for the eight organs segmented in the patient-specific phantoms (lungs, pericardium, urinary bladder, stomach, pancreas, liver, spleen, and kidneys) for all phantoms. As with the cadaver studies, 100 million particles were transported for the dosimetry simulations, while 10 million were transported for the attenuation calculations (for a total of 18,720 total simulations run). After all simulations were completed, a custom MATLAB™ script was used to post-process the data.

Results and Discussion

Due to the large amount of data generated as part of this study, only the summary tables for the results will be presented in this chapter. The full set of data tables can be found in Appendix B. For all studies, the percent differences between patient-specific phantom organ doses and matched-phantom organ doses were defined by the following equation:

$$\text{Percent Difference} = \frac{\text{Match Phantom Organ Dose} - \text{Patient Specific Organ Dose}}{\text{Patient Specific Organ Dose}} * 100 \quad (4-1)$$

For the purposes of allowing for analysis of percent difference trends as a function of BMI, the patients were split into three categories. The “Healthy” category contained patients with BMI values that placed them in the underweight or healthy CDC category. The “Overweight” category contained patients with BMI values that placed them in the overweight CDC category. The “Obese” category contained patients with BMI values that placed them in the obese or morbidly obese CDC category.

It should also be noted that for the purposes of this analysis, only the results from those organs deemed “in-field” (at least approximately 50% of the organ volume within the primary beam) for each exam type were considered. This is due to the fact that in-field doses can reach values more than an order of magnitude higher than those out-of-field in CT exams, and are therefore of much more importance and consequence. Assessing the effect of patient-phantom matching on the ability of a dosimetry methodology to accurately calculate patient in-field doses was seen as a more meaningful study than incorporating out-of-field contributions. The in-field organs for each exam were: all eight organs for CAP exams; lungs, pericardium, stomach, liver,

and spleen for chest exams; stomach, pancreas, liver, spleen, and kidneys for abdomen exams; and bladder for pelvis exams.

Fixed Tube Current Exams

The overall percent difference average magnitude results for the three matched phantoms for the fixed tube current exams can be seen in Table 4-4. These average magnitudes incorporated all in-field organs for all exam types. The justification for this combination was the fact that there was no noticeable dependence on organ or exam type in the behavior of the percent dose; rather, the behavior had strong dependence on patient BMI category and the type of matched phantom.

For the virtual male patients, the overall results show that the patient-dependent phantoms provide lower dose percent differences as compared to the two reference phantoms: there was an average decrease in percent difference of about 6% as compared to the reference hybrid and 10% for the reference stylized. However, in the overweight male group, the reference hybrid phantom had an average decrease of 0.3% as compared to the patient-dependent hybrid phantoms; and in the healthy male group, the two were equal at 19.8%. For the obese male group, however, the patient-dependent phantoms had percent differences a factor of 2 lower than the reference hybrid and a factor of 3 lower than the reference stylized phantoms. This is most likely caused by the fact that the patient-dependent phantoms better model the additional tissue shielding in the form of subcutaneous fat present in these patients of higher BMI. For all groups, the reference stylized had the largest percent difference results, which was expected due to their more unrealistic organ anatomy. Within the patient-

dependent results, the smallest percent difference results came for the overweight group, followed by the obese group, then the healthy group.

For the females, the overall results show that the patient-dependent phantoms have the least average percent differences; about 21% less than the reference hybrid and 19% less than the reference stylized phantoms. In each individual group, the patient-dependent phantoms had the lowest percent differences as well. The obese group in particular had a percent difference around 57% less than for the reference hybrid, and 38% less than for the reference stylized. For the females, the reference stylized had lower percent differences than the reference hybrid results for the overweight and obese BMI categories. This may be due to the fact that the reference stylized phantom has a larger BMI than the reference hybrid, and can therefore more accurately match doses with the larger patient-specific phantoms. However, this same trend was not seen for the male patient-specific phantoms, so this may not be the underlying reason for better results. Within the patient-dependent results, the smallest percent difference results came for the healthy group, followed by the overweight group, then the obese group.

Combining the results for both genders reveals that the patient-dependent phantoms have overall smaller percent differences than the two reference phantoms, especially within the obese group. Overall, there seems to be around a 16% average magnitude of percent difference as compared to the patient-specific phantom data, indicating a 16% dose uncertainty when using these phantoms to estimate patient dose. However, this uncertainty is about half that of the two reference phantoms, which are currently what are being used in large-scale CT dosimetry tools today.

ATCM Exams

The overall percent difference average magnitude results for the three matched phantoms for the exams with ATCM can be seen in Table 4-5. These average magnitudes incorporated all in-field organs for all exam types. Like the fixed tube current exams, there was no noticeable dependence on organ or exam type in the behavior of the percent dose; rather, the behavior had strong dependence on patient BMI category and the type of matched phantom.

For the virtual male patients, the overall results show that the patient-dependent phantoms provide smaller average dose percent differences as compared to the two reference phantoms: about 6% less as compared to the reference hybrid and 12% less for the reference stylized. However, in the overweight male group, the reference hybrid phantom had average percent differences 1.2% less than the patient-dependent hybrid phantoms. For the obese male group, however, the patient-dependent phantoms had percent differences about three times smaller than the reference hybrid and reference stylized phantoms. This is again most likely caused by the fact that the patient-dependent phantoms better model the extra shielding in the form of adipose tissue that these patients of higher BMI have, which is even more apparent in CT imaging exams acquired under ATCM. For all groups, the reference stylized once again had the largest percent difference results. Within the patient-dependent results, the smallest percent differences came for the overweight group, followed by the obese group, then the healthy group.

For the virtual female patients, the overall results show the patient-dependent phantoms had about 30% smaller percent differences compared to the reference hybrid

and 27% compared to the reference stylized phantoms. For all categories, the patient-dependents had lower percent differences, especially in the obese group. In this group the percent difference was around 82% less than for the reference hybrid, and 63% less than for the reference stylized. Once again, the reference stylized had smaller percent difference results compared to the reference hybrid results for the overweight and obese BMI categories. Within the patient-dependent results, the smallest percent differences came for the healthy group, followed by the overweight group, then the obese group.

Combining the results for both genders reveals that the patient-dependent phantoms once again have smaller percent differences than the two reference phantoms, most notably in the obese group. Overall, there seems to be around an 11% average magnitude of percent difference as compared to the patient-specific phantom data, indicating a 11% dose uncertainty when matching these phantoms to patients for organ dose estimation for CT exams with ATCM. However, this uncertainty is a third of that of the two reference phantoms. This more dramatic decrease in uncertainty as compared to the fixed tube current exams comes from the fact that the patient-dependent morphometry plays an even more important role due to the presence of the ATCM in the exam.

Conclusion

The overall conclusion that can be drawn from this study is that for CT exams both with and without ATCM, use of patient-dependent phantoms from the UF/NCI family of hybrid computational phantoms will provide two to three times less uncertainty for in-field organ dose estimates as compared to the reference hybrid and stylized

phantoms that are currently being employed in CT dosimetry studies. No patient-phantom matching is perfect, as seen in the average percent difference magnitudes of 16% for fixed tube current exams and 11% for exams with ATCM. However, there is no way to perfectly match both individual body morphometry and internal organ anatomy variations (size, shape, and position) outside of patient-specific phantoms, which, are not practical for use in a clinical environment in which patient CT dosimetry must be performed. Patient matching using this patient-dependent phantom library provides the practicality necessary for CT dosimetry in a clinical environment, while keeping the dose uncertainty as low as possible.

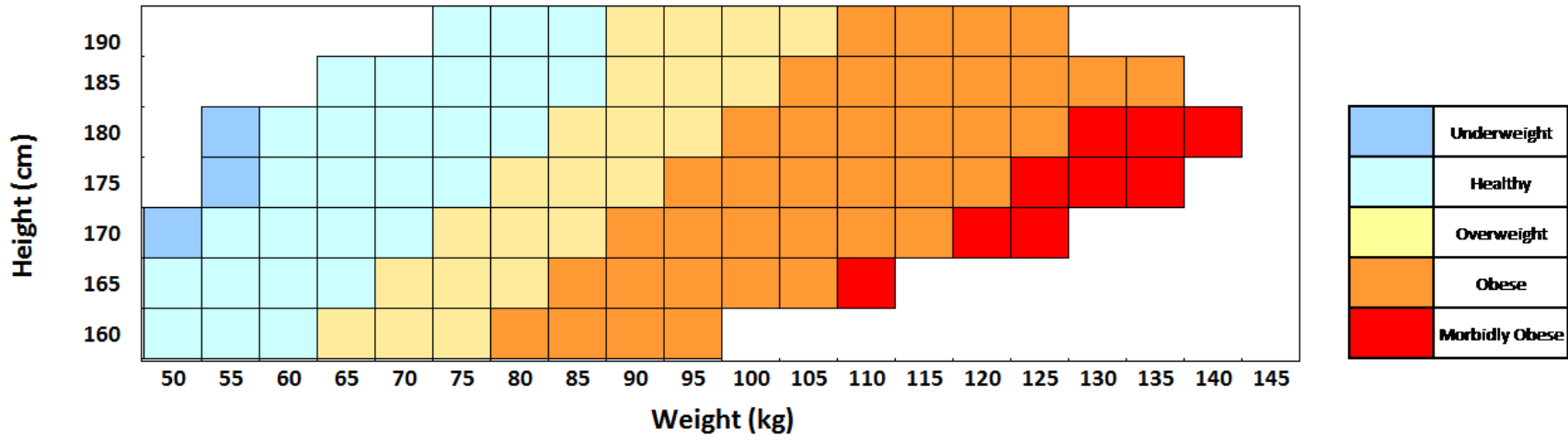


Figure 4-1. Adult male phantom grid for the UF/NCI family of computational hybrid phantoms.

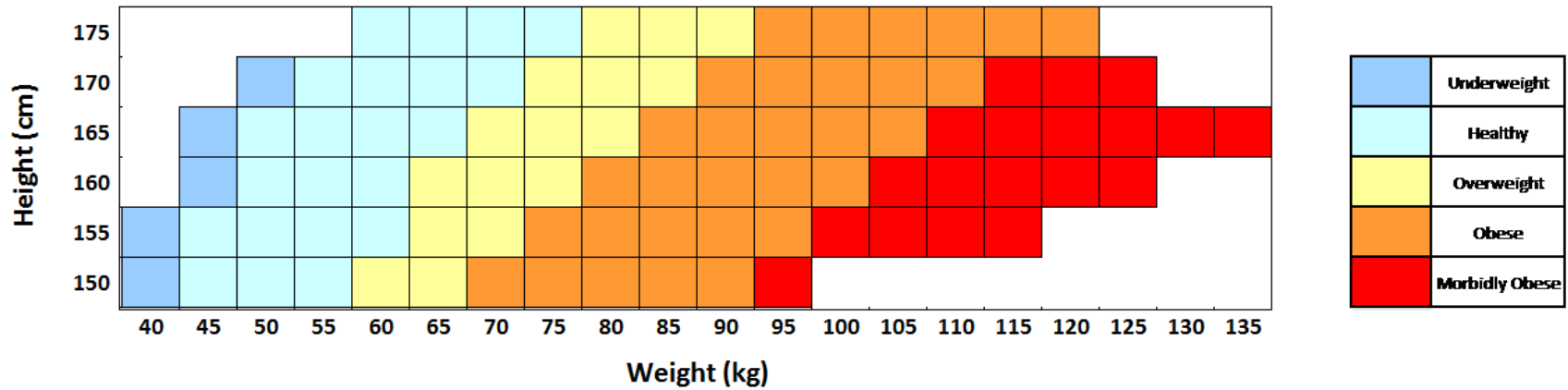


Figure 4-2. Adult female phantom grid for the UF/NCI family of computational hybrid phantoms.

Table 4-1. Adult male patient and matched patient-dependent morphometry data.

Phantom	Patient-Specific				Matched Patient-Dependent			
	Height (cm)	Mass (kg)	BMI	Classification	Height (cm)	Mass (kg)	BMI	Classification
1	157.5	43.5	17.6	Underweight	160	50	19.5	Healthy
2	165.1	74.4	27.3	Overweight	165	75	27.5	Overweight
3	167.6	78.5	27.9	Overweight	170	80	27.7	Overweight
4	172.7	74.4	24.9	Healthy	175	75	24.5	Healthy
5	172.7	98.0	32.8	Obese	175	100	32.7	Obese
6	175.3	66.2	21.6	Healthy	175	65	21.2	Healthy
7	175.3	80.7	26.3	Overweight	175	80	26.1	Overweight
8	177.8	73.5	23.2	Healthy	180	75	23.1	Healthy
9	177.8	99.8	31.6	Obese	180	100	30.9	Obese
10	180.3	81.6	25.1	Overweight	180	80	24.7	Healthy
11	182.9	85.7	25.6	Overweight	185	90	26.3	Overweight
12	182.9	112.5	33.6	Obese	185	115	33.6	Obese
13	182.9	74.4	22.2	Healthy	185	75	21.9	Healthy
14	193.0	131.5	35.3	Obese	190	125	34.6	Obese

Table 4-2. Adult female patient and matched patient-dependent morphometry data.

Phantom	Patient-Specific				Matched Patient-Dependent			
	Height (cm)	Mass (kg)	BMI	Classification	Height (cm)	Mass (kg)	BMI	Classification
1	152.4	66.2	28.5	Overweight	150	65	28.9	Overweight
2	154.9	47.6	19.8	Healthy	155	50	20.8	Healthy
3	154.9	69.9	29.1	Overweight	155	70	29.1	Overweight
4	154.9	98.0	40.8	Morbidly Obese	155	100	41.6	Morbidly Obese
5	160.0	51.3	20.0	Healthy	160	50	19.5	Healthy
6	160.0	51.7	20.2	Healthy	160	50	19.5	Healthy
7	160.0	60.8	23.7	Healthy	160	60	23.4	Healthy
8	163.8	59.0	22.0	Healthy	165	60	22	Healthy
9	162.6	80.3	30.4	Obese	165	80	29.4	Overweight
10	162.6	117.5	44.5	Morbidly Obese	165	120	44.1	Morbidly Obese
11	165.1	62.6	23.0	Healthy	165	65	23.9	Healthy
12	172.7	82.1	27.5	Overweight	170	80	27.7	Overweight
13	175.3	135.6	44.2	Morbidly Obese	170	125	43.3	Morbidly Obese

Table 4-3. Adult reference phantom morphometry data.

Phantom	Height (cm)	Mass (kg)	BMI	Classification
UF Reference Hybrid Adult Male	176	67	21.6	Healthy
UF Reference Hybrid Adult Female	163	59	22.2	Healthy
ORNL Reference Stylized Adult Hermaphrodite	170	75	26	Overweight

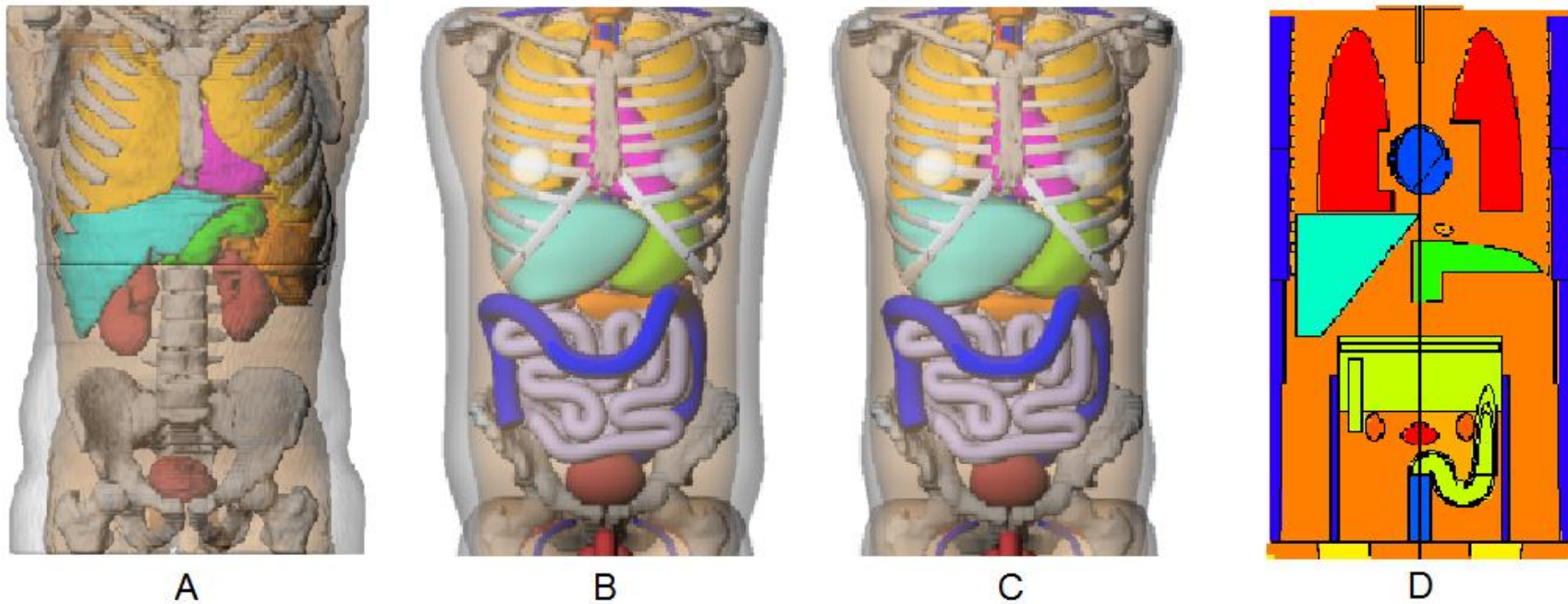


Figure 4-3. Frontal view of the four phantoms used for dosimetry for male patient nine. A) Patient-specific. B) Matched patient-dependent. C) Reference hybrid. D) Reference stylized.

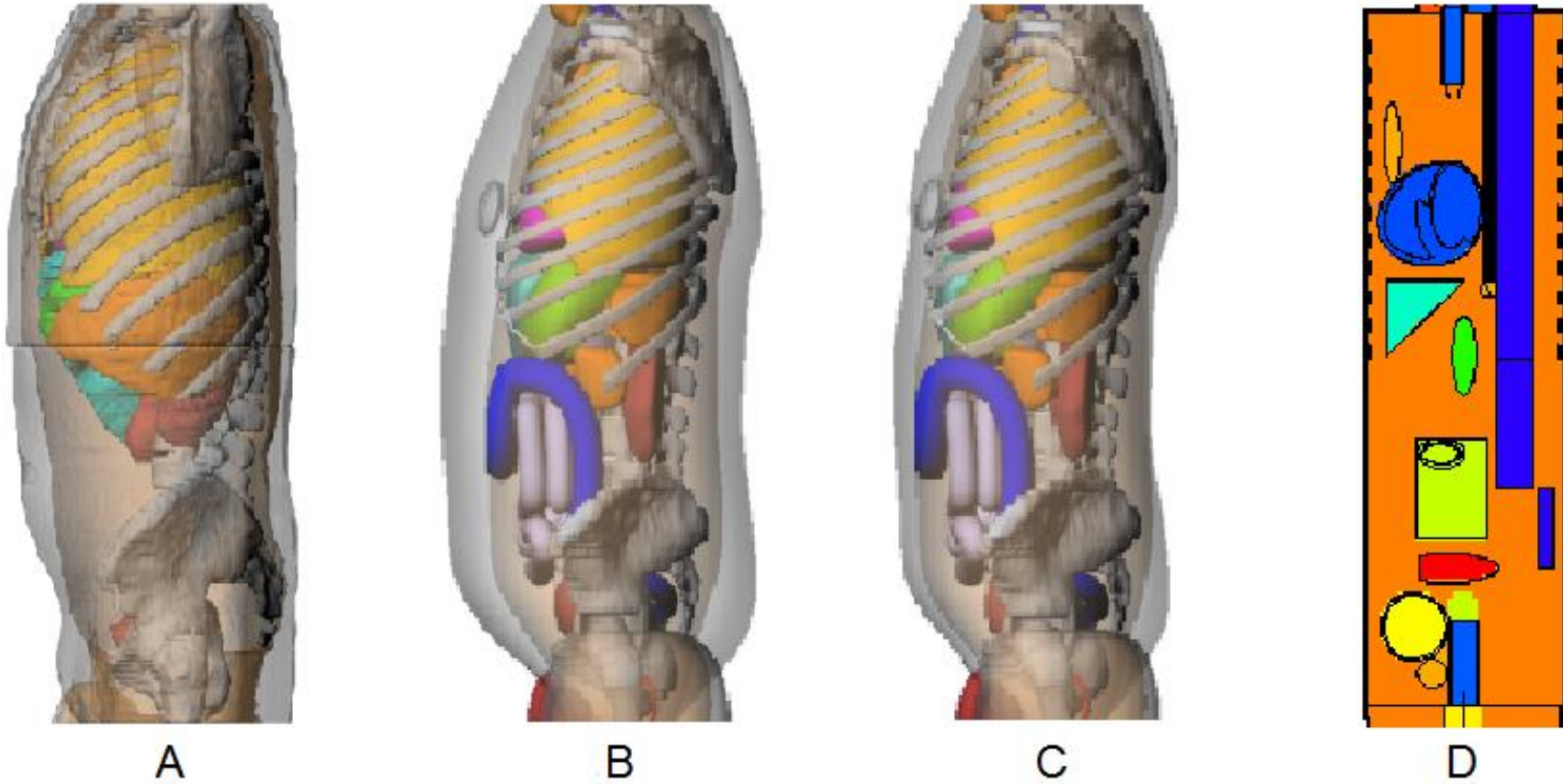


Figure 4-4. Left lateral view of the four phantoms used for dosimetry for male patient nine. A) Patient-specific. B) Matched patient-dependent. C) Reference hybrid. D) Reference stylized.

Table 4-4. Overall percent difference average magnitude results for in-field organs for all fixed tube current CT exams.

Gender	Category	Patient-Dependent	Reference Hybrid	Reference Stylized
Male	Healthy	19.8	19.8	22.5
	Overweight	10.3	10.0	14.1
	Obese	15.4	36.9	42.0
	All	15.1	21.2	25.0
Female	Healthy	9.7	13.3	23.8
	Overweight	13.2	17.7	15.4
	Obese	28.7	85.9	66.6
	All	16.3	37.0	35.3
Combined	Healthy	14.3	16.2	23.2
	Overweight	11.3	12.9	14.6
	Obese	22.0	61.4	54.3
	All	15.7	28.8	30.0

Table 4-5. Overall percent difference average magnitude results for in-field organs for CT exams with ATCM.

Gender	Category	Patient-Dependent	Reference Hybrid	Reference Stylized
Male	Healthy	16.9	20.2	24.7
	Overweight	8.3	7.1	14.4
	Obese	12.1	31.3	37.8
	All	12.5	18.7	24.8
Female	Healthy	6.0	10.3	19.9
	Overweight	9.8	22.4	15.4
	Obese	14.0	96.1	77.3
	All	9.4	39.5	36.5
Combined	Healthy	11.0	14.8	22.1
	Overweight	8.8	12.8	14.8
	Obese	13.0	63.7	57.5
	All	11.0	28.7	30.4

CHAPTER 5 FINAL CONCLUSIONS AND FUTURE WORK

Results and Conclusions of This Work

The overall goal of this work was to investigate the initial feasibility and accuracy of using a pre-calculated organ dose database for CT dosimetry as has been proposed for new software programs in development within the ALRADS laboratory at UF. This software will provide organ dose estimates for patients undergoing CT imaging exams with ATCM on Toshiba 64-slice scanners. If successfully validated, this software would provide much-needed improvements to currently-available CT dosimetry tools, to include the use of a hybrid phantom library covering a large span of patient ages, heights, and weights for dosimetry calculations, while at the same time accounting prospectively for the influences of ATCM on patient organ dose estimates.

The final results of this work indicate that the proposed dosimetric methodology for this new software is indeed feasible for patient dosimetry on a Toshiba scanner operating in 64-slice mode with and without ATCM. For the CAP exam without ATCM, the average percent differences of simulated cadaver organ doses compared to experimentally-measured doses were all below 15%. For the four body exams with ATCM over the three cadavers, average percent differences were all below 13% for the volumetric organ dose methodology that is to be employed by the software. The effects of matching a patient to a patient-dependent phantom from the UF/NCI family of computational hybrid phantoms were found to be an average 16% percent difference for fixed tube current exams and 11% for exams with ATCM. These numbers are acceptable given the fact that those phantoms currently employed in CT software today

resulted in dose uncertainties two to three times greater than that of the patient-dependent phantoms.

Although further work must be performed to improve and validate the methodology presented in this study, this initial proof-of-concept can be confirmed as a feasible method of calculating patient organ doses for CT exams with ATCM in a fast and easy-to-implement manner.

Proposed Future Work

MCNPX Source Subroutine

Additional work should be undertaken in order to further characterize and improve the current MCNPX source subroutine of the Toshiba Aquilion ONE CT scanner. For this study, only the effects of the large focal spot were fully characterized, so work should be done to investigate the dosimetric impacts (if any) of the small focal spot selection during exams, and how to incorporate this into the source model. Additional work must also be done to investigate the accuracy of the subroutine for smaller patients, as the head CTDI phantom validation was not on par with that of the body CTDI phantom.

ATCM Dosimetry Algorithm

The accuracy of the attenuation-calculation dosimetry algorithm presented in this paper must be further tested with a more robust set of organ dose measurements using UF anthropomorphic phantoms. These phantoms allow for dose measurements for 15+ internal organs, and would provide more insight and guidance into how to improve the algorithm's accuracy and reproducibility, especially since the material composition is much better known and more uniformly present in the organ anatomy than that found in the cadavers. Since this initial iteration of the algorithm did not take into account tube

current minimum and maximum limits as can be specified in SureExposure™ 3D, it would be beneficial to investigate the impacts of those specified ranges on the algorithm and associated dosimetry. Additionally, CT head exam dose measurements should also be made and tested, as those data were not considered in this initial feasibility study. The effects of exam overranging (or helical overscan) should be investigated in order to determine its impact on dosimetric accuracy and how best to incorporate it into the final CT dosimetry software. Additionally, finding potential correlations to other post-exam metrics shown by the console such as the volume weighted CT dose index (CTDI_{vol}) or dose length product (DLP) to an acceptable exam average effective mAs should be investigated.

Patient-Phantom Matching

Just as the patient-phantom matching study quantified the uncertainties for adult patients, a new study should be undertaken to evaluate this matching's effect on pediatric patients while incorporating typical pediatric-specific CT scan parameters. Additionally, further investigation should be made into the patient-phantom matching method, such as including body circumference values as a part of the matching criteria

Final Thoughts

The research presented in this dissertation provides the foundations for a new CT dosimetry software program that could provide significant improvements in patient dose estimation over current CT dosimetry tools such as ImPACT's CTDosimetry and CT-Expo, while still maintaining the speed and practicality these programs provide. Such software could come in two iterations: one web-based and available for free CT dose calculations for a variety of applications including radiation epidemiology studies, and the other integrated into the PACS of a clinical radiology practice. With a current

push to provide patient organ dose information in medical records (such as in California), a program such as this could provide hospitals and imaging clinics a clinically-viable solution to accomplish this without a large strain in workflow. It is hoped that the methodology presented in this study will be improved upon to the point that such implementation can be achieved.

APPENDIX A
CADAVER ATCM DOSE STUDY DATA TABLES

Large Cadaver Fixed Tube Current CAP Exam Data Tables

Point Dose Comparison

Dose Point	CAP Doses (mGy)		Percent Difference
	Simulated	Measured	
Lung - 1	23.2	20.3	14.5
Lung - 2	22.7	25.6	-11.1
Lung - 3	20.0	18.7	7.2
Lung - 4	20.0	21.4	-6.8
Lung - 5	30.5	32.0	-4.5
Lung - 6	31.7	32.0	-1.0
Lung - 7	28.0	25.9	8.0
Lung - 8	26.6	30.0	-11.3
Breast - 1	24.2	28.8	-15.8
Breast - 2	22.8	28.9	-21.0
Breast - 3	24.6	33.4	-26.2
Breast - 4	28.1	30.8	-8.8
Breast - 5	22.7	30.0	-24.5
Breast - 6	19.2	21.2	-9.6
Breast - 7	16.3	22.9	-28.8
Breast - 8	20.8	21.8	-4.6
Breast - 9	20.7	19.8	4.9
Breast - 10	19.6	20.9	-6.4
Liver - 1	27.3	26.0	5.1
Liver - 2	27.7	28.1	-1.4
Liver - 3	27.5	30.2	-8.9
Liver - 4	24.3	26.0	-6.6
Liver - 5	25.0	25.5	-1.7
Stomach - 1	20.1	25.4	-20.7
Stomach - 2	21.7	27.1	-20.0
Small Intestine -1	24.4	30.0	-18.6
Small Intestine -2	25.8	30.1	-14.1
Colon - 1	20.7	27.6	-25.2
Colon - 2	16.4	20.7	-20.9
Uterus	17.5	20.2	-13.6
Ovary - 1	19.0	22.9	-17.3
Ovary - 2	19.8	20.6	-3.5
Thyroid - 1	44.9	35.7	25.7
Thyroid - 2	42.2	34.6	22.1
Average Magnitude:			13.0
Standard Deviation:			8.2
Minimum:			-28.8
Maximum:			25.7

Point-Dose-Derived Average Organ Dose Comparison

Organ	CAP Doses (mGy)		Percent Difference
	Simulated	Measured	
Lung	25.3	25.7	-1.4
Breast	21.9	25.8	-15.1
Liver	26.4	27.2	-3.0
Stomach	20.9	26.2	-20.2
Small Intestine	25.1	30.1	-16.5
Colon	18.5	24.2	-23.5
Uterus	17.5	20.2	-13.4
Ovary	19.4	21.8	-11.0
Thyroid	43.6	35.2	23.8
Average Magnitude:			14.2
Standard Deviation:			8.1
Minimum:			-23.5
Maximum:			23.8

Volumetric Average Organ Dose Comparison

Organ	CAP Doses (mGy)		Percent Difference
	Simulated	Measured	
Lung	26.7	25.7	4.0
Breast	25.3	25.8	-2.1
Liver	24.1	27.2	-11.3
Stomach	20.9	26.2	-20.2
Ovary	18.0	21.8	-17.4
Uterus	17.3	20.2	-14.4
Average Magnitude:			11.6
Standard Deviation:			7.2
Minimum:			-20.2
Maximum:			4.0

Small Cadaver ATCM Exam Data Tables

Point Dose Comparison

Dose Point	CAP Doses (mGy)				CAP Percent Differences		
	Fixed-mA (Avg)	Attenuation-Based	Image-Based	Measured	Fixed-mA (Avg)	Attenuation-Based	Image-Based
Lung - 1	12.0	10.6	9.9	9.1	32.0	16.6	8.9
Lung - 2	12.2	10.8	10.1	9.5	28.4	13.7	6.0
Lung - 3	12.8	11.7	10.7	9.9	29.8	18.6	8.5
Lung - 4	13.2	12.0	11.0	9.6	37.2	24.2	14.1
Lung - 5	9.7	8.3	7.9	11.6	-17.0	-28.5	-31.7
Lung - 6	10.3	8.9	8.5	12.8	-19.4	-30.0	-33.6
Lung - 7	14.5	13.6	12.2	13.8	4.9	-1.7	-11.4
Lung - 8	12.3	11.2	10.3	14.5	-15.2	-22.7	-29.1
Breast - 1	10.1	10.0	8.9	11.5	-12.0	-13.3	-22.4
Breast - 2	9.7	9.6	8.6	12.8	-24.0	-25.1	-33.1
Breast - 3	9.6	9.5	8.4	12.1	-20.5	-21.6	-30.3
Breast - 4	11.9	11.4	10.1	12.4	-4.5	-8.5	-18.8
Breast - 5	9.5	9.4	8.4	8.4	13.6	12.1	0.0
Breast - 6	12.5	12.3	11.0	10.8	15.6	14.0	1.7
Breast - 7	11.1	10.6	9.4	9.5	16.7	12.2	-0.5
Breast - 8	11.8	11.4	10.1	8.3	42.3	37.3	21.6
Breast - 9	11.1	10.8	9.5	9.0	23.0	19.2	5.3
Breast - 10	11.2	10.9	9.7	8.4	32.3	29.4	14.5
Liver - 1	12.9	12.7	11.4	11.7	11.0	8.6	-2.2
Liver - 2	13.3	12.9	11.6	11.3	17.4	14.1	2.2
Liver - 3	12.8	12.5	11.2	12.4	4.0	1.0	-9.5
Liver - 4	11.2	10.8	10.1	12.6	-11.1	-14.2	-20.2
Liver - 5	11.5	11.1	10.4	13.3	-13.0	-16.1	-22.1
Stomach - 1	12.4	12.1	10.9	11.1	12.0	9.5	-1.4
Stomach - 2	14.0	13.6	12.4	10.9	28.6	24.7	14.4
Small Intestine	15.3	16.4	14.3	14.6	4.9	12.5	-2.3
Colon - 1	11.0	12.3	10.4	15.0	-27.1	-18.0	-31.0
Colon - 2	11.1	12.4	10.5	11.9	-6.5	4.5	-11.8
Uterus	12.6	15.1	12.8	14.1	-11.2	6.9	-9.6
Ovary	10.6	12.8	10.8	8.5	25.3	51.2	27.9
				Average Magnitude:	18.7	17.7	14.9
				Standard Deviation:	10.2	10.7	11.2
				Minimum:	-27.1	-30.0	-33.6
				Maximum:	42.3	51.2	27.9

Dose Point	Chest Doses (mGy)				Chest Percent Differences		
	Fixed-mA (Avg)	Attenuation-Based	Image-Based	Measured	Fixed-mA (Avg)	Attenuation-Based	Image-Based
Lung - 1	9.2	9.3	8.6	7.3	27.1	28.3	18.1
Lung - 2	9.2	9.3	8.6	7.8	17.3	18.6	9.9
Lung - 3	8.4	8.9	8.7	8.1	3.5	9.1	7.2
Lung - 4	9.8	10.1	9.7	7.9	23.5	27.7	22.0
Lung - 5	7.2	7.1	6.5	9.0	-19.2	-20.5	-27.1
Lung - 6	6.4	6.4	5.9	9.3	-31.0	-31.1	-36.7
Lung - 7	7.9	8.4	8.4	10.3	-23.3	-18.2	-19.0
Lung - 8	8.7	9.1	8.9	10.2	-15.3	-10.9	-12.7
Breast -1	6.5	7.3	7.6	9.6	-32.3	-24.4	-21.0
Breast -2	6.1	6.9	7.1	9.0	-32.6	-23.6	-21.3
Breast -3	6.1	7.0	7.2	8.8	-30.4	-20.4	-18.6
Breast -4	7.6	8.1	8.1	10.3	-26.2	-20.8	-20.9
Breast -5	5.8	6.5	6.8	10.3	-43.7	-36.6	-34.3
Breast -6	8.9	10.1	10.4	8.8	1.4	15.1	18.9
Breast -7	7.4	8.0	8.0	7.3	1.3	9.7	9.8
Breast -8	8.5	9.4	9.5	7.3	15.9	28.3	29.5
Breast -9	7.4	8.4	8.5	6.5	13.4	28.1	30.1
Breast -10	6.9	7.8	8.0	7.5	-7.9	5.0	7.1
Liver - 1	9.0	10.1	10.4	9.6	-5.8	5.1	9.1
Liver - 2	7.8	8.7	8.8	9.7	-20.1	-10.8	-9.1
Liver - 3	7.5	8.4	8.6	9.8	-23.2	-14.4	-12.7
Liver - 4	7.6	8.4	8.8	10.2	-24.9	-17.4	-13.0
Liver - 5	7.4	8.1	8.6	10.2	-27.8	-20.3	-16.2
Stomach -1	8.4	9.4	9.8	6.9	21.9	35.8	40.8
Stomach -2	7.6	8.4	8.8	9.6	-20.2	-11.7	-7.7
Average Magnitude:					20.4	19.7	18.9
Standard Deviation:					10.6	8.9	9.7
Minimum:					-43.7	-36.6	-36.7
Maximum:					27.1	35.8	40.8

Dose Point	Abdomen Doses (mGy)				Abdomen Percent Differences		
	Fixed-mA (Avg)	Attenuation-Based	Image-Based	Measured	Fixed-mA (Avg)	Attenuation-Based	Image-Based
Lung - 3	8.1	7.6	7.8	7.6	6.3	0.0	2.0
Lung - 4	5.8	5.5	5.6	7.3	-21.2	-25.7	-24.4
Lung - 7	8.6	8.2	8.3	10.3	-16.1	-20.8	-19.3
Lung - 8	8.0	7.5	7.7	9.7	-17.1	-22.1	-20.5
Breast -1	8.9	8.7	8.7	10.3	-13.2	-15.7	-15.3
Breast -2	8.3	8.2	8.1	10.2	-18.7	-19.8	-20.4
Breast -3	8.2	8.2	8.1	10.2	-19.3	-19.6	-20.8
Breast -4	9.3	8.8	8.9	11.5	-19.2	-24.1	-22.5
Breast -5	7.9	7.7	7.7	10.6	-25.8	-27.3	-27.4
Breast -6	12.2	12.0	11.9	9.0	36.0	34.2	33.3
Breast -7	9.3	8.8	9.0	7.8	20.4	13.8	15.7
Breast -8	11.0	10.6	10.7	8.6	28.6	24.2	24.6
Breast -9	9.7	9.6	9.5	8.4	15.6	14.0	13.1
Breast -10	9.2	9.2	9.0	8.0	14.7	14.1	12.6
Liver - 1	12.3	12.0	12.0	11.3	9.3	6.3	6.7
Liver - 2	10.0	9.8	9.8	7.2	39.0	36.4	35.9
Liver - 3	9.6	9.4	9.4	10.2	-5.6	-7.4	-7.8
Liver - 4	11.1	10.7	10.8	7.3	52.6	46.1	48.0
Liver - 5	10.6	10.2	10.3	10.1	4.8	0.8	2.0
Stomach -1	11.5	11.2	11.2	9.7	18.8	15.5	15.9
Stomach -2	10.7	10.4	10.4	9.7	10.3	6.5	7.4
Small Intestine	10.9	11.5	11.2	13.9	-21.3	-17.5	-19.4
Colon - 1	6.8	7.4	7.2	7.6	-10.9	-2.2	-5.3
Colon - 2	7.4	8.1	7.9	9.2	-19.4	-11.9	-14.5
Average Magnitude:					19.3	17.7	18.1
Standard Deviation:					11.1	11.4	11.0
Minimum:					-25.8	-27.3	-27.4
Maximum:					52.6	46.1	48.0

Dose Point	Pelvis Doses (mGy)				Pelvis Percent Differences		
	Fixed-mA (Avg)	Attenuation-Based	Image-Based	Measured	Fixed-mA (Avg)	Attenuation-Based	Image-Based
Small Intestine	8.2	8.3	8.1	9.3	-11.7	-10.5	-12.4
Colon - 1	10.3	10.7	10.5	12.2	-15.2	-12.5	-13.5
Colon - 2	10.2	10.4	10.3	10.2	-0.4	2.2	0.7
Uterus	14.2	15.3	15.4	12.9	10.2	19.2	19.8
Ovary	12.0	13.0	13.0	11.8	1.2	9.8	10.1
Average Magnitude:					7.7	10.8	11.3
Standard Deviation:					6.6	6.1	6.9
Minimum:					-15.2	-12.5	-13.5
Maximum:					10.2	19.2	19.8

Point-Dose-Derived Average Organ Dose Comparison

Organ Doses from Points

Organ	CAP Doses (mGy)				CAP Percent Differences		
	Fixed-mA (Avg)	Attenuation-Based	Image-Based	Measured	Fixed-mA (Avg)	Attenuation-Based	Image-Based
Lung	12.1	10.9	10.1	11.4	6.3	-4.5	-11.7
Breast	10.8	10.6	9.4	10.3	5.3	2.7	-8.7
Liver	12.4	12.0	10.9	12.2	1.3	-1.6	-10.6
Stomach	13.2	12.9	11.7	11.0	20.0	16.8	6.3
Small Intestine	15.3	16.4	14.3	14.6	4.9	12.5	-2.3
Colon	11.0	12.4	10.5	13.5	-18.2	-8.2	-22.6
Uterus	12.6	15.1	12.8	14.1	-10.9	7.2	-9.4
Ovary	10.6	12.8	10.8	8.5	24.9	50.7	27.4
Average Magnitude:					11.5	13.0	12.4
Standard Deviation:					8.5	16.0	8.4
Minimum:					-18.2	-8.2	-22.6
Maximum:					24.9	50.7	27.4

Organ	Chest Doses (mGy)				Chest Percent Differences		
	Fixed-mA (Avg)	Attenuation-Based	Image-Based	Measured	Fixed-mA (Avg)	Attenuation-Based	Image-Based
Lung	8.4	8.6	8.2	8.7	-4.0	-1.4	-6.3
Breast	7.1	8.0	8.1	8.5	-16.4	-6.5	-4.6
Liver	7.9	8.7	9.1	9.9	-20.6	-11.8	-8.6
Stomach	8.0	8.9	9.3	8.2	-1.9	8.9	13.3
Average Magnitude:					10.7	7.1	8.2
Standard Deviation:					9.2	4.4	3.8
Minimum:					-20.6	-11.8	-8.6
Maximum:					-1.9	8.9	13.3

Organ	Abdomen Doses (mGy)				Abdomen Percent Differences		
	Fixed-mA (Avg)	Attenuation-Based	Image-Based	Measured	Fixed-mA (Avg)	Attenuation-Based	Image-Based
Breast	9.4	9.2	9.2	9.5	-1.0	-3.5	-3.6
Liver	10.7	10.4	10.5	9.2	16.6	13.2	13.6
Stomach	11.1	10.8	10.8	9.7	14.4	10.9	11.5
Small Intestine	10.9	11.5	11.2	13.9	-21.3	-17.5	-19.4
Colon	7.1	7.8	7.5	8.4	-15.7	-7.6	-10.4
Average Magnitude:					13.8	10.5	11.7
Standard Deviation:					7.6	5.3	5.7
Minimum:					-21.3	-17.5	-19.4
Maximum:					16.6	13.2	13.6

Organ	Pelvis Doses (mGy)				Pelvis Percent Differences		
	Fixed-mA (Avg)	Attenuation-Based	Image-Based	Measured	Fixed-mA (Avg)	Attenuation-Based	Image-Based
Small Intestine	8.2	8.3	8.1	9.3	-12.1	-10.9	-12.8
Colon	10.3	10.6	10.4	11.2	-8.4	-5.8	-7.1
Uterus	14.2	15.3	15.4	12.9	9.9	18.8	19.5
Ovary	12.0	13.0	13.0	11.8	1.4	10.0	10.3
Average Magnitude:					7.9	11.4	12.4
Standard Deviation:					4.6	5.4	5.3
Minimum:					-12.1	-10.9	-12.8
Maximum:					9.9	18.8	19.5

Volumetric Average Organ Dose Comparison

Organ	CAP Doses (mGy)				CAP Percent Differences		
	Fixed-mA (Avg)	Attenuation-Based	Image-Based	Measured	Fixed-mA (Avg)	Attenuation-Based	Image-Based
Lung	14.0	12.6	11.7	11.4	22.6	10.5	2.4
Breast	10.0	9.8	8.7	10.3	-3.1	-5.0	-15.2
Liver	11.6	11.3	10.4	12.2	-4.8	-7.5	-15.1
Stomach	13.2	12.8	11.9	11.0	20.2	16.7	8.4
Ovary	10.5	12.4	10.6	8.5	23.5	46.1	24.6
Uterus	11.6	14.0	11.8	14.1	-17.7	-0.8	-16.2
Average Magnitude:					15.3	14.4	13.6
Standard Deviation:					9.0	16.4	7.6
Minimum:					-17.7	-7.5	-16.2
Maximum:					23.5	46.1	24.6

Organ	Chest Doses (mGy)				Chest Percent Differences		
	Fixed-mA (Avg)	Attenuation-Based	Image-Based	Measured	Fixed-mA (Avg)	Attenuation-Based	Image-Based
Lung	9.1	9.4	9.0	8.7	4.5	7.7	3.2
Breast	6.4	7.2	7.4	8.5	-24.8	-15.1	-12.5
Liver	7.0	7.7	8.0	9.9	-29.8	-22.4	-19.2
Stomach	7.9	8.7	9.1	8.2	-4.0	5.7	10.9
Average Magnitude:					15.8	12.7	11.4
Standard Deviation:					13.4	7.6	6.6
Minimum:					-29.8	-22.4	-19.2
Maximum:					4.5	7.7	10.9

Organ	Abdomen Doses (mGy)				Abdomen Percent Differences		
	Fixed-mA (Avg)	Attenuation-Based	Image-Based	Measured	Fixed-mA (Avg)	Attenuation-Based	Image-Based
Breast	8.8	8.6	8.6	9.5	-7.8	-9.5	-9.8
Liver	10.0	9.7	9.7	9.2	8.9	5.2	5.9
Stomach	12.0	11.6	11.7	9.7	24.0	19.2	20.4
Average Magnitude:					13.6	11.3	12.0
Standard Deviation:					9.1	7.2	7.5
Minimum:					-7.8	-9.5	-9.8
Maximum:					24.0	19.2	20.4

Organ	Pelvis Doses (mGy)				Pelvis Percent Differences		
	Fixed-mA (Avg)	Attenuation-Based	Image-Based	Measured	Fixed-mA (Avg)	Attenuation-Based	Image-Based
Ovaries	11.7	12.5	12.6	11.8	-0.6	5.8	7.1
Uterus	13.1	14.2	14.2	12.9	1.5	9.9	10.3
Average Magnitude:					1.0	7.9	8.7
Standard Deviation:					0.6	2.9	2.3
Minimum:					-0.6	5.8	7.1
Maximum:					1.5	9.9	10.3

Console Average Effective mAs ATCM Exam Data

Point dose comparison

Dose Point	CAP Doses (mGy)		Percent Difference
	Attenuation-Based	Measured	
Lung - 1	19.2	9.1	111.3
Lung - 2	19.6	9.5	106.0
Lung - 3	21.3	9.9	114.9
Lung - 4	21.7	9.6	125.0
Lung - 5	15.1	11.6	29.5
Lung - 6	16.2	12.8	26.7
Lung - 7	24.6	13.8	78.2
Lung - 8	20.3	14.5	40.1
Breast - 1	18.0	11.5	57.2
Breast - 2	17.4	12.8	35.7
Breast - 3	17.1	12.1	42.0
Breast - 4	20.6	12.4	65.7
Breast - 5	17.0	8.4	103.0
Breast - 6	22.3	10.8	106.5
Breast - 7	19.3	9.5	103.4
Breast - 8	20.6	8.3	148.7
Breast - 9	19.5	9.0	116.0
Breast - 10	19.8	8.4	134.4
Liver - 1	22.9	11.7	96.7
Liver - 2	23.4	11.3	106.7
Liver - 3	22.6	12.4	82.9
Liver - 4	19.6	12.6	55.5
Liver - 5	20.2	13.3	52.0
Stomach - 1	22.0	11.1	98.3
Stomach - 2	24.6	10.9	126.0
Small Intestine	29.8	14.6	103.9
Colon - 1	22.4	15.0	48.7
Colon - 2	22.5	11.9	89.2
Uterus	27.4	14.1	93.6
Ovary	23.2	8.5	174.0
Average Magnitude:			89.1
Standard Deviation:			37.0
Minimum:			26.7
Maximum:			174.0

Dose Point	Chest Doses (mGy)		Percent Difference
	Attenuation-Based	Measured	
Lung - 1	15.8	7.3	117.6
Lung - 2	15.8	7.8	101.2
Lung - 3	15.0	8.1	85.1
Lung - 4	17.2	7.9	116.6
Lung - 5	12.1	9.0	34.8
Lung - 6	10.8	9.3	16.8
Lung - 7	14.3	10.3	38.7
Lung - 8	15.5	10.2	51.2
Breast -1	12.3	9.6	28.3
Breast -2	11.7	9.0	29.6
Breast -3	11.9	8.8	35.1
Breast -4	13.8	10.3	34.4
Breast -5	11.1	10.3	7.6
Breast -6	17.1	8.8	95.2
Breast -7	13.6	7.3	86.1
Breast -8	15.9	7.3	117.7
Breast -9	14.2	6.5	117.3
Breast -10	13.3	7.5	78.1
Liver - 1	17.0	9.6	78.3
Liver - 2	14.7	9.7	51.3
Liver - 3	14.3	9.8	45.3
Liver - 4	14.2	10.2	40.1
Liver - 5	13.8	10.2	35.2
Stomach -1	16.0	6.9	130.4
Stomach -2	14.3	9.6	49.8
	Average Magnitude:		64.9
	Standard Deviation:		37.0
	Minimum:		7.6
	Maximum:		130.4

Dose Point	Abdomen Doses (mGy)		Percent Difference
	Attenuation-Based	Measured	
Lung - 3	12.8	7.6	68.4
Lung - 4	9.2	7.3	25.0
Lung - 7	13.7	10.3	33.3
Lung - 8	12.7	9.7	31.1
Breast -1	14.6	10.3	42.0
Breast -2	13.7	10.2	35.1
Breast -3	13.8	10.2	35.4
Breast -4	14.7	11.5	27.8
Breast -5	13.0	10.6	22.5
Breast -6	20.2	9.0	125.9
Breast -7	14.8	7.8	91.6
Breast -8	17.9	8.6	109.1
Breast -9	16.1	8.4	92.0
Breast -10	15.4	8.0	92.1
Liver - 1	20.1	11.3	79.0
Liver - 2	16.5	7.2	129.7
Liver - 3	15.9	10.2	56.0
Liver - 4	17.9	7.3	145.9
Liver - 5	17.1	10.1	69.7
Stomach -1	18.8	9.7	94.5
Stomach -2	17.4	9.7	79.3
Small Intestine	19.3	13.9	38.8
Colon - 1	12.5	7.6	64.6
Colon - 2	13.6	9.2	48.4
Average Magnitude:			68.2
Standard Deviation:			36.1
Minimum:			22.5
Maximum:			145.9

Dose Point	Pelvis Doses (mGy)		Percent Difference
	Attenuation-Based	Measured	
Small Intestine	12.8	9.3	37.9
Colon - 1	16.4	12.2	34.9
Colon - 2	16.1	10.2	57.4
Uterus	23.6	12.9	83.7
Ovary	20.0	11.8	69.2
Average Magnitude:			56.6
Standard Deviation:			20.7
Minimum:			34.9
Maximum:			83.7

Point-dose-derived average organ dose comparison

Organ	CAP Doses (mGy)		Percent Difference
	Attenuation-Based	Measured	
Lung	19.7	11.4	73.1
Breast	19.2	10.3	86.1
Liver	21.7	12.2	78.2
Stomach	23.3	11.0	111.6
Small Intestine	29.8	14.6	103.9
Colon	22.4	13.5	66.3
Uterus	27.4	14.1	94.2
Ovary	23.2	8.5	173.0
Average Magnitude:			98.3
Standard Deviation:			33.9
Minimum:			66.3
Maximum:			173.0

Organ	Chest Doses (mGy)		Percent Difference
	Attenuation-Based	Measured	
Lung	14.6	8.7	67.3
Breast	13.5	8.5	58.7
Liver	14.8	9.9	49.6
Stomach	15.1	8.2	84.7
Average Magnitude:			65.1
Standard Deviation:			15.0
Minimum:			49.6
Maximum:			84.7

Organ	Abdomen Doses (mGy)		Percent Difference
	Attenuation-Based	Measured	
Breast	15.4	9.5	62.5
Liver	17.5	9.2	90.5
Stomach	18.1	9.7	86.8
Small Intestine	19.3	13.9	38.9
Colon	13.1	8.4	55.5
Average Magnitude:			66.8
Standard Deviation:			21.7
Minimum:			38.9
Maximum:			90.5

Organ	Pelvis Doses (mGy)		Percent Difference
	Attenuation-Based	Measured	
Small Intestine	12.8	9.3	37.3
Colon	16.3	11.2	45.1
Uterus	23.6	12.9	83.1
Ovary	20.0	11.8	69.5
Average Magnitude:			58.8
Standard Deviation:			21.2
Minimum:			37.3
Maximum:			83.1

Volumetric average organ dose comparison

Organ	CAP Doses (mGy)		Percent Difference
	Attenuation-Based	Measured	
Lung	22.8	11.4	100.2
Breast	17.7	10.3	72.2
Liver	20.5	12.2	67.7
Stomach	23.3	11.0	111.5
Ovary	22.5	8.5	164.7
Uterus	25.3	14.1	79.8
Average Magnitude:			99.3
Standard Deviation:			36.2
Minimum:			67.7
Maximum:			164.7

Organ	Chest Doses (mGy)		Percent Difference
	Attenuation-Based	Measured	
Lung	15.9	8.7	82.7
Breast	12.2	8.5	44.1
Liver	13.0	9.9	31.6
Stomach	14.7	8.2	79.4
Average Magnitude:			59.4
Standard Deviation:			25.5
Minimum:			31.6
Maximum:			82.7

Organ	Abdomen Doses (mGy)		Percent Difference
	Attenuation-Based	Measured	
Breast	14.5	9.5	52.4
Liver	16.3	9.2	77.1
Stomach	19.5	9.7	100.6
Average Magnitude:			76.7
Standard Deviation:			24.1
Minimum:			52.4
Maximum:			100.6

Organ	Pelvis Doses (mGy)		Percent Difference
	Attenuation-Based	Measured	
Ovaries	19.2	11.8	63.1
Uterus	21.8	12.9	69.4
Average Magnitude:			66.2
Standard Deviation:			4.4
Minimum:			63.1
Maximum:			69.4

Medium Cadaver ATCM Exam Data Tables

Point Dose Comparison

Dose Point	CAP Doses (mGy)				CAP Percent Differences		
	Fixed-mA (Avg)	Attenuation-Based	Image-Based	Measured	Fixed-mA (Avg)	Attenuation-Based	Image-Based
Lung - 1	18.6	15.7	17.1	17.4	7.1	-9.8	-1.7
Lung - 2	20.0	17.2	18.4	15.4	30.2	11.9	19.9
Lung - 3	21.2	17.9	19.4	17.8	19.0	0.4	9.2
Lung - 4	22.6	19.4	20.8	19.7	14.7	-1.6	5.5
Lung - 5	22.4	20.6	20.9	20.9	7.5	-1.5	0.1
Lung - 6	23.1	21.3	21.5	20.9	10.5	1.9	3.1
Breast -1	26.0	23.9	24.2	21.8	19.4	9.6	11.1
Breast -2	23.5	21.8	21.9	21.9	7.2	-0.5	0.0
Breast -3	25.2	22.9	23.6	28.1	-10.2	-18.4	-15.9
Breast -4	25.8	23.1	24.0	26.2	-1.8	-12.0	-8.4
Breast -5	23.5	21.1	21.8	23.7	-0.9	-11.0	-8.1
Breast -6	27.3	25.6	25.5	21.8	25.2	17.1	17.0
Breast -7	25.8	23.4	24.1	25.7	0.3	-9.1	-6.1
Breast -8	26.1	22.8	23.9	21.5	21.5	6.0	11.3
Breast -9	26.0	23.4	24.3	23.0	13.2	2.1	5.8
Breast -10	23.7	21.7	22.0	23.2	2.2	-6.5	-5.0
Liver - 1	22.4	22.2	21.3	17.6	27.4	26.0	20.8
Liver - 2	24.3	24.0	23.0	20.9	16.4	15.1	10.3
Liver - 3	23.3	23.0	22.0	21.7	7.3	6.1	1.5
Liver - 4	24.0	23.5	22.6	18.6	28.6	26.0	21.5
Liver - 5	24.7	24.3	23.3	17.9	38.1	36.0	30.6
Lung -7	23.8	21.9	22.1	18.9	25.9	15.9	16.9
Lung -8	23.2	21.5	21.6	19.2	20.5	12.0	12.1
Stomach -1	26.5	24.8	24.7	25.2	5.2	-1.3	-2.0
Stomach -2	31.9	30.2	29.8	23.6	35.4	28.0	26.2
Small Intestine - 1	23.2	25.9	24.1	18.5	25.7	40.1	30.6
Small Intestine - 2	23.5	26.9	24.8	26.7	-12.0	0.6	-7.3
Colon - 1	21.8	25.9	24.3	24.5	-11.0	5.7	-0.7
Colon - 2	17.6	20.9	19.7	21.3	-17.4	-1.9	-7.5
Uterus	16.8	17.5	18.1	19.0	-11.7	-7.9	-4.7
Ovary - 1	18.6	19.7	20.4	24.0	-22.4	-17.7	-14.9
Ovary - 2	19.0	19.7	20.4	20.1	-5.4	-1.9	1.8
Thyroid - 1	35.2	21.2	31.8	29.6	18.7	-28.4	7.2
Thyroid - 2	31.8	19.6	28.7	27.2	16.7	-28.2	5.5
Average Magnitude:					15.8	12.3	10.3
Standard Deviation:					10.0	11.0	8.5
Minimum:					-22.4	-28.4	-15.9
Maximum:					38.1	40.1	30.6

Dose Point	Chest Doses (mGy)				Chest Percent Differences		
	Fixed-mA (Avg)	Attenuation-Based	Image-Based	Measured	Fixed-mA (Avg)	Attenuation-Based	Image-Based
Lung - 1	11.8	11.4	11.5	11.0	7.3	3.4	4.0
Lung - 2	12.5	12.4	12.3	12.7	-1.2	-2.4	-3.1
Lung - 3	13.4	13.0	13.0	13.9	-3.2	-6.4	-6.3
Lung - 4	14.2	14.0	13.9	13.7	3.6	2.4	1.4
Lung - 5	13.6	14.5	14.1	18.1	-24.7	-19.7	-22.3
Lung - 6	14.0	15.0	14.5	14.7	-4.9	2.0	-1.4
Breast -1	15.8	16.9	16.6	19.3	-18.2	-12.3	-14.1
Breast -2	14.3	15.5	14.9	15.3	-6.7	1.2	-2.9
Breast -3	15.4	16.4	15.7	17.8	-13.4	-8.0	-11.9
Breast -4	15.8	16.6	15.9	21.0	-24.8	-21.3	-24.3
Breast -5	14.2	14.9	15.0	18.1	-21.8	-17.9	-17.3
Breast -6	16.6	18.2	17.4	12.9	29.3	41.6	34.9
Breast -7	15.8	16.7	16.0	13.5	17.0	24.1	18.7
Breast -8	16.0	16.4	15.7	19.7	-18.7	-17.0	-20.6
Breast -9	15.9	16.8	16.1	12.5	26.9	33.8	28.5
Breast -10	14.4	15.4	15.2	15.4	-6.8	-0.1	-1.7
Liver - 1	12.5	14.3	13.3	10.7	16.7	33.7	24.5
Liver - 2	13.6	15.6	14.5	17.5	-22.5	-11.2	-17.3
Liver - 3	13.1	15.0	14.0	18.4	-28.9	-18.4	-24.0
Liver - 4	13.5	15.4	14.4	14.1	-4.0	9.0	2.3
Liver - 5	13.9	15.9	14.8	14.8	-6.3	7.0	0.0
Lung -7	14.1	15.1	14.9	15.5	-9.0	-2.5	-4.2
Lung -8	13.6	14.7	14.4	16.4	-17.0	-10.3	-12.5
Stomach -1	15.4	16.9	16.4	15.7	-1.9	7.2	4.0
Stomach -2	18.7	20.6	19.9	16.0	17.2	29.3	24.7
Thyroid -1	24.8	16.8	21.5	21.0	18.1	-20.1	2.2
Thyroid - 2	22.1	15.3	19.2	21.5	3.0	-28.8	-10.4
Average Magnitude:					13.8	14.5	12.6
Standard Deviation:					9.1	11.6	10.3
Minimum:					-28.9	-28.8	-24.3
Maximum:					29.3	41.6	34.9

Dose Point	Abdomen Doses (mGy)				Abdomen Percent Differences		
	Fixed-mA (Avg)	Attenuation-Based	Image-Based	Measured	Fixed-mA (Avg)	Attenuation-Based	Image-Based
Liver - 1	21.6	16.4	16.9	16.6	29.7	-1.6	1.6
Liver - 2	23.8	17.9	18.5	19.9	19.7	-9.9	-6.8
Liver - 3	22.0	17.4	18.0	20.7	6.5	-15.6	-12.7
Liver - 4	19.7	17.1	17.8	16.6	19.3	3.1	7.3
Liver - 5	22.1	18.0	18.6	17.2	28.4	4.5	8.3
Lung -7	15.2	11.2	12.2	13.5	12.8	-16.5	-9.1
Lung -8	18.6	12.6	13.7	15.5	20.0	-18.2	-11.2
Stomach -1	21.3	16.6	18.0	17.8	19.9	-6.5	1.3
Stomach -2	25.6	22.1	23.8	20.7	23.5	6.5	15.0
Small Intestine - 1	20.4	22.3	22.0	20.2	1.0	10.1	8.8
Small Intestine - 2	24.1	23.2	22.6	25.1	-3.8	-7.7	-10.0
Colon - 1	18.9	21.7	21.1	20.6	-8.0	5.2	2.3
Colon - 2	16.9	17.3	16.9	18.3	-7.4	-5.1	-7.6
Average Magnitude:					15.4	8.5	7.8
Standard Deviation:					9.4	5.3	4.2
Minimum:					-8.0	-18.2	-12.7
Maximum:					29.7	10.1	15.0

Dose Point	Pelvis Doses (mGy)				Pelvis Percent Differences		
	Fixed-mA (Avg)	Attenuation-Based	Image-Based	Measured	Fixed-mA (Avg)	Attenuation-Based	Image-Based
Colon - 2	7.3	9.1	7.8	13.9	-48.0	-34.5	-44.2
Uterus	16.9	17.6	17.4	18.0	-5.9	-2.6	-3.6
Ovary - 1	17.3	18.5	18.0	25.5	-31.9	-27.4	-29.5
Ovary - 2	19.0	19.6	19.4	22.2	-14.4	-11.4	-12.3
Average Magnitude:					25.0	19.0	22.4
Standard Deviation:					18.7	14.6	18.1
Minimum:					-48.0	-34.5	-44.2
Maximum:					-5.9	-2.6	-3.6

Point-Dose-Derived Average Organ Dose Comparison

Organ	CAP Doses (mGy)				CAP Percent Differences		
	Fixed-mA (Avg)	Attenuation-Based	Image-Based	Measured	Fixed-mA (Avg)	Attenuation-Based	Image-Based
Lung	21.9	19.4	20.2	18.8	16.3	3.4	7.7
Breast	25.3	23.0	23.5	23.7	6.7	-3.2	-0.7
Liver	23.7	23.4	22.5	19.3	23.0	21.2	16.4
Stomach	29.2	27.5	27.2	24.4	19.6	12.8	11.5
Small Intestine	23.4	26.4	24.4	22.6	3.4	16.7	8.1
Colon	19.7	23.4	22.0	22.9	-14.0	2.2	-3.8
Uterus	16.8	17.5	18.1	19.0	-11.7	-7.9	-4.7
Ovary	18.8	19.7	20.4	22.0	-14.6	-10.5	-7.2
Thyroid	33.5	20.4	30.3	28.4	17.9	-28.2	6.5
Average Magnitude:					14.1	11.8	7.4
Standard Deviation:					6.2	8.9	4.5
Minimum:					-14.6	-28.2	-7.2
Maximum:					23.0	21.2	16.4

Organ	Chest Doses (mGy)				Chest Percent Differences		
	Fixed-mA (Avg)	Attenuation-Based	Image-Based	Measured	Fixed-mA (Avg)	Attenuation-Based	Image-Based
Lung	13.4	13.8	13.6	14.5	-7.5	-5.0	-6.6
Breast	15.4	16.4	15.8	16.6	-7.1	-1.4	-4.6
Liver	13.3	15.2	14.2	15.1	-11.9	0.8	-5.9
Stomach	17.1	18.8	18.1	15.8	8.1	18.7	14.8
Thyroid	23.5	16.0	20.4	21.2	10.6	-24.4	-4.0
Average Magnitude:					9.0	10.1	7.2
Standard Deviation:					2.1	10.8	4.4
Minimum:					-11.9	-24.4	-6.6
Maximum:					10.6	18.7	14.8

Organ	Abdomen Doses (mGy)				Abdomen Percent Differences		
	Fixed-mA (Avg)	Attenuation-Based	Image-Based	Measured	Fixed-mA (Avg)	Attenuation-Based	Image-Based
Liver	21.8	17.4	18.0	18.2	20.0	-4.7	-1.3
Stomach	23.4	19.3	20.9	19.2	22.1	0.7	8.9
Small Intestine	22.3	22.7	22.3	22.7	-1.9	0.0	-1.9
Colon	17.9	19.5	19.0	19.4	-7.6	0.5	-2.3
Average Magnitude:					12.9	1.5	3.6
Standard Deviation:					9.7	2.1	3.5
Minimum:					-7.6	-4.7	-2.3
Maximum:					22.1	0.7	8.9

Organ	Pelvis Doses (mGy)				Pelvis Percent Differences		
	Fixed-mA (Avg)	Attenuation-Based	Image-Based	Measured	Fixed-mA (Avg)	Attenuation-Based	Image-Based
Uterus	16.9	17.6	17.4	19.3	-12.2	-9.1	-10.1
Ovary	18.2	19.1	18.7	24.3	-25.3	-21.6	-23.0
Average Magnitude:					18.7	15.3	16.5
Standard Deviation:					9.3	8.8	9.2
Minimum:					-25.3	-21.6	-23.0
Maximum:					-12.2	-9.1	-10.1

Volumetric Average Organ Dose Comparison

Organ	CAP Doses (mGy)				CAP Percent Differences		
	Fixed-mA (Avg)	Attenuation-Based	Image-Based	Measured	Fixed-mA (Avg)	Attenuation-Based	Image-Based
Lung	25.7	22.9	23.9	18.8	36.5	22.0	27.0
Breast	25.4	22.8	23.6	23.7	7.2	-3.8	-0.3
Liver	23.5	23.4	22.9	19.3	21.7	21.1	18.5
Stomach	23.8	22.2	22.5	24.4	-2.5	-8.9	-7.8
Ovary	17.9	19.5	19.6	22.0	-18.5	-11.5	-10.9
Uterus	19.0	20.5	20.7	19.0	-0.2	7.6	8.9
Average Magnitude:					14.4	12.5	12.2
Standard Deviation:					13.8	7.5	9.3
Minimum:					-18.5	-11.5	-10.9
Maximum:					36.5	22.0	27.0

Organ	Chest Doses (mGy)				Chest Percent Differences		
	Fixed-mA (Avg)	Attenuation-Based	Image-Based	Measured	Fixed-mA (Avg)	Attenuation-Based	Image-Based
Lung	15.5	16.5	16.0	14.5	6.8	13.4	10.5
Breast	15.5	16.7	15.8	16.6	-6.4	0.4	-4.6
Liver	10.6	11.9	11.3	15.1	-29.8	-20.9	-25.0
Stomach	13.4	14.8	14.3	15.8	-15.1	-6.5	-9.4
Average Magnitude:					14.5	10.3	12.4
Standard Deviation:					10.9	8.9	8.8
Minimum:					-29.8	-20.9	-25.0
Maximum:					6.8	13.4	10.5

Organ	Abdomen Doses (mGy)				Abdomen Percent Differences		
	Fixed-mA (Avg)	Attenuation-Based	Image-Based	Measured	Fixed-mA (Avg)	Attenuation-Based	Image-Based
Liver	20.0	18.1	19.1	18.2	9.7	-0.3	4.8
Stomach	19.1	16.2	17.9	19.2	-0.4	-15.4	-7.0
Average Magnitude:					5.0	7.9	5.9
Standard Deviation:					6.6	10.7	1.6
Minimum:					-0.4	-15.4	-7.0
Maximum:					9.7	-0.3	4.8

Organ	Pelvis Doses (mGy)				Pelvis Percent Differences		
	Fixed-mA (Avg)	Attenuation-Based	Image-Based	Measured	Fixed-mA (Avg)	Attenuation-Based	Image-Based
Ovary	18.2	19.2	18.8	23.8	-23.5	-19.2	-20.9
Uterus	18.1	18.9	18.7	18.0	0.5	5.2	3.7
Average Magnitude:					12.0	12.2	12.3
Standard Deviation:					16.3	9.9	12.2
Minimum:					-23.5	-19.2	-20.9
Maximum:					0.5	5.2	3.7

Large Cadaver ATCM Exam Data Tables

Point Dose Comparison

Dose Point	CAP Doses (mGy)				CAP Percent Differences		
	Fixed-mA (Avg)	Attenuation-Based	Image-Based	Measured	Fixed-mA (Avg)	Attenuation-Based	Image-Based
Lung - 1	21.6	16.5	19.7	19.6	9.9	-16.1	0.2
Lung - 2	24.9	19.3	22.7	23.4	6.2	-17.7	-3.1
Lung - 3	20.4	17.0	18.7	19.8	2.9	-13.9	-5.5
Lung - 4	20.4	17.0	18.7	21.7	-6.0	-21.4	-13.7
Lung - 5	33.7	26.3	30.8	25.0	34.9	5.2	23.2
Lung - 6	31.4	24.5	28.7	22.7	38.3	8.2	26.3
Lung - 7	24.5	20.2	22.5	20.0	22.5	1.0	12.4
Lung - 8	25.6	21.3	23.5	23.1	10.9	-7.8	1.8
Breast - 1	24.3	22.4	22.5	24.0	1.3	-6.9	-6.4
Breast - 2	22.5	19.8	20.7	24.6	-8.6	-19.3	-15.7
Breast - 3	24.7	21.7	22.8	27.0	-8.6	-19.6	-15.6
Breast - 4	27.8	22.1	25.5	26.9	3.4	-18.1	-5.4
Breast - 5	22.9	20.3	21.2	26.6	-13.7	-23.6	-20.4
Breast - 6	19.1	17.8	17.7	26.5	-28.0	-32.7	-33.4
Breast - 7	21.8	19.4	20.2	25.5	-14.4	-23.7	-20.9
Breast - 8	21.2	17.4	19.5	23.0	-7.6	-24.1	-15.3
Breast - 9	20.5	16.3	18.8	23.1	-11.3	-29.3	-18.9
Breast - 10	19.3	16.8	17.8	22.6	-14.9	-25.7	-21.5
Liver - 1	25.7	24.3	23.8	21.5	19.8	12.9	11.0
Liver - 2	26.0	24.6	24.1	23.5	10.8	4.7	2.7
Liver - 3	25.9	24.5	24.0	27.3	-5.2	-10.4	-12.2
Liver - 4	23.7	22.0	22.0	20.5	15.9	7.6	7.2
Liver - 5	28.0	26.1	25.9	21.3	31.6	22.9	21.7
Stomach - 1	19.7	21.2	18.7	24.3	-18.6	-12.6	-22.9
Stomach - 2	21.4	23.2	20.3	28.6	-25.0	-18.9	-29.0
Small Intestine -1	24.4	29.5	24.1	27.9	-12.5	5.7	-13.9
Small Intestine -2	27.7	34.3	27.7	30.9	-10.5	11.1	-10.5
Colon - 1	20.6	25.7	21.3	26.9	-23.4	-4.5	-20.8
Colon - 2	16.9	21.3	17.8	25.9	-34.6	-17.6	-31.3
Uterus	18.4	22.9	21.1	22.1	-16.6	3.7	-4.7
Ovary - 1	18.7	23.6	21.4	19.1	-1.6	23.9	12.1
Ovary - 2	20.1	23.9	23.2	24.8	-19.1	-3.5	-6.6
Thyroid - 1	58.1	30.2	50.8	31.5	84.3	-4.3	61.2
Thyroid - 2	46.3	25.9	41.2	30.5	51.9	-15.1	35.2
Average Magnitude:					18.4	14.5	16.5
Standard Deviation:					16.5	8.4	12.3
Minimum:					-34.6	-32.7	-33.4
Maximum:					84.3	23.9	61.2

Dose Point	Chest Doses (mGy)				Chest Percent Differences		
	Fixed-mA (Avg)	Attenuation-Based	Image-Based	Measured	Fixed-mA (Avg)	Attenuation-Based	Image-Based
Lung - 1	12.7	12.0	12.2	11.6	9.7	3.5	5.2
Lung - 2	14.7	14.1	14.2	14.0	4.8	0.4	1.6
Lung - 3	11.8	12.1	12.1	12.2	-3.3	-0.8	-1.4
Lung - 4	11.8	12.1	12.1	12.1	-1.8	0.7	0.1
Lung - 5	19.9	19.2	19.4	18.5	7.5	3.8	4.9
Lung - 6	18.5	17.9	18.2	19.3	-3.9	-7.0	-5.6
Lung - 7	14.3	14.5	14.6	15.4	-7.2	-5.9	-5.6
Lung - 8	14.9	15.2	15.2	16.7	-10.9	-9.0	-9.0
Breast -1	14.0	15.8	14.6	17.1	-18.0	-7.7	-14.6
Breast -2	13.1	14.2	13.5	19.7	-33.7	-28.0	-31.2
Breast -3	14.5	15.7	15.0	19.9	-27.5	-21.2	-24.7
Breast -4	16.4	16.1	16.4	20.3	-19.1	-20.6	-19.4
Breast -5	13.4	14.6	13.9	19.8	-32.6	-26.6	-30.0
Breast -6	10.8	12.4	11.3	12.4	-12.8	-0.6	-8.8
Breast -7	12.8	14.1	13.3	17.7	-27.8	-20.5	-24.8
Breast -8	12.4	12.6	12.7	15.0	-17.0	-16.0	-15.2
Breast -9	12.1	11.9	12.0	12.1	-0.5	-2.1	-0.9
Breast -10	11.2	12.0	11.6	14.3	-21.5	-15.7	-18.8
Liver - 1	14.0	15.8	14.7	16.1	-13.4	-2.0	-8.7
Liver - 2	14.1	16.0	14.9	17.5	-19.5	-8.9	-15.1
Liver - 3	14.1	15.9	14.8	17.7	-20.6	-10.0	-16.2
Liver - 4	13.3	14.9	13.9	13.7	-3.4	8.7	0.9
Liver - 5	15.6	17.7	16.4	15.1	3.2	16.9	8.1
Stomach -1	8.5	10.4	9.3	12.5	-32.0	-16.2	-25.7
Stomach -2	9.3	11.6	10.2	12.1	-23.2	-4.1	-15.7
Thyroid -1	34.5	22.3	30.6	23.5	47.1	-5.1	30.5
Thyroid -2	27.5	19.1	24.5	21.1	30.3	-9.5	15.9
Average Magnitude:					16.7	10.1	13.3
Standard Deviation:					12.1	8.2	9.8
Minimum:					-33.7	-28.0	-31.2
Maximum:					47.1	16.9	30.5

Dose Point	Abdomen Doses (mGy)				Abdomen Percent Differences		
	Fixed-mA (Avg)	Attenuation-Based	Image-Based	Measured	Fixed-mA (Avg)	Attenuation-Based	Image-Based
Breast -1	18.9	16.0	18.1	19.6	-3.7	-18.2	-7.9
Breast -5	16.3	13.5	15.6	17.0	-3.8	-20.7	-8.0
Breast -6	15.8	13.5	15.1	19.2	-18.0	-29.8	-21.4
Liver - 1	22.2	19.0	21.3	22.2	0.0	-14.4	-3.7
Liver - 2	22.6	19.4	21.8	16.7	35.3	15.9	30.2
Liver - 3	22.7	19.4	21.9	25.2	-10.0	-23.0	-13.4
Liver - 4	18.5	16.0	17.8	18.1	2.2	-12.1	-1.9
Liver - 5	23.5	20.0	22.5	18.2	29.0	10.1	23.8
Stomach -1	17.9	17.3	17.6	21.9	-18.3	-21.1	-19.7
Stomach -2	19.7	19.1	19.3	23.0	-14.4	-17.0	-15.9
Small Intestine -1	22.5	24.3	22.8	25.5	-11.6	-4.7	-10.7
Small Intestine -2	25.6	28.3	26.1	25.6	-0.2	10.5	2.0
Colon - 1	18.1	20.1	18.8	22.0	-17.4	-8.2	-14.5
Colon - 2	14.0	15.6	14.5	18.9	-26.0	-17.3	-23.3
Average Magnitude:					13.6	15.9	14.0
Standard Deviation:					11.2	6.6	8.8
Minimum:					-26.0	-29.8	-23.3
Maximum:					35.3	15.9	30.2

Dose Point	Pelvis Doses (mGy)				Pelvis Percent Differences		
	Fixed-mA (Avg)	Attenuation-Based	Image-Based	Measured	Fixed-mA (Avg)	Attenuation-Based	Image-Based
Colon - 2	9.3	10.4	9.4	17.1	-45.3	-39.3	-44.8
Uterus	18.1	19.4	18.8	19.3	-6.2	0.5	-2.8
Ovary - 1	18.3	19.9	19.0	24.1	-24.1	-17.6	-21.2
Ovary - 2	20.1	20.6	20.6	24.5	-18.0	-15.9	-15.6
Average Magnitude:					23.4	18.4	21.1
Standard Deviation:					16.4	16.0	17.6
Minimum:					-45.3	-39.3	-44.8
Maximum:					-6.2	0.5	-2.8

Point-Dose-Derived Average Organ Dose Comparison

Organ	CAP Doses (mGy)				CAP Percent Differences		
	Fixed-mA (Avg)	Attenuation-Based	Image-Based	Measured	Fixed-mA (Avg)	Attenuation-Based	Image-Based
Lung	25.3	20.3	23.2	21.9	15.5	-7.4	5.7
Breast	22.4	19.4	20.6	25.0	-10.3	-22.4	-17.4
Liver	25.9	24.3	24.0	22.8	13.5	6.6	5.0
Stomach	20.6	22.2	19.5	26.4	-22.0	-15.9	-26.2
Small Intestine	26.1	31.9	25.9	29.4	-11.4	8.6	-12.0
Colon	18.8	23.5	19.5	26.4	-28.9	-10.9	-26.0
Uterus	18.4	22.9	21.1	22.1	-16.6	3.8	-4.7
Ovary	19.4	23.8	22.3	21.9	-11.4	8.5	1.6
Thyroid	52.2	28.0	46.0	31.0	68.3	-9.6	48.3
Average Magnitude:					22.0	10.4	16.3
Standard Deviation:					18.4	5.6	15.1
Minimum:					-28.9	-22.4	-26.2
Maximum:					68.3	8.6	48.3

Organ	Chest Doses (mGy)				Chest Percent Differences		
	Fixed-mA (Avg)	Attenuation-Based	Image-Based	Measured	Fixed-mA (Avg)	Attenuation-Based	Image-Based
Lung	14.8	14.7	14.8	15.0	-1.1	-2.3	-1.7
Breast	13.1	13.9	13.4	16.8	-22.2	-17.1	-20.1
Liver	14.2	16.1	14.9	16.0	-11.2	0.4	-6.7
Stomach	8.9	11.0	9.7	12.3	-27.7	-10.3	-20.8
Thyroid	31.0	20.7	27.5	22.3	39.1	-7.3	23.5
Average Magnitude:					20.3	7.5	14.5
Standard Deviation:					14.7	6.7	9.7
Minimum:					-27.7	-17.1	-20.8
Maximum:					39.1	0.4	23.5

Organ	Abdomen Doses (mGy)				Abdomen Percent Differences		
	Fixed-mA (Avg)	Attenuation-Based	Image-Based	Measured	Fixed-mA (Avg)	Attenuation-Based	Image-Based
Liver	21.9	18.8	21.1	20.1	8.9	-6.7	4.7
Stomach	18.8	18.2	18.5	22.4	-16.2	-18.8	-17.6
Small Intestine	24.0	26.3	24.4	25.6	-6.1	2.8	-4.5
Colon	16.1	17.9	16.6	20.4	-21.3	-12.4	-18.4
Average Magnitude:					13.1	10.2	11.3
Standard Deviation:					6.9	7.0	7.7
Minimum:					-21.3	-18.8	-18.4
Maximum:					8.9	2.8	4.7

Organ	Pelvis Doses (mGy)				Pelvis Percent Differences		
	Fixed-mA (Avg)	Attenuation-Based	Image-Based	Measured	Fixed-mA (Avg)	Attenuation-Based	Image-Based
Uterus	18.1	19.4	18.8	19.3	-6.2	0.5	-2.8
Ovary	19.2	20.2	19.8	24.3	-21.0	-16.7	-18.4
Average Magnitude:					13.6	8.6	10.6
Standard Deviation:					10.5	11.5	11.0
Minimum:					-21.0	-16.7	-18.4
Maximum:					-6.2	0.5	-2.8

Volumetric Average Organ Dose Comparison

Organ	CAP Doses (mGy)				CAP Percent Differences		
	Fixed-mA (Avg)	Attenuation-Based	Image-Based	Measured	Fixed-mA (Avg)	Attenuation-Based	Image-Based
Lung	26.7	22.3	24.5	21.9	22.0	2.0	12.1
Breast	25.3	20.7	23.2	25.0	1.0	-17.0	-7.3
Liver	24.1	24.8	22.7	22.8	5.8	8.7	-0.4
Stomach	20.9	21.4	19.6	26.4	-20.8	-19.1	-25.8
Ovary	18.0	22.4	20.6	21.9	-17.7	2.3	-6.0
Uterus	17.3	21.8	19.7	22.1	-21.7	-1.5	-10.9
Average Magnitude:					14.8	8.4	10.4
Standard Deviation:					9.1	7.9	8.6
Minimum:					-21.7	-19.1	-25.8
Maximum:					22.0	8.7	12.1

Organ	Chest Doses (mGy)				Chest Percent Differences		
	Fixed-mA (Avg)	Attenuation-Based	Image-Based	Measured	Fixed-mA (Avg)	Attenuation-Based	Image-Based
Lung	15.5	16.0	15.7	15.0	3.6	6.4	4.7
Breast	14.8	15.0	15.1	16.8	-11.7	-10.5	-10.2
Liver	10.9	12.7	11.6	16.0	-32.2	-20.4	-27.3
Stomach	10.0	11.9	10.8	12.3	-18.7	-3.3	-12.1
Average Magnitude:					16.6	10.2	13.6
Standard Deviation:					12.1	7.4	9.7
Minimum:					-32.2	-20.4	-27.3
Maximum:					3.6	6.4	4.7

Organ	Abdomen Doses (mGy)				Abdomen Percent Differences		
	Fixed-mA (Avg)	Attenuation-Based	Image-Based	Measured	Fixed-mA (Avg)	Attenuation-Based	Image-Based
Liver	21.4	19.9	20.9	20.1	6.5	-0.9	4.0
Stomach	18.8	17.3	18.3	22.4	-16.2	-22.8	-18.3
Average Magnitude:					11.3	11.9	11.2
Standard Deviation:					6.8	15.4	10.2
Minimum:					-16.2	-22.8	-18.3
Maximum:					6.5	-0.9	4.0

Organ	Pelvis Doses (mGy)				Pelvis Percent Differences		
	Fixed-mA (Avg)	Attenuation-Based	Image-Based	Measured	Fixed-mA (Avg)	Attenuation-Based	Image-Based
Ovary	17.7	18.9	18.3	24.3	-27.2	-22.1	-24.7
Uterus	16.9	18.3	17.5	19.3	-12.7	-5.3	-9.3
Average Magnitude:					20.0	13.7	17.0
Standard Deviation:					10.3	11.8	10.8
Minimum:					-27.2	-22.1	-24.7
Maximum:					-12.7	-5.3	-9.3

APPENDIX B
PHANTOM COMPARISON STUDY DATA TABLES

Fixed Tube Current Patient-Phantom Matching Study

Male Percent Difference Average Magnitude Results

Scan	Organ	Patient-Dependent				Reference Hybrid				Reference Stylized			
		All	Healthy	Overweight	Obese	All	Healthy	Overweight	Obese	All	Healthy	Overweight	Obese
CAP	Lung*	12.7	15.3	10.8	11.8	15.3	22.9	10.4	12.0	14.6	18.9	2.7	24.1
	Pericardium*	14.3	18.0	8.9	16.5	14.4	21.5	5.1	17.3	14.9	18.6	2.2	26.1
	Bladder*	15.6	14.0	10.2	24.2	22.6	17.1	7.1	49.0	46.1	25.6	28.0	94.2
	Stomach*	11.7	17.3	4.4	13.9	20.2	19.7	5.6	39.1	22.6	20.8	8.0	43.0
	Pancreas*	10.9	20.5	3.4	8.2	21.7	19.3	5.7	44.7	23.6	20.1	7.9	47.7
	Liver*	8.9	12.9	4.9	8.9	19.0	16.1	6.0	38.9	16.6	17.1	4.7	30.7
	Spleen*	11.7	18.7	4.9	11.5	17.5	17.1	6.6	31.5	14.8	17.4	5.2	23.5
	Kidneys*	15.4	22.7	5.8	18.4	25.3	19.5	9.0	53.0	38.6	26.6	22.2	74.0
	All Organs	12.7	17.4	6.7	14.2	19.5	19.1	6.9	35.7	24.0	20.6	10.1	45.4
	In-Field Organs	12.7	17.4	6.7	14.2	19.5	19.1	6.9	35.7	24.0	20.6	10.1	45.4
Chest	Lung*	12.6	15.1	10.6	11.9	15.1	22.6	9.9	12.2	14.6	18.8	3.3	23.6
	Pericardium*	14.4	17.7	8.8	17.4	14.0	21.1	4.7	16.8	14.7	18.2	2.5	25.6
	Bladder	50.8	36.1	48.2	72.4	64.7	66.4	57.4	71.6	42.2	36.7	41.3	50.1
	Stomach*	18.0	17.3	18.4	18.3	16.4	12.4	12.5	26.2	28.9	31.0	33.7	20.1
	Pancreas	54.0	51.3	52.6	59.1	47.6	51.2	47.7	42.9	29.0	30.5	35.0	19.7
	Liver*	14.9	17.5	17.1	9.0	20.1	14.1	16.5	32.0	19.4	27.9	20.6	7.3
	Spleen*	24.0	32.5	24.6	12.6	24.9	21.6	22.4	32.2	21.5	21.6	28.1	13.1
	Kidneys	36.1	38.4	38.3	30.4	30.6	37.9	30.4	21.8	25.8	28.7	23.1	25.6
	All Organs	28.1	28.2	27.3	28.9	29.2	30.9	25.2	32.0	24.5	26.7	23.5	23.1
	In-Field Organs	16.8	20.0	15.9	13.8	18.1	18.4	13.2	23.9	19.8	23.5	18.6	17.9
Abdomen	Lung	27.1	24.4	27.6	30.0	33.1	31.2	35.2	36.8	46.2	44.7	47.9	31.6
	Pericardium	19.2	25.5	15.4	16.2	18.7	26.2	17.2	27.4	53.1	50.3	57.9	29.3
	Bladder	93.1	98.5	98.7	79.3	216.0	219.2	187.6	44.5	34.6	38.1	21.9	97.5
	Stomach*	17.8	26.3	8.3	19.1	26.2	27.6	9.4	29.1	30.9	29.9	14.5	125.9
	Pancreas*	16.3	26.7	8.7	12.6	30.1	24.2	14.6	71.0	24.6	21.8	8.5	22.4
	Liver*	14.4	20.1	8.8	14.2	23.9	18.8	10.0	33.4	17.8	18.9	2.7	64.2
	Spleen*	19.0	26.7	14.3	15.1	23.9	23.0	15.9	38.1	18.1	19.4	12.3	30.3
	Kidneys*	18.7	23.5	10.1	23.4	30.6	19.5	13.1	28.3	45.0	28.0	27.6	38.3
	All Organs	28.2	34.0	24.0	26.2	50.3	48.7	37.9	38.6	33.8	31.4	24.2	55.0
	In-Field Organs	17.2	24.7	10.1	16.9	26.9	22.6	12.6	50.3	27.3	23.6	13.1	49.6
Pelvis	Lung	36.0	28.2	39.4	41.5	40.7	43.0	41.4	36.8	35.9	40.9	34.2	31.6
	Pericardium	28.9	21.1	40.3	24.3	37.2	40.5	41.7	27.4	38.4	41.0	43.2	29.3
	Bladder*	16.0	12.8	11.5	25.8	21.4	18.2	6.2	44.5	48.0	27.0	29.4	97.5
	Stomach	70.5	60.5	108.5	35.5	36.8	42.1	37.8	29.1	115.9	122.9	101.0	125.9
	Pancreas	138.6	183.6	144.1	75.3	69.8	87.4	51.3	71.0	31.8	36.3	34.9	22.4
	Liver	60.0	59.9	92.9	18.9	32.9	26.6	38.8	33.4	67.4	66.1	71.3	64.2
	Spleen	36.3	32.2	42.8	33.5	40.5	39.9	42.8	38.1	43.6	56.0	41.9	30.3
	Kidneys	50.4	79.7	47.1	17.9	25.7	24.2	25.2	28.3	30.5	23.4	31.4	38.3
	All Organs	54.6	59.8	65.8	34.1	38.1	40.2	35.7	38.6	51.5	51.7	48.4	55.0
	In-Field Organs	16.0	12.8	11.5	25.8	21.4	18.2	6.2	44.5	48.0	27.0	29.4	97.5

* Denotes in-field organ for the respective exam.

Female Percent Difference Average Magnitude Results

Scan	Organ	Patient-Dependent				Reference Hybrid				Reference Stylized			
		All	Healthy	Overweight	Obese	All	Healthy	Overweight	Obese	All	Healthy	Overweight	Obese
CAP	Lung*	9.2	11.9	6.1	7.4	23.7	21.6	5.2	40.9	23.7	19.7	4.5	44.2
	Pericardium*	11.0	15.3	6.5	8.0	24.1	24.4	4.2	38.7	24.3	19.5	2.7	47.6
	Bladder*	12.3	13.9	7.6	13.4	48.2	11.9	22.3	121.9	65.0	17.5	40.4	154.9
	Stomach*	11.7	3.6	6.5	27.8	30.5	11.4	9.1	75.2	27.8	18.5	2.1	61.2
	Pancreas*	16.3	5.1	8.9	38.7	39.9	10.5	15.0	102.6	34.6	22.5	4.4	75.3
	Liver*	9.5	4.6	5.9	19.5	28.2	13.8	7.1	65.5	26.6	25.2	7.6	42.9
	Spleen*	18.9	7.7	13.2	39.9	30.2	7.1	12.3	78.3	26.6	24.5	12.0	40.9
	Kidneys*	23.7	8.7	23.7	46.2	47.3	7.4	33.7	117.3	38.8	10.1	20.4	95.6
	All Organs	14.1	8.8	9.8	25.1	34.0	13.5	13.6	80.0	33.4	19.7	11.8	70.3
	In-Field Organs	14.1	8.8	9.8	25.1	34.0	13.5	13.6	80.0	33.4	19.7	11.8	70.3
Chest	Lung*	9.1	12.0	5.7	7.3	23.9	21.6	5.1	41.7	24.0	19.9	4.5	44.6
	Pericardium*	11.1	15.4	6.3	8.4	24.1	24.4	3.5	39.0	24.5	19.6	3.3	48.0
	Bladder	45.8	47.9	45.9	42.5	51.6	47.6	51.3	57.9	57.3	60.2	64.0	47.9
	Stomach*	16.2	10.4	18.3	23.2	38.0	14.7	28.3	80.4	37.9	51.5	27.1	25.6
	Pancreas	33.5	46.1	31.2	16.2	50.9	38.0	54.4	67.5	48.0	39.8	48.8	59.6
	Liver*	12.8	8.0	14.6	18.5	32.0	12.4	18.2	71.9	31.4	41.3	21.0	24.5
	Spleen*	14.6	6.0	9.0	31.9	29.7	7.0	12.0	77.2	34.5	44.5	33.2	20.3
	Kidneys	33.1	33.6	49.1	20.4	37.8	38.9	36.4	37.3	37.9	48.5	25.4	31.4
	All Organs	22.0	22.4	22.5	21.1	36.0	25.6	26.1	59.1	36.9	40.7	28.4	37.7
	In-Field Organs	12.8	10.4	10.8	17.9	30.9	16.0	13.4	62.0	31.7	35.4	17.8	32.6
Abdomen	Lung	20.2	18.2	31.2	15.0	29.5	32.7	27.9	25.8	47.5	56.5	45.8	35.2
	Pericardium	19.7	19.5	26.1	15.1	31.5	31.9	22.0	37.9	48.5	61.0	51.3	27.8
	Bladder	74.6	49.4	64.5	120.0	150.8	119.8	133.0	210.5	50.6	59.2	43.4	43.2
	Stomach*	17.9	7.1	14.1	37.1	37.7	11.6	16.2	92.8	32.7	16.5	7.0	76.2
	Pancreas*	24.4	7.9	19.1	53.1	48.7	6.0	27.4	128.7	38.7	24.4	8.2	82.9
	Liver*	13.5	4.4	12.9	27.6	34.5	12.6	13.3	83.2	30.3	27.0	7.3	52.3
	Spleen*	33.0	16.3	27.0	62.6	46.0	12.0	27.6	111.0	30.2	22.6	11.5	55.8
	Kidneys*	33.5	12.5	38.4	61.3	61.6	10.6	52.9	144.5	47.2	9.0	34.0	114.3
	All Organs	29.6	16.9	29.2	49.0	55.0	29.6	40.0	104.3	40.7	34.5	26.1	61.0
	In-Field Organs	24.5	9.6	22.3	48.3	45.7	10.5	27.5	112.0	35.8	19.9	13.6	76.3
Pelvis	Lung	36.9	30.9	46.9	38.4	46.6	42.0	57.1	45.6	58.0	59.4	70.0	46.9
	Pericardium	39.7	35.0	48.8	39.8	50.1	46.1	61.4	47.8	59.2	60.3	71.5	48.3
	Bladder*	11.4	12.8	6.3	13.1	47.6	11.5	22.0	121.1	66.4	17.4	42.4	158.1
	Stomach	34.9	29.9	46.2	33.9	50.5	49.1	64.4	42.1	51.7	42.9	38.9	74.6
	Pancreas	33.7	22.1	60.4	31.1	34.0	15.1	52.9	48.0	46.6	41.7	69.1	37.2
	Liver	39.3	31.7	52.3	40.9	51.0	45.1	65.8	48.9	43.8	36.5	52.3	48.5
	Spleen	29.0	34.1	33.5	17.8	35.4	33.2	46.8	30.1	37.6	38.8	33.3	39.1
	Kidneys	35.9	31.5	50.4	31.5	47.7	40.3	57.0	51.7	49.2	47.0	67.9	38.7
	All Organs	32.6	28.5	43.1	30.8	45.4	35.3	53.4	54.4	51.6	43.0	55.7	61.4
	In-Field Organs	11.4	12.8	6.3	13.1	47.6	11.5	22.0	121.1	66.4	17.4	42.4	158.1

* Denotes in-field organ for the respective exam.

ATCM Patient-Phantom Matching Study

Male Percent Difference Average Magnitude Results

Scan	Organ	Patient-Dependent				Reference Hybrid				Reference Stylized			
		All	Healthy	Overweight	Obese	All	Healthy	Overweight	Obese	All	Healthy	Overweight	Obese
CAP	Lung*	14.0	21.2	7.1	13.8	24.8	27.1	5.9	45.5	25.0	26.2	4.1	49.8
	Pericardium*	12.9	20.1	7.0	11.5	23.4	24.5	4.0	46.2	23.5	24.3	3.9	47.2
	Bladder*	11.0	13.0	7.9	12.2	23.1	17.3	8.3	49.1	53.9	31.9	36.6	103.1
	Stomach*	10.9	15.9	5.5	11.2	14.7	19.0	3.1	23.9	15.0	18.2	2.7	26.3
	Pancreas*	10.0	15.2	4.9	9.7	14.8	20.3	3.1	22.4	15.0	19.6	2.8	24.5
	Liver*	9.1	12.2	5.3	10.0	16.3	18.4	2.8	30.6	16.4	21.5	7.6	21.1
	Spleen*	9.9	14.9	4.3	10.5	14.2	19.6	4.4	19.6	13.7	22.4	6.6	11.6
	Kidneys*	9.8	14.5	5.2	9.7	13.4	17.3	3.4	20.9	24.0	19.9	16.9	38.0
	All Organs	10.9	15.9	5.9	11.1	18.1	20.4	4.4	32.3	23.3	23.0	10.2	40.2
	In-Field Organs	10.9	15.9	5.9	11.1	18.1	20.4	4.4	32.3	23.3	23.0	10.2	40.2
Chest	Lung*	13.7	21.0	6.7	13.4	25.2	26.7	5.9	47.3	25.4	26.0	4.8	50.5
	Pericardium*	12.5	19.7	5.9	11.8	23.7	24.1	4.3	47.3	23.9	23.9	4.4	48.1
	Bladder	42.1	24.7	42.2	63.5	56.6	57.0	49.5	65.0	46.5	41.5	45.4	54.3
	Stomach*	17.7	19.2	16.2	17.7	15.5	17.0	10.8	19.4	34.3	35.2	38.6	28.0
	Pancreas	57.4	55.5	55.1	62.8	50.8	53.8	48.4	50.1	27.2	34.4	34.1	9.7
	Liver*	13.8	14.8	15.3	10.7	18.7	16.3	13.9	27.5	24.0	33.0	26.3	10.1
	Spleen*	18.4	26.9	18.7	7.3	21.8	24.7	18.9	21.8	24.1	26.5	28.4	15.9
	Kidneys	40.3	40.4	41.0	39.1	33.5	42.3	34.5	21.3	25.6	34.6	23.8	16.7
	All Organs	27.0	27.8	25.2	28.3	30.7	32.7	23.3	37.5	28.9	31.9	25.7	29.2
	In-Field Organs	15.2	20.3	12.6	12.2	21.0	21.8	10.8	32.6	26.4	28.9	20.5	30.5
Abdomen	Lung	27.3	26.2	29.3	26.2	35.9	34.5	38.3	34.6	47.8	46.6	49.7	46.8
	Pericardium	17.6	22.8	17.2	11.7	17.2	24.8	19.2	5.3	54.8	52.7	59.4	51.6
	Bladder	98.9	94.8	106.5	94.7	192.7	211.2	181.2	183.9	32.6	38.2	19.4	42.2
	Stomach*	14.1	19.5	8.5	14.5	16.2	20.0	6.7	23.2	18.7	21.8	6.5	30.2
	Pancreas*	11.9	17.5	5.3	13.0	16.6	17.9	6.3	27.7	14.7	19.7	3.6	22.5
	Liver*	10.4	11.5	8.6	11.3	17.0	18.1	5.8	29.6	16.2	21.2	6.7	21.8
	Spleen*	14.6	18.1	11.6	14.2	16.7	20.6	12.3	17.2	16.6	23.4	12.9	12.8
	Kidneys*	11.9	15.6	5.2	15.6	16.2	16.0	6.2	29.0	28.5	20.7	21.3	47.4
	All Organs	25.9	28.2	24.0	25.2	41.1	45.4	34.5	43.8	28.7	30.5	22.4	34.4
	In-Field Organs	12.6	16.4	7.9	13.7	16.5	18.5	7.5	25.4	19.0	21.3	10.2	26.9
Pelvis	Lung	30.8	21.8	40.7	29.6	39.2	36.9	38.7	42.7	32.3	33.5	29.6	34.2
	Pericardium	30.3	15.1	43.4	33.0	34.6	33.4	38.0	32.0	35.6	33.9	39.2	33.2
	Bladder*	10.1	11.4	7.9	11.2	22.6	18.4	7.9	46.1	57.1	33.6	38.8	109.2
	Stomach	85.4	62.6	124.1	65.5	38.4	40.9	39.1	34.2	118.9	120.1	112.3	125.6
	Pancreas	168.9	199.0	172.8	126.6	74.0	87.0	62.2	72.5	32.0	33.6	35.6	25.4
	Liver	74.5	65.9	106.5	45.5	30.3	19.5	39.8	31.9	70.8	67.5	80.4	62.8
	Spleen	34.9	33.4	50.0	17.8	38.4	33.5	38.7	44.1	46.8	56.2	50.1	31.0
	Kidneys	65.8	91.8	64.6	34.6	24.4	17.6	24.4	33.0	29.7	18.0	30.8	42.8
	All Organs	62.6	62.6	76.2	45.5	37.7	35.9	36.1	42.1	52.9	49.6	52.1	58.0
	In-Field Organs	10.1	11.4	7.9	11.2	22.6	18.4	7.9	46.1	57.1	33.6	38.8	109.2

* Denotes in-field organ for the respective exam.

Female Percent Difference Average Magnitude Results

Scan	Organ	Patient-Dependent				Reference Hybrid				Reference Stylized			
		All	Healthy	Overweight	Obese	All	Healthy	Overweight	Obese	All	Healthy	Overweight	Obese
CAP	Lung*	7.3	4.4	4.2	14.1	40.6	10.5	13.8	105.9	36.8	18.7	6.1	87.0
	Pericardium*	5.7	4.1	6.1	7.9	43.7	11.0	18.9	111.4	40.1	17.2	10.5	96.6
	Bladder*	17.6	15.9	11.2	25.0	44.7	14.6	14.3	112.5	54.9	12.3	28.4	138.6
	Stomach*	7.8	2.5	4.9	18.1	31.4	9.9	14.3	76.5	30.4	13.4	12.2	69.7
	Pancreas*	5.3	3.7	2.1	10.2	34.7	13.0	11.8	84.5	33.1	17.7	8.6	74.5
	Liver*	6.1	4.4	4.7	9.5	30.9	9.9	15.6	74.0	27.3	21.1	6.3	52.3
	Spleen*	6.7	3.9	5.4	11.9	34.1	6.0	20.1	86.6	27.7	20.2	7.2	54.3
	Kidneys*	5.6	2.8	7.9	8.1	31.4	5.9	20.3	77.8	32.4	5.7	22.0	80.3
	All Organs	7.8	5.2	5.8	13.1	36.4	10.1	16.1	91.1	35.3	15.8	12.7	81.7
	In-Field Organs	7.8	5.2	5.8	13.1	36.4	10.1	16.1	91.1	35.3	15.8	12.7	81.7
Chest	Lung*	7.8	4.2	5.5	14.9	42.5	10.2	15.5	111.2	38.2	19.0	6.9	90.5
	Pericardium*	6.4	4.3	7.5	8.6	45.7	10.7	20.9	116.7	41.7	17.4	11.8	100.5
	Bladder	40.0	47.6	45.2	24.6	51.0	47.8	55.3	52.4	54.6	57.7	58.5	47.1
	Stomach*	16.1	12.3	27.1	13.5	46.2	12.6	46.1	96.7	36.4	48.7	19.1	30.8
	Pancreas	33.4	46.6	20.5	23.4	53.4	37.4	62.4	70.8	52.8	37.7	60.8	69.7
	Liver*	11.8	8.9	25.3	6.0	44.0	10.3	38.2	98.8	33.6	38.4	17.2	38.7
	Spleen*	7.9	5.0	10.3	10.6	38.1	5.9	25.1	96.0	33.4	41.5	22.8	29.1
	Kidneys	40.4	36.5	52.8	37.1	40.5	38.9	52.1	34.1	39.0	45.0	43.5	26.5
	All Organs	20.5	20.7	24.3	17.3	45.2	21.7	39.5	84.6	41.2	38.2	30.1	54.1
	In-Field Organs	10.0	6.9	15.2	10.7	43.3	10.0	29.2	103.9	36.6	33.0	15.6	57.9
Abdomen	Lung	17.9	18.2	20.0	15.7	28.3	29.9	18.5	33.1	40.9	52.2	37.9	26.1
	Pericardium	20.1	20.2	16.4	22.8	30.4	26.7	13.9	48.2	41.9	56.9	43.5	18.1
	Bladder	68.6	51.1	56.4	104.0	126.5	122.9	108.5	145.4	52.4	62.9	50.3	38.0
	Stomach*	9.8	3.1	4.7	23.8	35.5	11.8	19.4	83.1	35.0	12.3	18.4	81.6
	Pancreas*	6.9	1.7	5.9	15.4	40.1	9.1	22.7	99.6	35.4	18.0	10.8	80.1
	Liver*	5.8	2.4	5.4	11.3	33.3	12.1	19.1	75.8	28.4	21.0	6.0	56.4
	Spleen*	15.2	10.5	17.6	20.2	45.3	10.3	34.6	105.8	29.8	16.4	9.1	65.6
	Kidneys*	10.5	5.1	20.0	11.4	41.6	6.9	38.9	95.8	42.2	6.9	39.7	96.9
	All Organs	19.4	14.1	18.3	28.1	47.6	28.7	34.5	85.8	38.3	30.8	27.0	57.9
	In-Field Organs	9.7	4.6	10.7	16.4	39.2	10.0	26.9	92.0	34.2	14.9	16.8	76.1
Pelvis	Lung	38.3	30.6	46.2	43.9	49.5	43.8	63.0	48.0	60.5	60.7	74.2	49.8
	Pericardium	40.2	34.0	48.6	43.1	52.7	47.8	67.0	49.3	61.1	61.6	75.7	49.5
	Bladder*	16.9	15.3	9.8	24.8	46.3	15.0	15.0	116.9	57.3	12.6	30.0	145.0
	Stomach	43.1	35.0	46.5	52.8	54.3	52.8	69.7	44.9	44.5	44.9	47.8	41.3
	Pancreas	44.5	23.9	55.1	67.5	34.5	19.6	61.0	36.9	49.7	43.2	74.4	40.9
	Liver	41.5	36.0	51.5	42.0	53.6	47.7	70.5	49.9	47.4	40.2	58.7	49.8
	Spleen	42.2	40.7	32.8	51.5	39.0	37.4	54.4	29.8	38.0	40.9	42.7	30.0
	Kidneys	45.8	38.0	50.1	54.3	47.5	44.4	63.5	40.1	49.3	50.0	72.6	30.7
	All Organs	39.1	31.7	42.6	47.5	47.2	38.6	58.0	52.0	51.0	44.3	59.5	54.6
	In-Field Organs	16.9	15.3	9.8	24.8	46.3	15.0	15.0	116.9	57.3	12.6	30.0	145.0

* Denotes in-field organ for the respective exam.

LIST OF REFERENCES

- ¹J.T. Bushberg, J.A. Seibert, E.M. Leidholdt Jr, J.M. Boone, *The Essential Physics of Medical Imaging*, 3rd ed. (Lippincott Williams & Wilkins, Philadelphia, PA, 2011).
- ²BEIR, *Biological Effects of Ionizing Radiation*, Report BEIR VII (National Research Council, Washington, DC, 2007).
- ³A.B. de Gonzalez, K.P. Kim, J.M. Samet, "Radiation-induced cancer risk from annual computed tomography for patients with cystic fibrosis," *Am. J. Respir. Crit. Care Med.* **176**, 970-973 (2007).
- ⁴D.J. Brenner and E.J. Hall, "Current concepts - Computed tomography - An increasing source of radiation exposure," *N. Engl. J. Med.* **357**, 2277-2284 (2007).
- ⁵W.R. Hendee and M.K. O'Connor, "Radiation Risks of Medical Imaging: Separating Fact from Fantasy," *Radiology* **264**, 312-321 (2012).
- ⁶M.S. Pearce, J.A. Salotti, M.P. Little, K. McHugh, C. Lee, K.P. Kim, N.L. Howe, C.M. Ronckers, P. Rajaraman, A.W. Craft, L. Parker, A.B. de Gonzalez, "Radiation exposure from CT scans in childhood and subsequent risk of leukaemia and brain tumours: a retrospective cohort study," *Lancet* **380**, 499-505 (2012).
- ⁷M.S. Pearce. "CT scans in childhood and risk of leukaemia and brain tumours reply," *Lancet* **380**, 1736-1737 (2012).
- ⁸O. Linton and F. Mettler, "National Conference on Dose Reduction in CT, with an emphasis on pediatric patients," *Am. J. Roentgenol.* **181**, 321-329 (2003).
- ⁹M. Kalra, M. Maher, T. Toth, B. Schmidt, B. Westerman, H. Morgan, S. Saini, "Techniques and applications of automatic tube current modulation for CT," *Radiology* **233**, 649-657 (2004).
- ¹⁰M.K. Kalra, N. Naz, S.M.R. Rizzo, M.A. Blake, "Computed tomography radiation dose optimization: scanning protocols and clinical applications of automatic exposure control." *Curr. Probl. Diagn. Radiol.* **34**, 171-181 (2005).
- ¹¹C.H. McCollough, M.R. Bruesewitz, J.M. Kofler Jr., "CT dose reduction and dose management tools: Overview of available options," *Radiographics* **26**, 503-514 (2006).
- ¹²C.H. Lee, J.M. Goo, H.J. Ye, S.J. Ye, C.M. Park, E.J. Chun, J.G. Im, "Radiation dose modulation techniques in the multidetector CT era: from basics to practice," *Radiographics* **28**, 1451-1459 (2008).
- ¹³T. Mulkens, P. Bellinck, M. Baeyaert, D. Ghysen, X. Van Dijck, E. Mussen, C. Venstermans, J. Termote, "Use of an automatic exposure control mechanism for dose

optimization in multi-detector row CT examinations: Clinical evaluation," *Radiology* **237**, 213-223 (2005).

¹⁴M. Soderberg and M. Gunnarsson, "Automatic exposure control in computed tomography--an evaluation of systems from different manufacturers," *Acta Radiol.* **51**, 625-634 (2010).

¹⁵J.F. Winslow, D.E. Hyer, R.F. Fisher, C.J. Tien, D.E. Hintenlang, "Construction of anthropomorphic phantoms for use in dosimetry studies," *Journal of Applied Clinical Med. Phys.* **10**, 195-204 (2009).

¹⁶ICRP, *Basic Anatomical and Physiological Data for Use in Radiological Protection: Reference Values*, Report 89 (International Commission on Radiological Protection, Oxford, UK, 2003).

¹⁷D.E. Hyer, R.F. Fisher, D.E. Hintenlang, "Characterization of a water-equivalent fiber-optic coupled dosimeter for use in diagnostic radiology," *Med. Phys.* **36**, 1711-1716 (2009).

¹⁸T.M. Griglock, *Determining Organ Doses from Computed Tomography Scanners using Cadaveric Subjects* (University of Florida, Gainesville, FL, 2012).

¹⁹J.J. DeMarco, C.H. Cagnon, D.D. Cody, D.M. Stevens, C.H. McCollough, J. O'Daniel, M.F. McNitt-Gray, "A Monte Carlo based method to estimate radiation dose from multidetector CT (MDCT): cylindrical and anthropomorphic phantoms," *Phys. Med. Biol.* **50**, 3989-4004 (2005).

²⁰J.J. DeMarco, C.H. Cagnon, D.D. Cody, D.M. Stevens, C.H. McCollough, M. Zankl, E. Angel, M.F. McNitt-Gray, "Estimating radiation doses from multidetector CT using Monte Carlo simulations: effects of different size voxelized patient models on magnitudes of organ and effective dose," *Phys. Med. Biol.* **52**, 2583-2597 (2007).

²¹C. Lee, C. Lee, R.J. Staton, D.E. Hintenlang, M.M. Arreola, J.L. Williams, W.E. Bolch, "Organ and effective doses in pediatric patients undergoing helical multislice computed tomography examination," *Med. Phys.* **34**, 1858-1873 (2007).

²²E. Angel, C.V. Wellnitz, M.M. Goodsitt, N. Yaghmai, J.J. DeMarco, C.H. Cagnon, J.W. Sayre, D.D. Cody, D.M. Stevens, A.N. Primak, C.H. McCollough, M.F. McNitt-Gray, "Radiation dose to the fetus for pregnant patients undergoing multidetector CT imaging: Monte Carlo simulations estimating fetal dose for a range of gestational age and patient size," *Radiology* **249**, 220-227 (2008).

²³P. Deak, M. van Straten, P.C. Shrimpton, M. Zankl, W.A. Kalender, "Validation of a Monte Carlo tool for patient-specific dose simulations in multi-slice computed tomography," *Eur. Radiol.* **18**, 759-772 (2008).

- ²⁴C. Lee, D. Lodwick, J.L. Williams, W.E. Bolch, "Hybrid computational phantoms of the 15-year male and female adolescent: applications to CT organ dosimetry for patients of variable morphometry," *Med. Phys.* **35**, 2366-2382 (2008).
- ²⁵E. Angel, N. Yaghmai, C.M. Jude, J.J. DeMarco, C.H. Cagnon, J.G. Goldin, C.H. McCollough, A.N. Primak, D.D. Cody, D.M. Stevens, M.F. McNitt-Gray, "Dose to radiosensitive organs during routine chest CT: effects of tube current modulation," *Am. J. Roentgenol.* **193**, 1340-1345 (2009).
- ²⁶E. Angel, N. Yaghmai, C.M. Jude, J.J. Demarco, C.H. Cagnon, J.G. Goldin, A.N. Primak, D.M. Stevens, D.D. Cody, C.H. McCollough, M.F. McNitt-Gray, "Monte Carlo simulations to assess the effects of tube current modulation on breast dose for multidetector CT," *Phys. Med. Biol.* **54**, 497-512 (2009).
- ²⁷C. Lee, K.P. Kim, D. Long, R. Fisher, C. Tien, S.L. Simon, A. Bouville, W.E. Bolch, "Organ doses for reference adult male and female undergoing computed tomography estimated by Monte Carlo simulations," *Med. Phys.* **38**, 1196-1206 (2011).
- ²⁸D.J. Long, C. Lee, C. Tien, R. Fisher, M.R. Hoerner, D. Hintenlang, W.E. Bolch, "Monte Carlo simulations of adult and pediatric computed tomography exams: Validation studies of organ doses with physical phantoms," *Med. Phys.* **40**, 013901 (2013).
- ²⁹X. Li, E. Samei, W.P. Segars, G.M. Sturgeon, J.G. Colsher, G. Toncheva, T.T. Yoshizumi, D.P. Frush, "Patient-specific radiation dose and cancer risk estimation in CT: part I. development and validation of a Monte Carlo program," *Med. Phys.* **38**, 397-407 (2011).
- ³⁰H. Liu, J. Gu, P.F. Caracappa, X.G. Xu, "Comparison of two types of adult phantoms in terms of organ doses from diagnostic CT procedures," *Phys. Med. Biol.* **55**, 1441-1451 (2010).
- ³¹P. Shrimpton and D. Jones, "Normalized Organ Doses for X-Ray Computed-Tomography Calculated using Monte-Carlo Techniques and a Mathematical Anthropomorphic Phantom," *Radiat. Prot. Dosimet.* **49**, 241-243 (1993).
- ³²G. Williams, M. Zankl, W. Abmayr, R. Veit, G. Drexler, "The Calculation of Dose from External Photon Exposures using Reference and Realistic Human Phantoms and Monte-Carlo Methods," *Phys. Med. Biol.* **31**, 449-452 (1986).
- ³³G. Stamm and H. Nagel, "CT-Expo - a novel program for dose evaluation in CT," *Rofo-Fortschritte Auf Dem Gebiet Der Rontgenstrahlen Und Der Bildgebenden Verfahren* **174**, 1570-1576 (2002).

- ³⁴C. Lee, D. Lodwick, D. Hasenauer, J.L. Williams, C. Lee, W.E. Bolch, "Hybrid computational phantoms of the male and female newborn patient: NURBS-based whole-body models," *Phys. Med. Biol.* **52**, 3309 (2007).
- ³⁵J. Wang, X. Duan, J.A. Christner, S. Leng, L. Yu, C.H. McCollough, "Radiation dose reduction to the breast in thoracic CT: comparison of bismuth shielding, organ-based tube current modulation, and use of a globally decreased tube current," *Med. Phys.* **38**, 6084-6092 (2011).
- ³⁶H. Greess, H. Wolf, U. Baum, M. Lell, M. Pirkl, W. Kalender, W.A. Bautz, "Dose reduction in computed tomography by attenuation-based on-line modulation of tube current: evaluation of six anatomical regions," *Eur. Radiol.* **10**, 391-394 (2000).
- ³⁷M.S. May, P. Deak, A. Kuettner, M.M. Lell, W. Wuest, M. Scharf, A.K. Keller, L. Haberle, S. Achenbach, M. Seltmann, M. Uder, W.A. Kalender, "Radiation dose considerations by intra-individual Monte Carlo simulations in dual source spiral coronary computed tomography angiography with electrocardiogram-triggered tube current modulation and adaptive pitch," *Eur. Radiol.* **22**, 569-578 (2012).
- ³⁸M. van Straten, P. Deak, P.C. Shrimpton, W.A. Kalender, "The effect of angular and longitudinal tube current modulations on the estimation of organ and effective doses in x-ray computed tomography," *Med. Phys.* **36**, 4881-4889 (2009).
- ³⁹M. Khatonabadi, H.J. Kim, P. Lu, K.L. McMillan, C.H. Cagnon, J.J. DeMarco, M.F. McNitt-Gray, "The feasibility of a regional CTDI_{vol} to estimate organ dose from tube current modulated CT exams," *Med. Phys.* **40**, 051903 (2013).
- ⁴⁰F. Zanca, M. Demeter, R. Oyen, H. Bosmans, "Excess radiation and organ dose in chest and abdominal CT due to CT acquisition beyond expected anatomical boundaries," *Eur. Radiol.* **22**, 779-788 (2012).
- ⁴¹H. Schlattl, M. Zankl, J. Becker, C. Hoeschen, "Dose conversion coefficients for CT examinations of adults with automatic tube current modulation," *Phys. Med. Biol.* **55**, 6243-6261 (2010).
- ⁴²M. Gies, W.A. Kalender, H. Wolf, C. Suess, "Dose reduction in CT by anatomically adapted tube current modulation. I. Simulation studies," *Med. Phys.* **26**, 2235-2247 (1999).
- ⁴³A.C. Turner, D. Zhang, H.J. Kim, J.J. DeMarco, C.H. Cagnon, E. Angel, D.D. Cody, D.M. Stevens, A.N. Primak, C.H. McCollough, M.F. McNitt-Gray, "A method to generate equivalent energy spectra and filtration models based on measurement for multidetector CT Monte Carlo dosimetry simulations," *Med. Phys.* **36**, 2154-2164 (2009).

- ⁴⁴M. Ghita, *Computer Simulations to Estimate Organ Doses from Clinically Validated Cardiac, Neuro, and Pediatric Protocols for Multiple Detector Computed Tomography Scanners* (University of Florida, Gainesville, FL, 2009).
- ⁴⁵D.B. Pelowitz, "MCNPX user's Manual Version 2.7.0," Los Alamos National Laboratory **LA-CP-11-00438** (2011).
- ⁴⁶J.H. Siewerdsen, A.M. Waese, D.J. Moseley, S. Richard, D.A. Jaffray, "Spektr: a computational tool for x-ray spectral analysis and imaging system optimization," *Med. Phys.* **31**, 3057-3067 (2004).
- ⁴⁷T.C. Chao, A. Bozkurt, X.G. Xu, "Conversion coefficients based on the VIP-Man anatomical model and EGS4-VLSI code for external monoenergetic photons from 10 keV to 10 MeV," *Health Phys.* **81**, 163-183 (2001).
- ⁴⁸T.M. Griglock, *Determining Organ Doses from Computed Tomography Scanners using Cadaveric Subjects* (University of Florida, Gainesville, FL, 2012).
- ⁴⁹M. Cristy and K.F. Eckerman, "Specific absorbed fractions of energy at various ages from internal photon sources," Oak Ridge National Laboratory **ORNL/TM-8381, Vol. 1** (1987).
- ⁵⁰A. Geyer M., *The University of Florida/National Cancer Institute Family of Hybrid Computational Phantoms Representing the Current United States Population of Male and Female Children and Adolescents Applications to Computed Tomography Dosimetry* (University of Florida, Gainesville, FL, 2012).
- ⁵¹P.B. Johnson, S.R. Whalen, M. Wayson, B. Juneja, C. Lee, W.E. Bolch, "Hybrid Patient-Dependent Phantoms Covering Statistical Distributions of Body Morphometry in the US Adult and Pediatric Population," *Proc IEEE* **97**, 2060-2075 (2009).
- ⁵²J.L. Hurtado, C. Lee, D. Lodwick, T. Goede, J.L. Williams, W.E. Bolch, "Hybrid computational phantoms representing the reference adult male and adult female: construction and applications for retrospective dosimetry," *Health Phys.* **102**, 292-304 (2012).
- ⁵³E. Han, W. Bolch, K. Eckerman, "Revisions to the ORNL series of adult and pediatric computational phantoms for use with the mird schema," *Health Phys.* **90**, 337-356 (2006).
- ⁵⁴P.B. Johnson, A. Geyer, D. Borrego, K. Ficarrota, K. Johnson, W.E. Bolch, "The impact of anthropometric patient-phantom matching on organ dose: a hybrid phantom study for fluoroscopy guided interventions," *Med. Phys.* **38**, 1008-1017 (2011).

BIOGRAPHICAL SKETCH

Daniel Joseph Long was born in 1987 in Palm Harbor, Florida to Tom and Colleen Long. He has one older brother, Chris. He graduated from Palm Harbor University High School in 2005, and graduated with his Bachelor of Science in nuclear engineering from the University of Florida in May 2009. He graduated with his Master of Science in biomedical engineering with a specialty in medical physics at the University of Florida in August 2011, after which he began pursuit of a doctorate in the same field, which he received in August 2013. Daniel met his wife, Nelia, in his junior year of undergraduate studies on the day of his first nuclear engineering class. Three years later, they married in August 2010.